Summer 8-15-2015

Enhanced Magnetism in Dy and Tb at Extreme Pressure

Jinhyuk Lim
Washington University in St. Louis

WASHINGTON UNIVERSITY IN ST. LOUIS

Department of Physics

Dissertation Examination Committee:
James S. Schilling, Chair
Mark S. Conradi
Sophia E. Hayes
Erik A. Henriksen
Kater W. Murch
Li Yang

Enhanced Magnetism in Dy and Tb at Extreme Pressure

by

Jinhyuk Lim

A dissertation presented to the
Graduate School of Arts & Sciences
of Washington University in
partial fulfillment of the
requirements for the degree
of Doctor of Philosophy

August 2015
St. Louis, Missouri

Table of Contents

List of Figures

List of Tables

Acknowledgements

This research was gratefully supported by the National Science Foundation (NSF) through Grant No. DMR-1104742 and by the Carnegie/DOE Alliance Center (CDAC) through NNSA/DOE Grant No. DE-FC52-08NA28554. In addition, special thanks are due:

Prof. James S. Schilling, my thesis advisor, for showing me an exemplary life as an academic educator and researcher and for training me to be a high pressure physicist and Dr. Daniel Haskel and Prof. Zohar Nussinov for their support for my academic career.

Prof. Takahiro Matsuoka for teaching me high pressure electrical resistivity technique and Drs. Anup Gangopadhyay, Wenli Bi, Narelle Hillier, Neda Foroozani, and Gilberto Fabbris for their encouragement and help in many experiments.

Dian Tan, Vikas Soni, Jing Song, and Matt Ferguson for their technical assistance and helpful discussions and Satcher Hsieh and Christopher West for their proofreading of this dissertation.

Lastly, my church members, parents, wife, and three children for their trust and love for me.

Jinhyuk Lim

Washington University in St. Louis

August 2015

ABSTRACT OF THE DISSERTATION

Enhanced Magnetism in Dy and Tb at Extreme Pressure

by

Jinhyuk Lim

Doctor of Philosophy in Physics

Washington University in St. Louis, 2015

Professor James S. Schilling, Chair

At ambient pressure all lanthanide metals order magnetically at temperatures at or below ambient. The magnetic ordering is known to result from the indirect exchange interaction between localized 4*f* magnetic moments mediated by the surrounding conduction electrons, the so-called Ruderman-Kittel-Kasuya-Yosida (RKKY) interaction. With the RKKY interaction the magnetic ordering temperature T_o is expected to be proportional to the de Gennes factor which is a function of the Landé g factor g_J and the total angular momentum J. For example, Gd has the highest value of T_o, 292 K, at ambient pressure as it has the largest de Gennes factor of 15.75. Under extreme pressure, however, one anticipates that the 4*f* state of lanthanides would become unstable leading to exotic physics due to the competition between the RKKY interaction and Kondo screening. Four-point dc electrical resistivity measurements have been carried out on the heavy lanthanides Dy, Tb, and Gd in conjunction with their dilute magnetic alloys Y(Dy), Y(Tb), and Y(Gd) under extreme pressures well above those where their atomic volume collapse occurs, P_{vc}. Unlike Gd, the results obtained reveal for Dy and Tb a strong deviation from de Gennes scaling in the pressure dependence of T_o as well as a dramatic suppression of superconductivity in a superconducting Y host, all beginning for pressures just above P_{vc}. T_o for Dy and Tb appears to rise well above room temperature at 157 GPa and 141 GPa, respectively. These results provide insight into possible Kondo lattice behavior in Dy and Tb.

Chapter 1

Introduction

High pressure science is growing rapidly as evidenced by the increasing number of papers each year utilizing high pressure techniques such as diamond anvil cells [1]. The reason is that high pressure is a unique tool to modify the electronic structure of matter in a relatively simple way by changing interatomic distances. Recent technological developments allow the measurement of condensed matter systems to explore new and exotic phases of matter under extreme pressures in the multimegabar range.

Currently, the most active fields in condensed matter physics include studies of topological insulators [2], dense Kondo behavior [3], and exotic forms of superconductivity [4], all of which are closely related to magnetic instabilities. Subjecting matter to extreme pressures has the potential to turn conventional, stable magnetic systems into ones with new and exotic magnetic or superconducting states.

The heavy lanthanide metals exhibit stable magnetic properties due to their highly localized 4*f*-electron orbitals. The indirect Ruderman-Kittel-Kasuya-Yosida (RKKY) exchange interaction is known to lead to magnetic ordering phenomena, where the resultant magnetic ordering

temperature T_o obeys simple de Gennes scaling. However, extreme pressure may change this scenario and push the heavy lanthanides into a magnetically unstable region where the RKKY interaction and the Kondo screening strongly compete with each other. In this case, de Gennes scaling would no longer hold.

At ambient pressure, heavy lanthanide metals, such as gadolinium (Gd), terbium (Tb), and dysprosium (Dy), exhibit magnetic ordering at temperatures at or below ambient. Gd is trivalent with hcp structure, a half-filled $4f^7$ electron configuration, and a ferromagnetic transition below 293 K at ambient pressure [5,6]. Tb has the same number of valence electrons as Gd with hcp structure at ambient pressure, a partially filled $4f^8$ electron configuration, antiferromagnetism below 229 K, and ferromagnetism below 221 K [5,6]. Dy is also a trivalent heavy lanthanide having hcp structure at ambient pressure with a partially filled $4f^9$ electron configuration, an antiferromagnetic transition below 174 K, and ferromagnetic below 90 K [5,6]. Temperature-dependent dc electrical resistivity measurements on the heavy lanthanides Gd, Tb, and Dy have been carried out in conjunction with their dilute magnetic alloys Y(Gd), Y(Tb), and Y(Dy) under extreme pressures as high as 157 GPa (~1.6 million atmospheres). The search for possible pressure-induced magnetic instabilities in these materials was carried out over a wide pressure range spanning the pressure P_{vc} where their volume collapse occurs.

Chapter 2 provides brief theoretical and experimental background information on pressure, superconductivity, magnetism in lanthanides, and Kondo physics. Chapter 3 describes the high pressure transport measurement techniques in detail. Chapter 4 shows the results of measurements on Gd, Tb, and Dy and discusses possible mechanisms for the resultant phenomena. The thesis then ends with Chapter 5, a brief summary.

Chapter 2

Background: Theory and Experiment

The development of high pressure apparatuses like diamond anvil cell (DAC) has enabled more frequent use of pressure as a tunable parameter of condensed matter systems, much like temperature and magnetic field [7]. Many physical properties are varied when pressure is applied to the systems including magnetism and superconductivity. This chapter provides brief theoretical and experimental background information on pressure, superconductivity, magnetism in lanthanides, and Kondo physics.

2.1 Pressure

Condensed matter systems, like solids and liquids, are formed by electromagnetic forces between charged particles. Since the force is a function of distance, the physical properties of systems depend strongly on the distance between atoms (interatomic distance). By applying high pressure, an experimenter can modify the interatomic distances of a condensed matter system (see Fig. 2.1) in order to observe changes in the physical properties of that system.

In solids, the effect of changing temperature modifies the electronic occupation of energy levels, whereas the effect of changing pressure modifies the energy levels themselves [8]. At

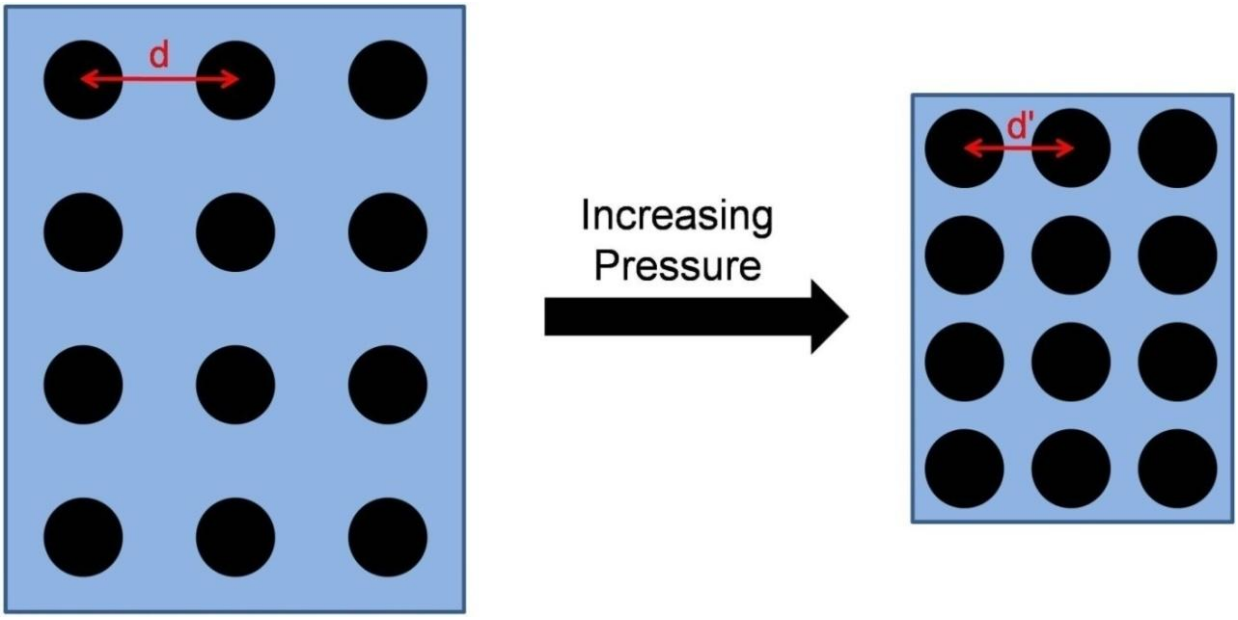

Figure 2.1: Schematic image of a metal at ambient pressure (left) and high pressure (right). Black circle represents an ion including nucleus and core electrons. Blue background represents conduction electrons in the Fermi gas. When pressure is applied, the interatomic distance decreases (d > d').

constant temperature, pressure is defined as [9]

$$P = -\left(\frac{\partial E}{\partial V}\right)_{S,N}, \tag{2.1}$$

where E is the internal energy, V is the volume, S is the entropy, and N is the number of particles in a system. This definition indicates that pressure is a measure of how the change of internal energy depends on the change of volume in the system. As pressure tunes the internal energy, the energy levels of the system, associated with interatomic distances, also change.

Emphasizing the importance of high pressure science in the study of condensed matter systems, P. W. Bridgman (1946 Nobel Laureate in Physics) wrote [10]:

"Our understanding of the condensed state cannot be regarded as satisfactory until we can give

an account of the effect of pressure on every variety of physical phenomena."

2.2 Superconductivity

In 1908 H. Kamerlingh Onnes at University of Leiden in Netherlands liquefied helium (He) for the first time [11] and opened a way to explore new physics at temperatures as low as ~1 K the boiling point of helium at reduced pressure. In 1911 he reported a new state of a mercury sample in which electrical resistance abruptly dropped to nearly zero at 4.2 K [12]. This new state of matter was what is now known as superconductivity.

2.2.1 Properties

Fig. 2.2 shows the electrical resistance of mercury (Hg) sample versus temperature from 4.4 K down to 4.15 K exhibiting an abrupt drop in resistance at 4.2 K [12]. When a simple metal is non-superconducting, its resistivity ρ is expected at low temperature (well below the Debye temperature T_D) to have the form [13]

$$\rho = \rho_d + aT^2 + bT^5 \cdots, \tag{2.2}$$

where ρ_d is the defect scattering due to impurities, aT^2 is the electron-electron scattering (Fermi liquid behavior), bT^5 is the electron-phonon scattering, a and b are constants, and T is the temperature. Simple metals, like copper or gold [13], follow Eq. 2.2 in their temperature-dependent resistivity curves.

Superconducting metals, on the other hand, undergo a thermodynamic phase transition passing through the so-called superconducting transition temperature T_c below which the resistivity abruptly vanishes:

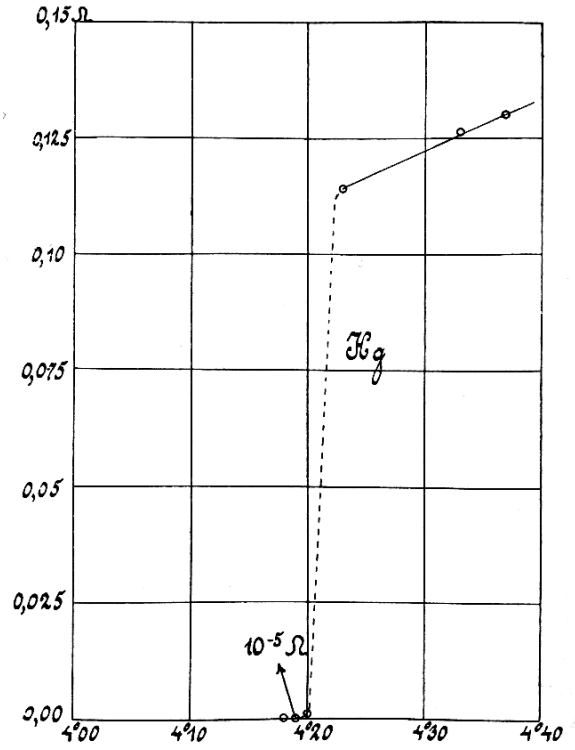

Figure 2.2: Electrical resistance of Hg versus temperature (K) measured by Onnes in 1911. The superconducting transition temperature T_c is identified by the abrupt drop to zero (less than 10^{-5} Ω) in resistance curve at ~4.2 K. Figure taken from Ref. [12].

$$\rho(T < T_c) = 0. \tag{2.3}$$

This remarkable characteristic of superconductivity leads electrical resistivity measurements as the key method to look for new superconductors, in particular under high pressure.

Superconductors also exhibit the so-called Meissner-Ochsenfeld effect [14,15] (named after two German physicists W. Meissner and R. Ochsenfeld who discovered the phenomenon in 1933) which describes the sudden expulsion of a weak applied magnetic flux inside a superconductor when cooled down below the superconducting transition temperature T_c. Thus in a superconductor below T_c, the magnetic field is not only independent of time (perfect

conductivity) but also zero everywhere inside the superconductor. As a result, a superconductor is also considered a perfect diamagnet (magnetic susceptibility $\chi = -1$ in MKS units).

2.2.2 BCS Theory

Following the discovery of superconductivity in 1911, many scientists attempted to formulate a fundamental theory of superconductivity from the early framework of quantum mechanics [11]. Phenomenological theories were developed in conjunction with further experimental realization of superconductivity such as the Meissner-Ochsenfeld effect and the isotope effect ($T_c \propto M^{-\alpha}$, where M is the mass of the cation and α is the isotope exponent [13]).

In 1957 almost 50 years after Onnes' discovery of superconductivity in Hg, John Bardeen, Leon Cooper, and J. Robert Schrieffer (BCS theory) at the University of Illinois formulated a microscopic theory of superconductivity [16]. In this model, electrons are paired (Cooper pairs) to occupy a single-particle ground state through a weak attractive force mediated by electron-phonon interaction. The system becomes most energetically favorable in a stable pair bound state [16]. The BCS theory successfully accounted for many superconducting phenomena including the isotope effect and made valuable new predictions such as the presence of an energy gap 2Δ at the Fermi level E_F where Δ is the gap parameter [16].

Fig. 2.3 illustrates how the effective interaction between electrons can be attractive rather than repulsive in a crystal lattice. In this example, an electron passes between the ions in the lattice. Due to Coulomb attraction, the positive cations are pulled toward the electron and excited by a phonon mode (the lattice vibration). Then, a localized region with excessive positive charge density develops. Since the excited cations are relatively heavy, they are pulled back rather slowly while the electron moves away. Without the electron, the region of excessive positive

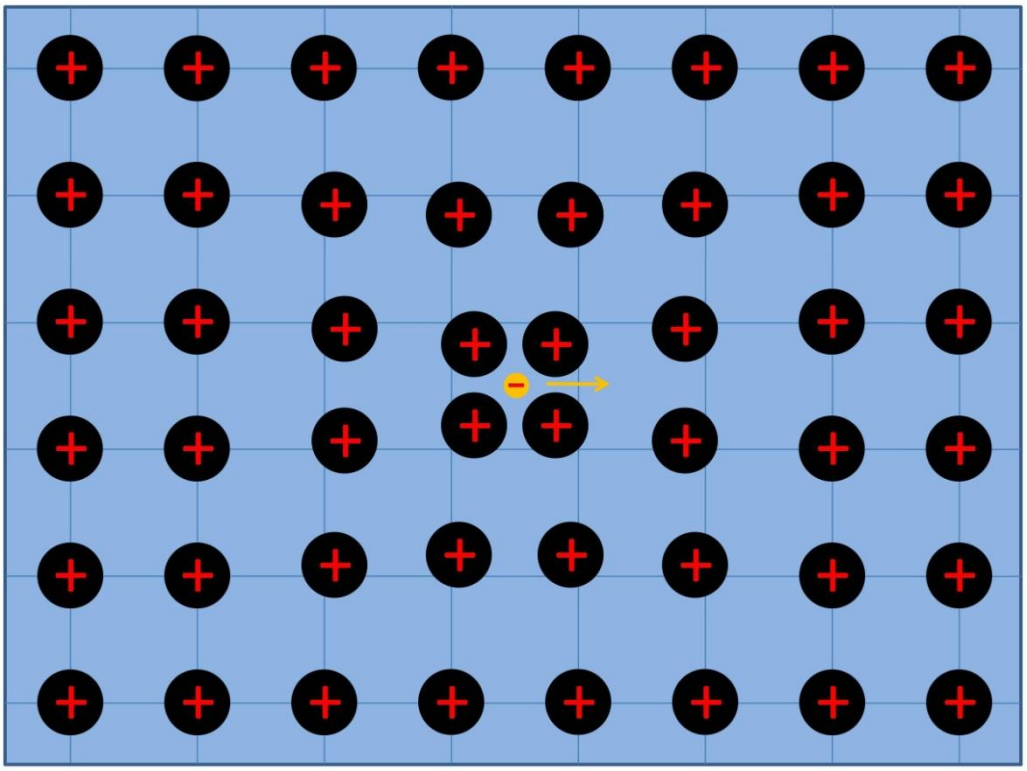

Figure 2.3: Schematic illustration of the electron-phonon interaction leading cooper pairs. Black big circles with a positive charge represent cations. The orange small circle represents an electron in the conduction band (arrow refers to moving direction of the electron). Blue horizontal and vertical lines illustrate the crystal lattice.

density still remains. A second electron is then attracted to the region. This can drive an effective attractive interaction between those two electrons to pair them together: the so-called Cooper pair.

BCS theory quantitatively predicts various properties of superconductivity, including critical temperature, energy gap, critical field, specific heat, and the isotope effect [15]. According to BCS theory, in the limit of weak electron-phonon coupling, the superconducting transition temperature T_c is given by [1,16]

$$T_c = 1.14\left(\frac{\hbar\omega_D}{k_B}\right)\exp\left[-\frac{1}{N(E_F)V_{eff}}\right], \tag{2.4}$$

where $\hbar$ is the reduced Planck constant, ω_D is the Debye frequency, k_B is the Boltzmann constant, $N(E_F)$ is the density of states at the Fermi level, and V_{eff} is the effective attractive (positive) potential between the electron-electron pair (Cooper pair). The zero-temperature energy gap is given by [1,16]

$$2\Delta(0) = 4\hbar\omega_D\exp\left[-\frac{1}{N(E_F)V_{eff}}\right]. \tag{2.5}$$

The ratio of Eq. 2.5 to 2.4 provides the famous BCS prediction regarding a fundamental constant

$$\frac{2\Delta(0)}{k_B T_c} = 3.52. \tag{2.6}$$

This result agrees very well with experimental data for a wide range of superconductors. For example, the value of the ratio Eq. 2.6 for aluminum (Al) and indium (In) gives 3.4 and 3.6 respectively according to experiments [15].

2.2.3 Effect of Pressure on Superconductivity

BCS theory appears to predict the pressure dependence of the superconducting transition temperature $T_c(P)$. The BCS prediction for T_c given by Eq. 2.4 can be rewritten as [1,17,18]

$$T_c = 1.14\left(\frac{\hbar}{k_B}\right)\langle\omega\rangle\exp\left[-\frac{1}{\lambda-\mu^*}\right] = 1.14\left(\frac{\hbar}{k_B}\right)\sqrt{\frac{k}{M}}\exp\left[-\frac{k}{\eta}\right], \tag{2.7}$$

assuming $\mu^* = 0$ since $\mu^* \approx 0.1 \ll \lambda$ and using the relations $\omega_D \approx \langle\omega\rangle \approx \sqrt{k/M}$, $M\langle\omega^2\rangle \approx M\langle\omega\rangle^2 \approx k$, and $\lambda = \eta/M\langle\omega^2\rangle = \eta/k$, where $\langle\omega\rangle$ is the average phonon frequency, λ is the

electron-phonon coupling constant, μ^* is the Coulomb pseudopotential (Coulomb repulsion between the electrons), k is the lattice spring constant, M is the mass of cation, and $\eta \equiv N(E_F)\langle I^2 \rangle$ is the Hopfield parameter [19] ($\langle I^2 \rangle$ is the average square electronic matrix element), which is a purely electronic term. The values of k and η increase under pressure due to lattice stiffening and proportional behavior to $(V_o/V)^{\varphi}$ respectively, where V_o and V are the volume at ambient and high pressure respectively and φ is the empirical (positive) parameter [20]. Since the increase of k in the exponent dominates over the prefactor $\sqrt{k}$, the overall pressure-dependent T_c may vary according to the relative values of k and η. In the simple *sp*-electron superconductors (aluminum (Al), zinc (Zn), indium (In), tin (Sn), and lead (Pb)), T_c rapidly decreases as a function of pressure due to the more rapid increase in k than in η. On the other hand, in some transition metals [21] $T_c(P)$ increases since η increases more rapidly than k.

Fig. 2.4 shows a periodic table showing elemental superconductors and the values of the superconducting transition temperature T_c at ambient and high pressures [22,23]. At ambient pressure 30 elemental solids become superconducting at sufficiently low temperatures (yellow in Fig. 2.4). An additional 23 elements, which are not superconducting at ambient pressure, are induced to become superconductors by applying high pressure (light green with bold outline in Fig. 2.4).

2.3 Magnetism in Lanthanides

Among all elements in the periodic table, 76 elements have a permanent magnetic dipole moment in their neutral atomic state like a gas or vapor. However, when these elements are condensed into a solid, only 24 of them retain their magnetism [24]. The 4*f*-series of lanthanide

Periodic Table of Superconductivity

(dedicated to the memory of Bernd Matthias; compiled by James S. Schilling)

30 elements superconduct at ambient pressure, 23 more superconduct at high pressure.

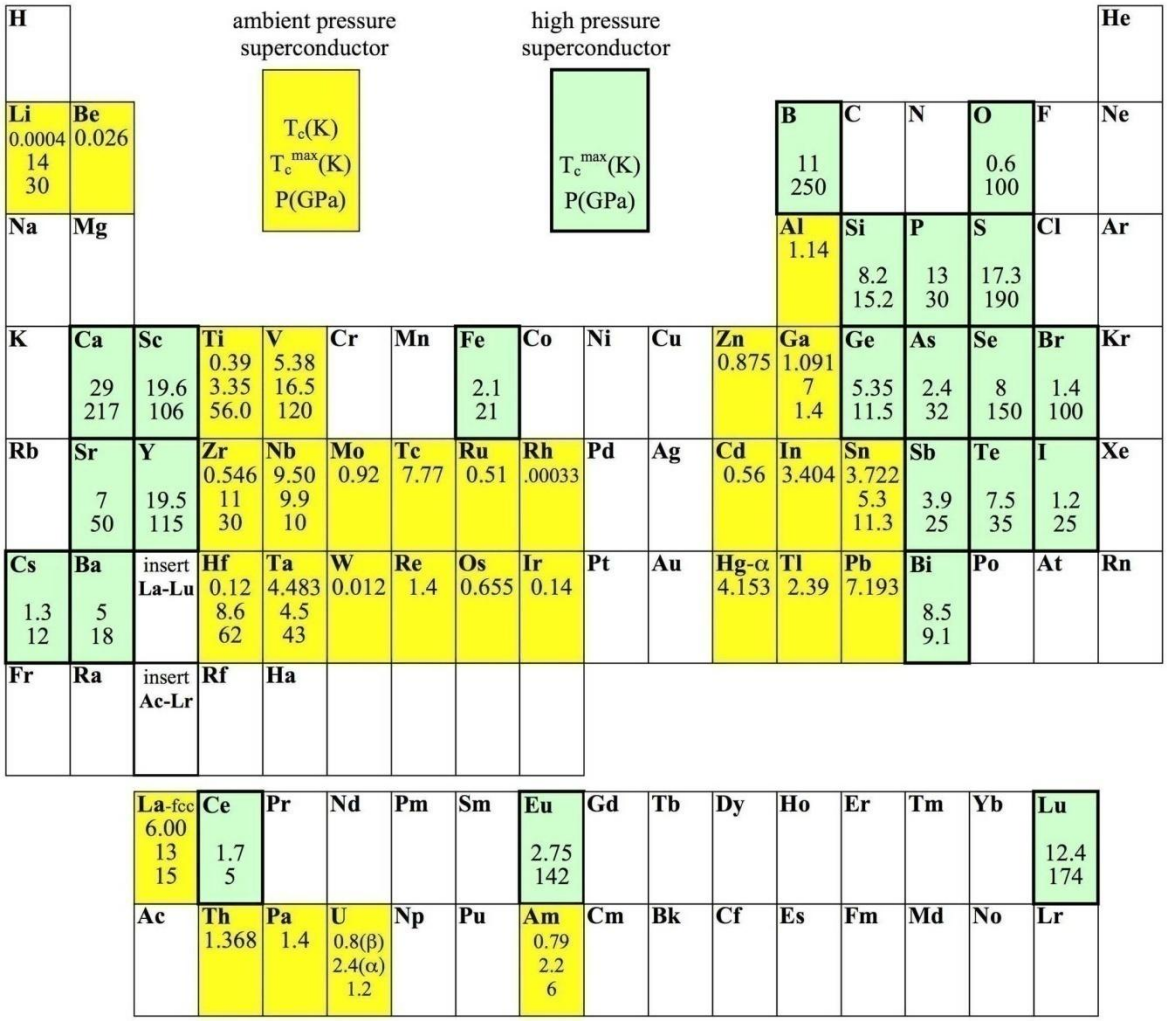

Figure 2.4: Periodic table of elemental superconductors. Yellow region represents elements which become superconducting at ambient pressure. Light green region represents superconductors only at high pressures. For each element the upper value refers to T_c at ambient pressure; the middle value refers to T_c^{max} at high pressures of which the corresponding values are described at the lower position. Figure taken from Ref. [22].

metals have the most successful rate in retaining their magnetism due to the high degree of localization of their 4*f* orbitals.

2.3.1 Strongly Localized 4*f*-Electrons

Fig 2.5 shows the normalized radial charge density of gadolinium ion (Gd^{3+}) versus distance *R* from the nucleus given by solving the Hartree-Fock equations [25–27]. The orange dashed line marks half distance of nearest Gd^{3+} neighbors. 4*f*, 5*s*, 5*p*, 5*d*, and 6*s* refer to the different orbital levels. Since the 6*s* and 5*d* orbitals have significant overlap with the same orbitals of the nearest neighbor, as seen in Fig. 2.5, they form conduction electrons and contribute to crystal binding. On the other hand, it is clear that 4*f*-orbital electrons are embedded close to the nuclei leading to the strongly localized electron behavior that retains magnetism.

2.3.2 RKKY Interaction

The magnetic ordering of 4*f* local moment in the heavy lanthanides is known to be governed by the indirect RKKY (Ruderman-Kittel-Kasuya-Yosida) exchange interaction [28], a magnetic interaction between localized magnetic moments mediated by the surrounding conduction electrons. This exchange interaction can be expressed to the Heisenberg Exchange Hamiltonian $H_{ij} = -2J_{ij}\mathbf{S}_i \cdot \mathbf{S}_j$, where J_{ij} is the exchange coupling constant and $\mathbf{S}_i$ is the vector spin operator for spin S of the i^{th} ion [15].

The exchange interaction is related to spins, but because of spin-orbit interaction in the heavy lanthanides, it is necessary to use total angular momentum **J** by projecting spin angular momentum **S** on to it. Using the Wigner-Eckart theorem $\mathbf{L} + 2\mathbf{S} = g_J\mathbf{J}$ as well as the relation $\mathbf{L} + \mathbf{S} = \mathbf{J}$, one can replace the spin operator by $\mathbf{S}_i = (g_J - 1)\mathbf{J}_i$ [29], where **L** is the orbital angular momentum and g_J is the Landé *g*-factor. Then, the magnetic ordering temperature T_o, with the

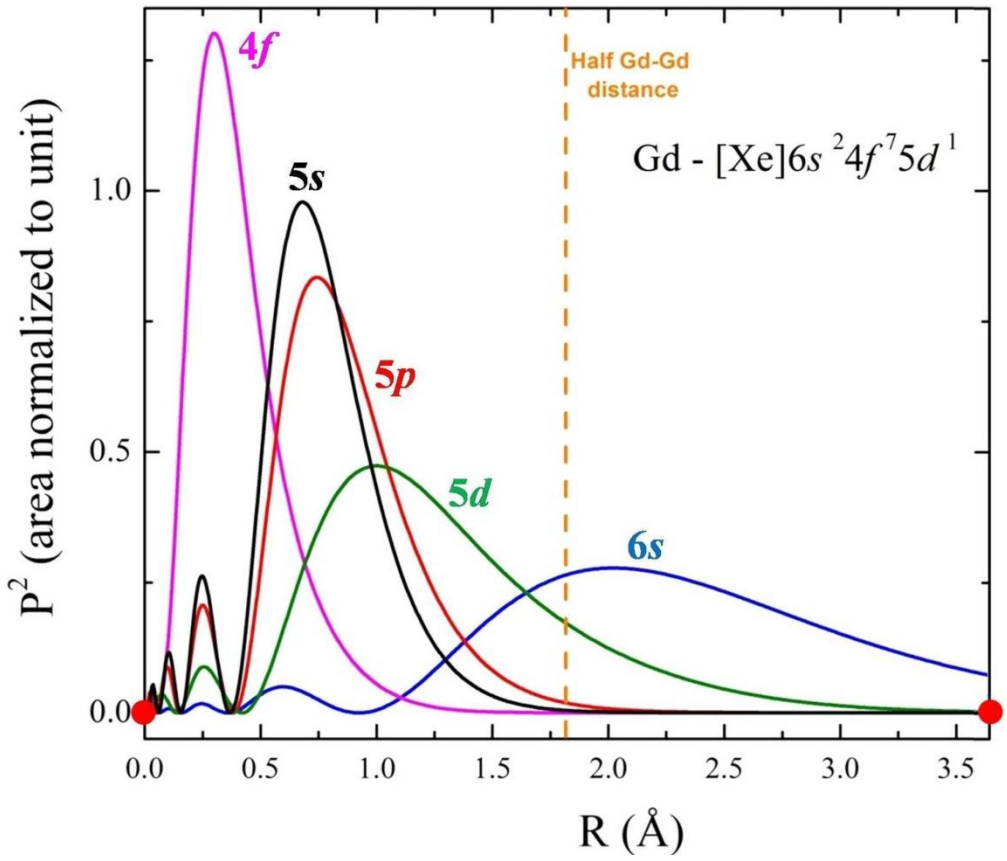

Figure 2.5: Normalized radial charge density versus distance R from the nucleus (red circle) of a Gd^{3+} ion. 4*f*, 5*s*, 5*p*, 5*d*, and 6*s* refer to the different orbital levels. The orange dashed line marks half distance of nearest Gd^{3+} neighbors. Figure taken and modified from Refs. [25–27].

aid of the Weiss molecular field theory, is expected to have the form [30]

$$T_o = \frac{1}{k_B} 2\pi z J^2 \left\{ (g_J - 1)^2 J_t (J_t + 1) \right\} N(E_F) \sum_{\mathbf{R}_i \neq \mathbf{R}_j} \phi\left(2k_F |\mathbf{R}_i - \mathbf{R}_j|\right), \tag{2.8}$$

where k_B is the Boltzmann constant, z is the number of conduction electrons per atomic volume, J is the exchange coupling constant (from the RKKY approximation), J_t is the total angular momentum quantum number, $N(E_F)$ is the density of states at the Fermi level, $\phi(x) = (\sin x - x \cos x)/x^4$, k_F is the Fermi wave number, and $\mathbf{R}_i$ is the position vector for spin S_i.

Eq. 2.8 predicts that at ambient pressure the magnetic ordering temperature T_o of the heavy lanthanides would be proportional to the term $(g_J - 1)^2 J_t(J_t+1)$, which is known as the so-called de Gennes factor. For example, Gd has the highest value of T_o = 292 K [6] among the heavy lanthanides (see Fig. 4.5), as it has the largest de Gennes factor of 15.75 (see Table 4.1).

2.4 Kondo Physics

In 1930 W. Meissner and G. Voigt [31] found that the temperature-dependent resistivity of gold (Au) has a minimum feature (the so-called resistance minimum) at a low temperature around 10 K instead of decreasing monotonically with decreasing temperature, as expected from the Bloch-Grüneisen model (Eq. 2.2). The same phenomena was subsequently found in many dilute magnetic alloys, leading J. Kondo [32] to formulate the existence of strong coupling between the conduction electrons and the local magnetic impurity in 1963, which is known as the Kondo effect.

2.4.1 Kondo Effect

At high temperature dilute magnetic impurities in a non-magnetic metal host weakly couple with conduction electrons. However, near the characteristic Kondo temperature T_K, the interaction becomes very strong such that the local magnetic impurity is compensated by spins of the surrounding conduction electrons (Kondo screening). Kondo suggested the *s-d* exchange interaction $H_{s\text{-}d} = -J_{\text{eff}}\mathbf{s}\cdot\mathbf{S}$ [33] for dilute magnetic alloys, where $\mathbf{s}$ is the spin operator of conduction electrons, $\mathbf{S}$ is the spin operator of magnetic impurities, and J_{eff} is the effective exchange constant. By taking the *s-d* exchange interaction as a perturbation to third order, he found that magnetic impurity scattering increases logarithmically with decreasing temperature (Kondo effect) with the form [32]

$$\rho_{\text{spin}} = a\rho_{\text{sd}} + bJ_{\text{eff}}\log T. \quad (2.9)$$

where a and b are positive constants, ρ_{sd} is the spin-disorder scattering. When J_{eff} is negative (antiferromagnetic coupling between **s** and **S**), the resultant resistivity is divergent at low enough temperatures. Together with the phonon scattering (see Eq. 2.2), it gives rise to a resistivity (resistance) minimum.

2.4.2 Kondo Pair Breaking

In 1969 Maple, Wittig, and Kim [34] carried out high pressure experiments to test for the presence of Kondo effect phenomena by alloying dilute magnetic impurities into a superconducting host instead of a non-magnetic one. They found that the superconducting transition temperature T_c in lanthanum (La) was strongly suppressed by the dilute magnetic cerium (Ce) ions showing a characteristic sinkhole-like suppression across the pressure at 0.7 GPa, where Ce suffers 16% volume collapse [35] (see Fig. 4.6). Such a strong suppression of superconductivity indicates strong antiferromagnetic coupling (Kondo effect) between spins of conduction electrons and magnetic impurities causing separation of the Cooper pairs (see Section 2.2.2). This is known as pair breaking by the Kondo effect or Kondo pair breaking. Fig. 2.6 shows a schematic illustration of the Kondo pair breaking in a superconducting host by dilute magnetic impurities.

2.4.3 Kondo Lattice

In 1977 Doniach [36,37] proposed a lattice version of the Kondo effect, which is widely used to explain the properties of heavy fermion systems [24,38,39]. In this Kondo Lattice Model (KLM), every ion with a local moment in a crystalline lattice participates in the strong coupling with the spins of the surrounding conduction electrons. Doniach calculated the one dimensional

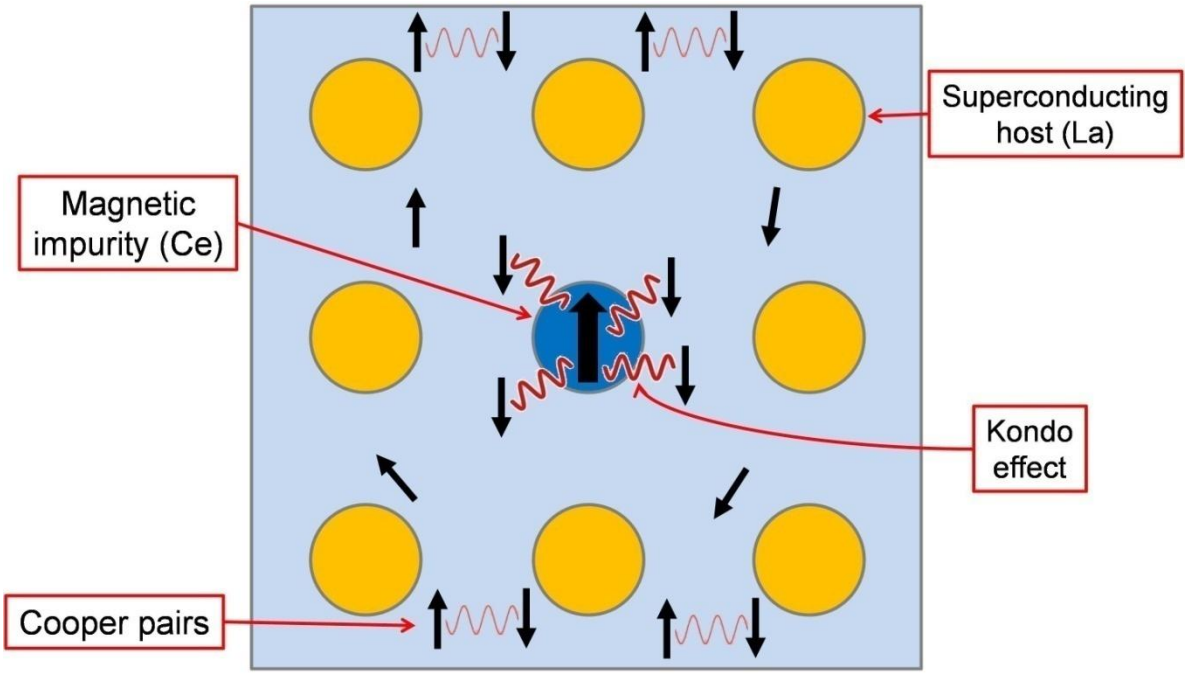

Figure 2.6: Schematic illustration of Kondo pair breaking in superconducting host La by magnetic impurity Ce. Yellow circle represents the La^{3+} ion. Blue circle with a local moment in it represents the magnetic impurity Ce^{3+} ion. Black arrow represents spin of the conduction electron. Light red spring refers to the weak attractive interaction of Cooper pairs. Red spring refers to the strong interaction of Kondo effect, which breaks up the Cooper pairs. Note that real spacing of Cooper pairs is about several hundred times greater than that of ions.

Kondo lattice problem by using the mean field approximation and suggested a simple phase diagram for Kondo lattice model, as seen in Fig. 2.7. The competition between the RKKY interaction and the Kondo interaction leads the system into magnetic instability and quenches the magnetic ordering. In the RKKY interaction, T_{RKKY} (T_{o} in Section 2.3.2) is proportional to two terms [30]

$$T_{\mathrm{RKKY}} \propto J^2 N(E_{\mathrm{F}}), \tag{2.10}$$

where $N(E_{\mathrm{F}})$ is the density of states at the Fermi level and J is the exchange coupling constant. In the Kondo interaction, T_{K} is expressed as [24]

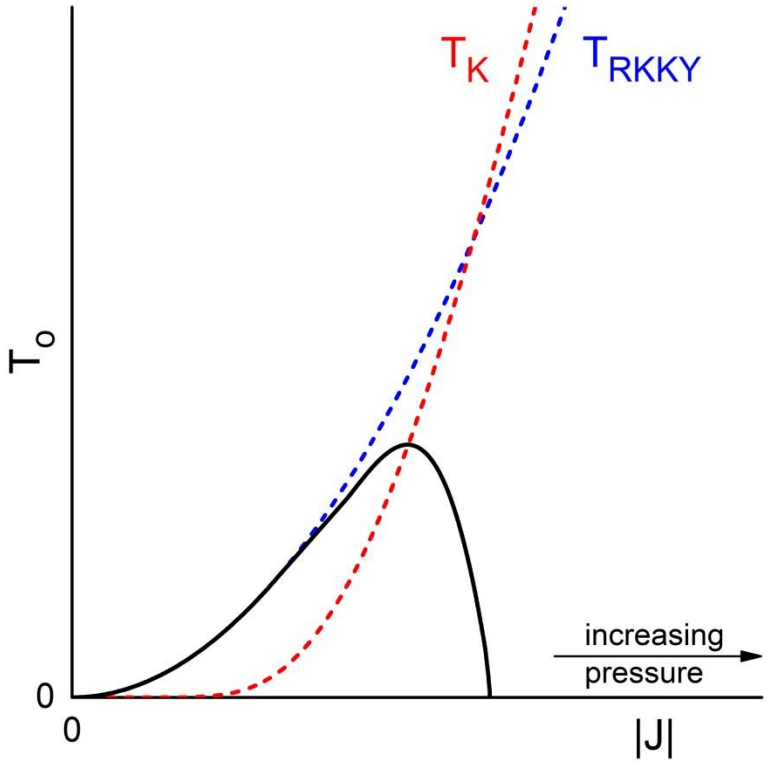

Figure 2.7: Schematic phase diagram of the Kondo lattice model proposed by S. Doniach [36]. Black curve denotes the magnetic ordering temperature T_o of the Kondo lattice behavior with increasing $|J|$ or pressure.

$$T_K \propto \exp\left[\frac{-1}{|J|N(E_F)}\right]. \tag{2.11}$$

Chapter 3

Experimental Apparatus and Methods

As a topic of Ph.D. research, the electronic and magnetic phases of selected heavy lanthanide metals were studied under extreme pressure conditions using diamond anvil cells (DAC). High pressure transport measurements were carried out such as direct current (dc) electrical resistivity and alternating current (ac) magnetic susceptibility. Successful measurements depend on the level of preparation in all the aspects of experimental setups with great details. This chapter will describe the high pressure transport measurement techniques, including some technical improvements to enhance the quality of measurements.

3.1 Diamond Anvil

In the Middle Ages, metal workers used anvils and hammers to make weapons for battle. They fashioned hardened swords and armor from hot bulk metal, pounding by hammer on extremely hard anvils (usually made of a massive block of iron [40]). In a similar way, a diamond anvil (typically a millimeter sized, see Fig. 3.1) is an anvil on which tiny materials can be pressed and deformed using nature's hardest material ever known "diamond" (recently an artificial nanotwinned diamond was fabricated and reported to have higher hardness than

diamonds in nature [41]). It is important to appreciate that the properties of diamond enable many interesting physical phenomena to be explored under non-ambient conditions (ambient conditions refer to, in general, room temperature at 300 K and atmospheric pressure at 100 kPa).

Diamond is an allotrope of carbon (C), which forms at high pressure and temperature conditions (metastable phases), just as graphite is another allotrope of carbon at ambient conditions. The crystal structure of diamond is overall face-centered cubic in the unit cell, but in the primitive cell the carbon atoms are tetrahedrally bonded, giving it the name "diamond structure" among other materials with the same structure [42]. The extreme properties of diamond are mostly due to the strong covalent bonding between carbon atoms.

The exceptional thing about diamond, as a tool in the study of high pressure science, is its hardness—the highest among any other bulk materials in nature; for example, diamond measures at 45.3 HV, as compared to 4.59 HV for quenched steel in units of GPa [GN/m^2], according to the Vickers Hardness test [42]. Diamond also has excellent thermal conductivity, which allows accurate temperature measurements *in situ* at non-ambient temperature conditions. Its low thermal expansion provides stable pressure environments during cooling and heating processes. Diamond is an excellent electrical insulator (a wide bandgap of 5.5 eV), enabling electrical conductivity measurements on materials [43]. Pure diamond is transparent in the visible range (see Fig. 3.1), which allows observation of any change in the optical properties of the samples during compression. It is also roughly transparent to both soft and hard x-rays, with photon energies in the range from 100 eV to 100 keV, supporting x-ray spectroscopy as a valuable radiation probe for materials under high pressure—though a limitation is posed by the diamond thicknesses (this has led to adoption of perforated designs of diamond; for more information on

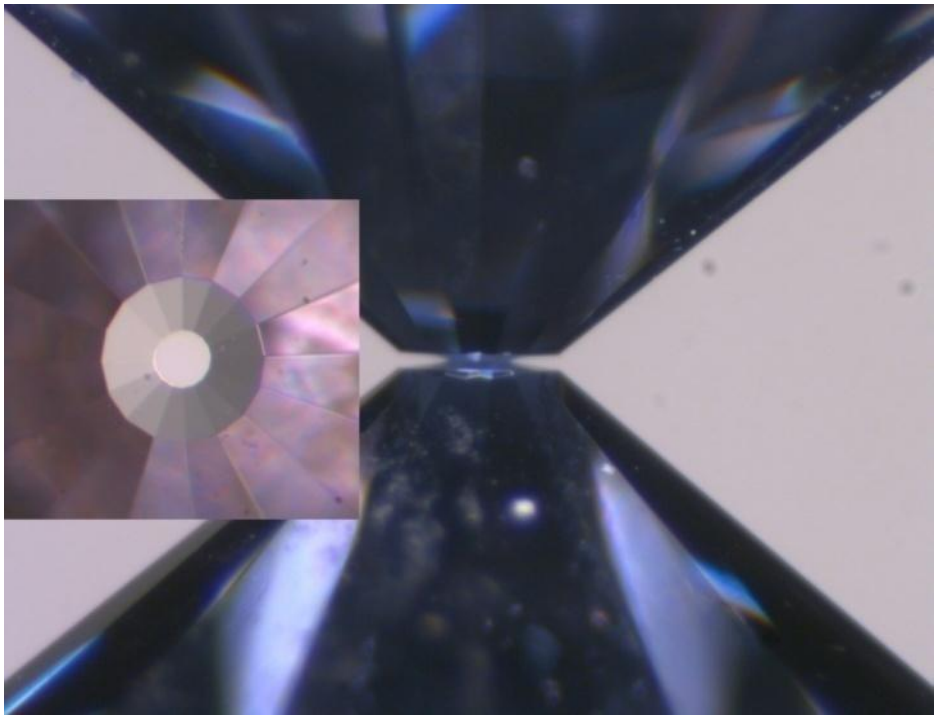

Figure 3.1: Image of two opposing diamond anvils touching each other on the central flat of the culet (300 μm diameter culet beveled at 8° to a 100 μm central flat). The inset shows a view of the beveled culet looking through the table of the upper diamond thanks to its transparency to visible light. Figure taken from Ref. [44].

enhancement of x-ray transmission by altering diamond geometry, see Refs. [45,46]).

Even though diamond has many good and excellent characteristics for high pressure science as discussed above, there are also some drawbacks. At ambient temperature, diamond is chemically very stable, meaning that it is hardly reactive to any other materials. However, when it reaches high temperatures, it becomes relatively unstable. For example, natural diamond begins to oxidize in air at around 1100 K, making its application limited at high temperature conditions [47]. Most of all, use of a small size of diamond anvil (typically less than 1 mm culet in diameter, see Fig. 3.1) limits sample volume to be extremely small (less than 300 μm in

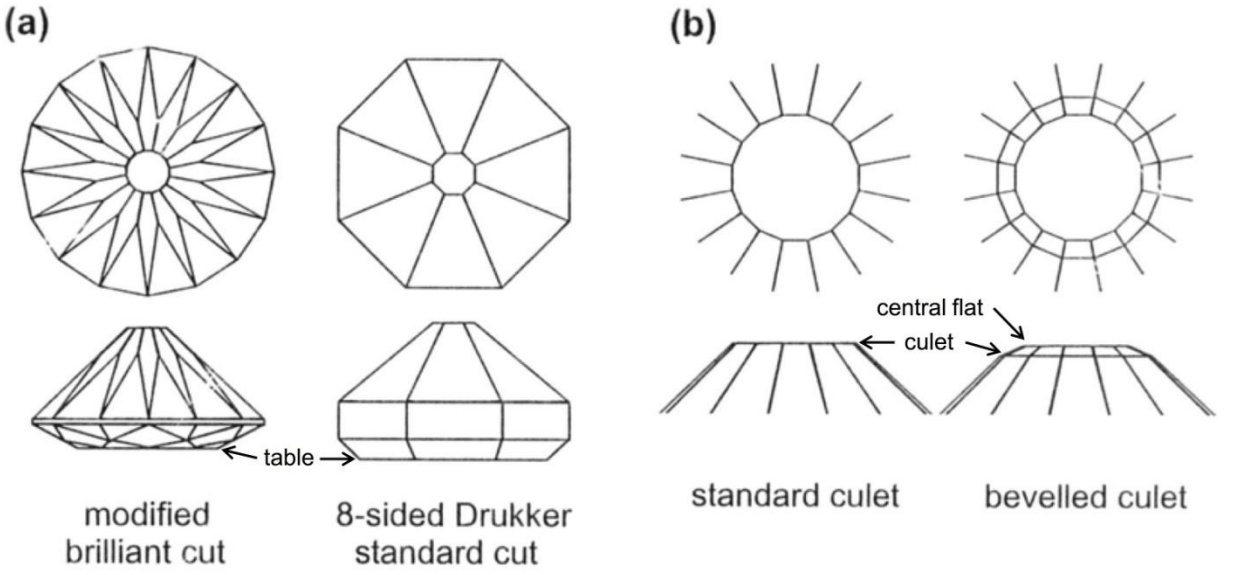

Figure 3.2: Diamond anvil types. (a) Shapes of diamond anvils (arrows mark the table of diamond). (b) Culet designs (arrows mark the culet and central flat of diamond respectively). Figure modified from Ref. [48].

diameter), leaving significant challenges in preparing experiment setups.

Several types of diamond anvil designs may be seen in Fig 3.2(a) and (b). The modified brilliant cut is the early design of anvils, which is also widely used to maximize reflection and dispersion for jewelry and other adornment purposes. The Drukker cut was designed to provide superior strength over the brilliant cut for the same carat (weight). For example, as seen in Fig. 3.2(a), the diamond table (the base of the diamond parallel to the culet) of a Drukker cut becomes enlarged and the anvil angle to the culet is increased in comparison to the modified brilliant cut. In Fig. 3.2(b), although the standard culet may be used for high pressure, much higher pressures can be achieved by using the beveled culet, a modification that reduces stress on the culet edges and gives additional support for the central flat. Generating maximum pressure on samples critically depends on the culet (or central flat) sizes. The smaller the size used, the

Table 3.1 Maximum pressures (P_{max}) reached in our laboratory are presented for varying diamond culet size and experiment conditions. Culet face diameters are listed for flat and beveled (b) geometries; initial gasket thickness is 250 μm (for information on gasket, refer to Section 3.2.2). Pressure media are listed with *NPM* indicating no pressure medium. Pressure gauges are indicated for ruby fluorescence (RF) and diamond vibron (DV). *T* indicates temperature at which sample pressure was measured. Note that 1 GPa = 10 kbar and that the 180 μm diamond culet size is used twice as a reference to compare dc resistivity technique (cBN + epoxy, see Section 3.3.3).

P_{max} (GPa)	Diamond culet diameter (μm)	Gasket material	Indented gasket thickness (μm)	Gasket hole diameter (μm)	Pressure medium	Sample	Pressure gauge	*T* (K)	Ref.
10	900	CuBe	100	450	He	$LaRu_2P_2$	RF	10	[49]
67	500	Re	70	250	He	Li	RF	20	[50]
89	300	Re	50	150	He	Y	RF	20	[51]
174	180(b)	$W_{0.75}Re_{0.25}$	30	90	*NPM*	Lu	DV	297	[52]
157	180(b)	Re	30	80	cBN + epoxy	Dy	DV	297	[53]
209	100(b)	Re	20	50	*NPM*	C_6H_6	DV	297	[54]

higher the pressure that can be reached. The maximum pressures reached in our laboratory are listed by diamond anvil culet sizes in Table 3.1.

Diamond can be categorized into two kinds, type I and type II [55], depending on the degree and behavior of impurities. The former has a significant amount (≥0.1%) of nitrogen (N) impurities and can be further divided into two groups, type Ia and type Ib according to the nature of nitrogen impurity mixture. Type II diamonds have an insignificant amount of nitrogen impurities and are further classified as type IIa or type IIb according to electrical conductivity. Most high pressure experiments using diamond anvils utilize type Ia, including this research.

3.2 Pre-Preparation for Diamond Anvil Cell

A high pressure experiment device using diamond anvils is the so-called “Diamond Anvil

Cell (DAC)" as shown in Fig 3.3. Depending on the nature of measurements and sample properties, the corresponding setups are constructed differently inside the cell assembly. As far as the generation of high pressure is concerned, however, some aspects remain the same. Those are the alignment of the two opposing diamond culets and gasket preparation (how the gaskets are used in DAC may be seen in Fig 3.5).

3.2.1 Fine Alignment of Diamond Anvils

High pressures require precise alignment of diamond culets. The cause of diamond fracture under extreme pressures results mostly from the misalignment of the diamond culets. Prior to alignment, their surface must be cleaned thoroughly under a stereo microscope to prevent dust from obscuring the degree of misalignment. Cleaning the culet surface with cotton swabs (much bigger than the size of culet) which absorb methanol or ethanol (but not acetone because it can dissolve the glue used for mounting diamonds) is a challenging task since the culet is sub-millimeter sized. Experience indicates better results with smaller amounts of methanol and minimal swabbing repetitions.

Generally the alignment of diamond culets is performed under a stereo microscope and can be checked further with a metallurgical microscope. There are typically three types of alignments depending on the design of the DAC: translational, rotational, and planar alignments. The following description of fine diamond culet alignments is based on the DAC designed by James S. Schilling [56] and may be seen in Fig. 3.3. Before beginning to work on the alignment, all the screws which hold and adjust both adjustment plate and adjustment hemisphere (Fig. 3.3(a)) should be finger tight to prevent loosening or overtightening (assuming both diamonds are already mounted on the adjustment plate and adjustment hemisphere). Both the adjustment plate

(a)

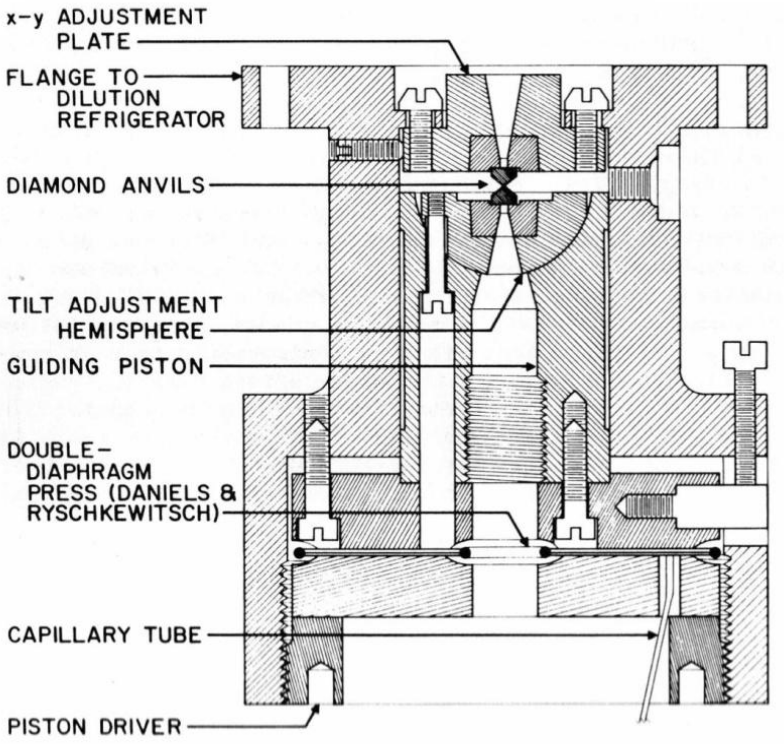

(b)

Figure 3.3: Diamond anvil cell (DAC) designed by James S. Schilling. (a) Cross-sectional schematic picture of the DAC. (b) Actual image of DAC components: (from the upper left) piston, body, (from the lower left) force plate (which is placed between diaphragm and piston driver, see Fig. 3.3(a)), piston driver, and torquing tool (for piston driver). Figures taken from Refs. [56] and [57] respectively.

and adjustment hemisphere should also be roughly aligned before closing the cell by inserting the piston into body, see Fig. 3.3.

The translational (X-Y directional) alignment process is the most straightforward of the three. After bringing the two diamonds close together (~5 μm apart), two slightly unmatched diamond culets may be seen through the upper diamond using a stereo microscope. A series of translational adjustments of the adjustment plate may be required so that the two opposing diamond culets perfectly contact each other.

Rotational alignment is performed by loosening the two screws that hold the adjustment plate and the other three screws that make the translational adjustment. This allows the adjustment plate to rotate a few degrees. All screws should be finger tightened after each alignment adjustment. Note, however, that rotational alignment is typically unnecessary when both diamonds are mounted and glued together such that their facets point in the same direction.

The final and most critical stage of diamond alignment is the planar alignment. After the translational and rotational alignments are finished, the two diamonds are gently brought together in contact at the culet (or central flat) surfaces as seen in Fig. 3.1. Since those surfaces are not yet perfectly aligned (i.e., not yet precisely parallel), interference fringes (rainbow colors) will appear on the culet surface. These are called “Newton’s rings” [58], Fig 3.4(a). The fringes are observed on the culet surface of the upper diamond due to the interference of reflected light from the two culet surfaces which are in contact only at specific angles.

Here we describe how to determine where the surfaces meet. After observing the interference pattern on the culet surface, the pattern will slowly move in a specific direction as the diamonds are gently pulled apart. When once again brought into contact, the moving

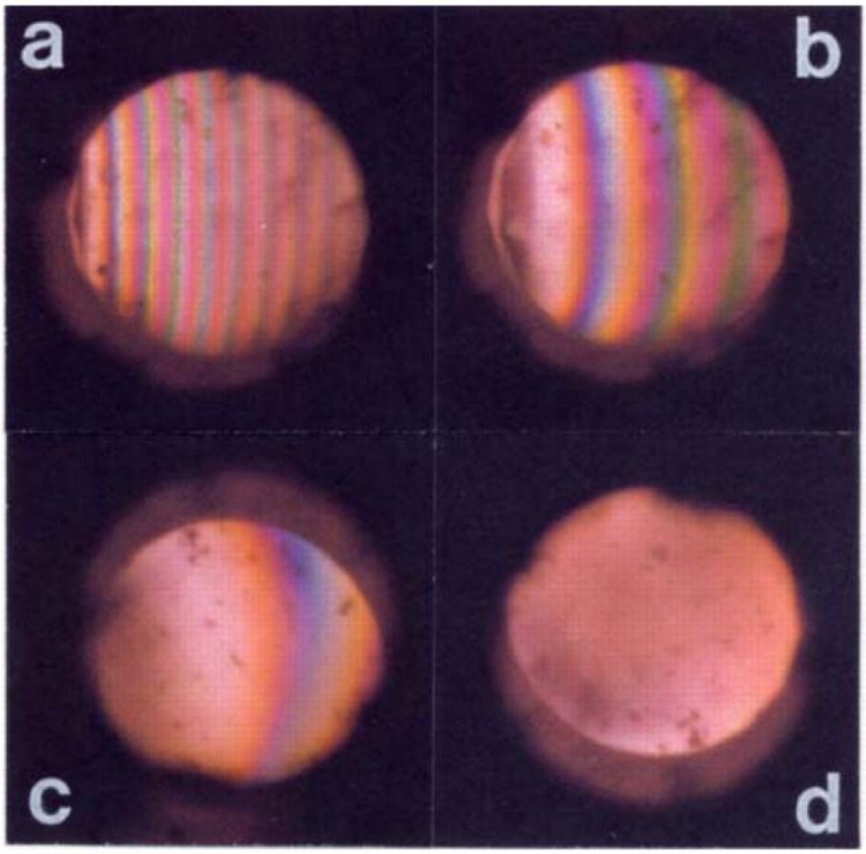

Figure 3.4: Images of disappearing Newton's interference fringes on two opposing diamond culets which are in contact during planar alignment (parallelization). (a) Initial stage of the planar alignment showing appearance of significant Newton's interference. (b) Reduced fringes after one stage of alignment. (c) Fair alignment leaving just one fringe. (d) Fine alignment (absolutely parallel culet surfaces of two diamonds) yields a homogeneous grey color. Image taken from Ref. [48].

direction of the fringes on the culet surface indicates where the two culet surfaces are touching. The tilt of the hemisphere (see Fig. 3.3(a)) should be adjusted accordingly. Tightening one of the three screws attached to the hemisphere will pull the hemisphere on that side and make the culet surfaces more parallel. Successive adjustments will decrease the number of fringes, as seen in Figs. 3.4(b) and (c), until only one homogeneous grey color remains on the culet surface, as seen in Fig 3.4(d). This final state indicates that the two culet surfaces are sufficiently parallel to each

other.

After finishing all three alignments, it is recommended to double-check them by pre-indenting (see Fig. 3.5) a gasket (for example, a stainless steel gasket) with the aligned diamond anvils and by drilling a hole at the center of the indented gasket. The pre-indented gasket shows the imprint of two culet surfaces on both front and back sides, and the relative position of the drilled hole on the imprinted culet surfaces of the gasket indicates the translational misalignment of the diamond culets. For example, if the drilled hole is at the center of the imprinted culet surface on front side gasket but not centered on the back side, there is a translational misalignment since the hole is straight through the gasket. To achieve high pressure, misalignment of less than 5% of the culet diameter is strongly recommended.

3.2.2 Gasket Pre-Indentation

A pre-indented metal gasket with a bore at the center and two opposing diamond culets form a pressure chamber in the DAC into which the sample, pressure calibrating material, and pressure medium are placed, as seen in Fig. 3.5(a). It is important to note that the proper choice of gasket material (for example, suitable hardness and ductility), the pre-indented gasket thickness, and the gasket hole size all play a vital role in achieving highest pressure on a sample [59].

For this thesis work, for ac magnetic susceptibility measurements, either rhenium (Re) or copper beryllium (CuBe) gaskets were used depending on the superconducting transition temperature T_c of samples. Re gaskets superconduct at around 1.7 K [60] at ambient pressure and at approximately 4 K under strain [61], obscuring sample signals below 4 K, whereas CuBe gaskets, due to their non-magnetic and non-superconducting properties, allow measurements to

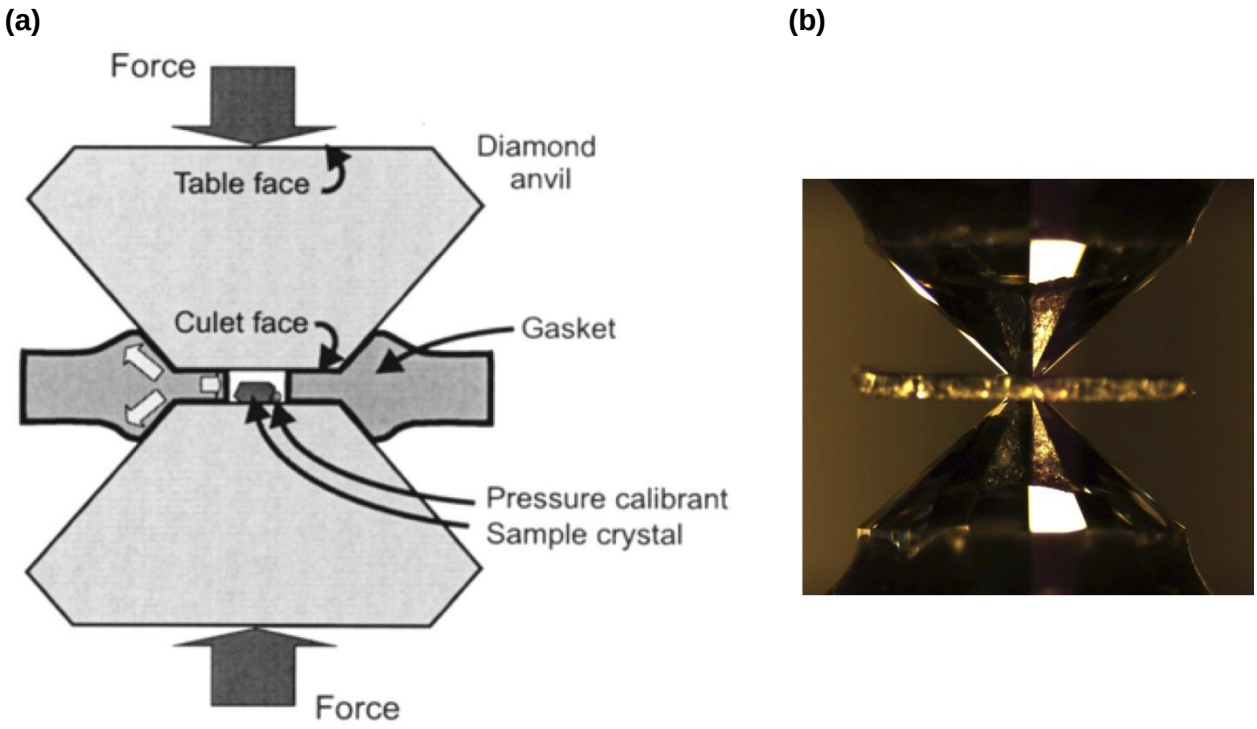

Figure 3.5: Images of the pre-indented metal gaskets. (a) Schematic picture of the pressure chamber made by the pre-indented and centrally drilled gasket (together with the two opposing diamond culet surfaces) which accommodates the sample, pressure calibrant, and pressure medium. (b) Actual image of the gasket pre-indentation. Images taken from Refs. [48] and [62] respectively.

be performed at the lowest available temperatures—as low as 1.3 K, limited by the liquid helium (LHe) cryostat. For high pressure dc electrical resistivity measurements, Re gaskets were often used not only due to its hardness (5.35 HV in units of GPa [GN/m^2] [1]) but also because of the nature of the resistivity measurement, where the sample is electrically isolated (insulated) from the metal gasket, leaving no ambiguity about an artifact superconducting signal from the Re gasket below 4 K.

The dimensions of the pre-indented gasket and the drilled hole at the center are as follows. For the ac magnetic susceptibility measurements, gaskets with 2.8 mm in diameter are punched

from a metal foil (either Re or CuBe with an initial thickness of 250 μm) since they must be able to go inside the coil system (3.46 mm in inner diameter, see Fig 3.7). For the dc electrical resistivity measurements, gaskets with 7 mm in diameter, as seen in Fig. 3.11(f), were cut from a metal foil (either Re or stainless steel with an initial thickness of 250 μm). The pre-indentation thickness is 1/3 of the drilled hole diameter at the center which can be made by electric discharge machining (EDM), and the hole diameter is 1/2 of the culet diameter. For example, in the high pressure electrical resistivity measurement on dysprosium (Dy) in run 1 (refer to Section 4.2.1), diamond anvils with 500 μm in culet diameter were used, and the hole diameter of Re gasket was 250 μm and the pre-indentation thickness was 80 μm.

A tip on how to make the desired indentation thickness within two trials is the following. Whenever gaskets are pre-indented by using the rotating torquing tool (see Fig. 3.3(b)) in same angular degrees, the resulting indentation thickness will be the same each time as long as the same diamond anvils are used. This is because everything in the DAC assembly is in contact, and their dimensions never change during indentation process. For example, if within the several trials the indentation ended up with 70° on a polar graphing paper which is mounted on a force table and the desired indentation thickness, 80 μm, is achieved, then for the next time within two trials 70° of angular displacement with another gasket will make exactly 80 μm thickness of pre-indentation.

During the course of this research, one side pre-indented gasket was developed for DAC measurement. The one side pre-indented gasket is made by putting two gaskets on top of each other with super glue and pre-indenting the sandwiched gasket in the usual pre-indentation process, as described in Section 3.2.2. When only one side of gasket is pre-indented, the gasket

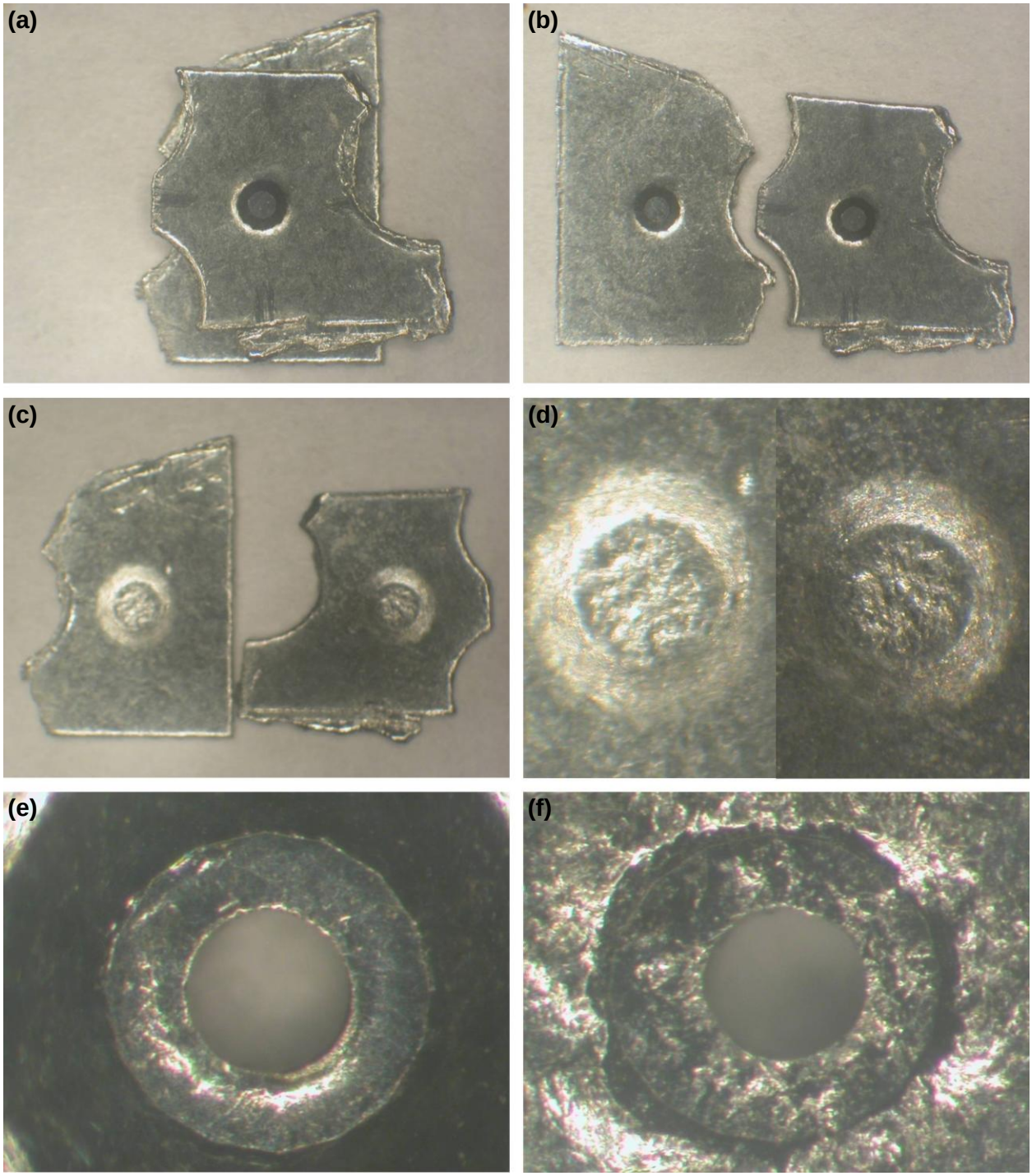

Figure 3.6: Images of the single-sided pre-indented gaskets. (a) Two gaskets (stainless steel with 250 μm of initial thickness) on top of each other (sandwiched) adhered together with superglue and then pre-indented with 0.5 mm diamond culet by the usual process, as described in Section 3.2.2. (b) One side of the two pre-indented gaskets (180 μm indentation thickness each). (c) The other side of the two gaskets which are not pre-indented (with convex surfaces at center). (d) Enlarged view of (c). (e) Pre-indented side of the one gasket after applying pressure, indicating a shallow indentation. (f) Other side of the same gasket after applying the same pressure, leaving a deeper indentation.

material close to the indentation, which is already pre-pressurized, will be more hardened than the gasket material on the other side. The benefit of this gasket is that for either the microcoil magnetic susceptibility or the liquid electrical resistivity setup (see Figs 3.8 and 3.11) the four wires (or leads) on the pre-indented side of the gasket, which come out from the pressure chamber, will not be greatly pressurized under high pressure in comparison to the other side without pre-indentation. Ideally, this will prevent the wires from being damaged (or cut) under high pressure since the non-indented side of the gasket will be mostly pressurized as seen in Fig. 3.6(e) and (f).

3.3 High Pressure Measurement DACs

A diamond anvil cell (DAC) tunes the pressure of a system to alter its physical properties. According to the physical properties, the corresponding measurement setups vary inside the DAC. Here I describe some techniques for determining properties of matter such as magnetic susceptibility and electrical resistivity under high pressure as well as moderate improvements to these techniques.

3.3.1 Susceptibility Cell

Magnetic and superconducting properties of materials can be detected in magnetic susceptibility (χ) measurements by using an induction coil system which is composed of a primary (field) coil and a secondary (pickup) coil, as seen in Fig. 3.7. Ac, rather than dc, susceptibility techniques are commonly used, including this research, due to its high sensitivity to the change in magnetization and its ability to detect magnetic and superconducting phase transitions. Positive χ indicates paramagnetic, ferromagnetic, ferrimagnetic, or antiferromagnetic

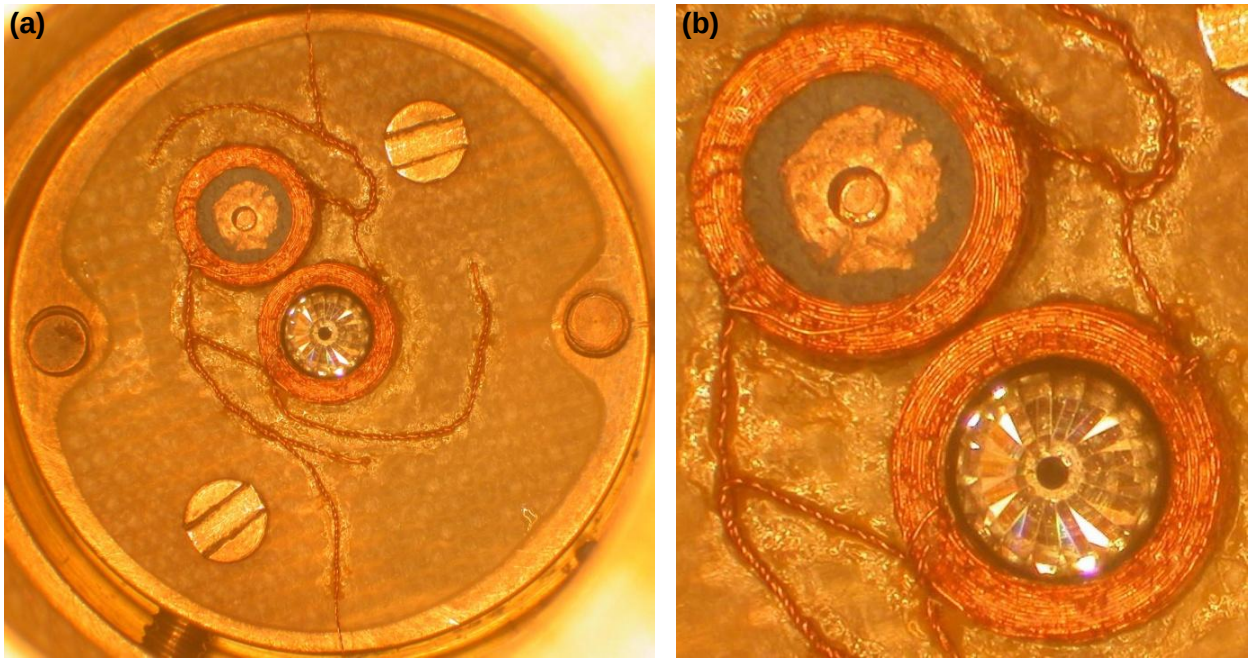

Figure 3.7: Side-by-side coil system used for high pressure ac magnetic susceptibility measurements. (a) Overview of the coil system components including the two identical coils (at the center the measurement coil and at the upper left the compensation coil), a dummy gasket (which is placed in the dummy coil with clay and is the same gasket material as the sample chamber gasket for the gasket signal compensation), MgB_2 (under the dummy gasket, not shown), a coil board (on which the coils are glued down, 0.8 mm thick), and two CuBe screws (to mount the coil system inside the body of the cell). (b) Enlarged view of the coil system. Each coil contains six inner layers of secondary and six outer layers of primary coils. The dimension of each coil is 3.46 mm in inner diameter and 1.95 mm in height. The diamond culet is 0.5 mm in diameter.

behavior, and negative χ indicates diamagnetism including superconductivity (perfect diamagnetism, $\chi = -1$ with full shielding).

Our laboratory most frequently uses the so-called side-by-side coil system (Fig. 3.7) designed by Vladimir G. Tissen to detect superconductivity (including possible strong ferromagnetism) of materials. It consists of two identical adjacent coil systems wound with 60 μm diameter of insulated copper (Cu) wires (approximately the diameter of a human hair [63]).

Each coil system consists of six layer windings on the inner side (as shown in Fig. 3.7(b)) to pick up the induced sample signals (the "secondary coil") and another six layer windings on the outer side for generating ac magnetic field (the "primary coil"), with 30 turns per layer. The two primary coils are wound in the same direction to generate the magnetic field in the same direction, whereas the two secondary coils are wound in the opposite direction to zero out the background signal.

The general principle of measuring ac magnetic susceptibility with the induction coil system is as follows. An ac driving field (external magnetic field) is applied to a sample by the surrounding primary coil with an ac current (1023 Hz, 6.8 mA for 3 Oe (3×10^{-4} T) in the case of the side-by-side coil system described above). The induced sample magnetic moment (or magnetization), depending on the nature of the magnetic properties, leads to a change in the magnetic field and thereby a change in the induced voltage in the secondary coil (which is inside the primary coil) according to the Lenz's law. For example, for a superconducting sample in the coil system, the magnetic flux is allowed to permeate the sample above the superconducting transition temperature T_c. As it is cooled down below T_c, however, the sample begins to shield the magnetic flux due to the Meissner effect and the weakened field may be detected in the reduced voltage of the secondary coil.

The magnitude of reduction in the induced voltage by a superconducting material can be estimated. This must be done before the cooling process begins in order to assist the search for superconducting signals out of the background noise. For this purpose, a small piece of magnesium diboride (MgB_2) is placed inside the dummy coil (compensating coil) to indicate the sign of the sample signal and to check the performance of the coil system. Before loading the

sample, a 1 mm piece of (ferrimagnetic) ferrite magnet can be inserted in the main coil to ensure that the superconducting signal appears as a dip (rather than a peak).

The induced voltage *S* (in the units of V) by the magnetic properties of the sample in a pickup coil, in MKS units, is

$$S = \frac{\pi f \alpha H V_s N}{R(1-D)}\chi, \tag{3.1}$$

where *f* is the frequency of the applied field in Hz, α (dimensionless) is equal to $1/\sqrt{1+(L/R)^2}$ with 2*L* being the length (or height) of the coil in m, *H* is the magnitude of the applied field in T, V_s is the volume of the sample in m^3, *N* (dimensionless) is the number of turns in the coil, *R* is the radius of the coil in m, D (dimensionless) is the demagnetization factor (which depends on the geometry of the sample and its orientation to the field), and χ (dimensionless) is the susceptibility (Eq. 3.1 modified from Ref. [1]).

For the voltage generated by a superconducting sample with full shielding ($\chi = -1$) in the side-by-side coil system, Eq. 3.1 leads to

$$S_{side-by-side}\,(\mathrm{nV}) = -\frac{8.17\times10^{-5}\times V_s(\mu\mathrm{m}^3)}{(1-D)}, \tag{3.2}$$

where the signal is in the units of nV and volume of the sample in μm^3 without considering superconducting penetration depth (λ) (Eq. 3.2 modified from Ref. [1]). For example, when a measurement utilizes 500 μm culet diamond anvils (with a gasket hole having 250 μm in diameter and 80 μm in height, the dimension of our pressure chamber), the typical sample volume (cylindrical shape, c-axis parallel to the field) especially for hydrostatic experiments

using helium (He) as a pressure medium may be $\pi \times 40^2 \times 20\ \mu m^3$ and the corresponding demagnetization factor is approximately 0.68 [64]. The estimated amplitude of a sudden drop in the temperature-dependent background signal would be 26 nV in this case. If a sample with a 25% larger radius is used ($\pi \times 50^2 \times 20\ \mu m^3$), D is 0.72 and the signal size would be 46 nV (77% increase). If a sample with a 25% greater height of the sample is used ($\pi \times 40^2 \times 25\ \mu m^3$), D is about 0.63 and the signal size would be 28 nV (only 8% increase). Thus the flattened sample may be the better choice for larger sample signals.

3.3.2 Microcoil Susceptibility Cell

The side-by-side coil system is an excellent tool to measure ac magnetic susceptibility of superconducting materials. However, the system signal-to-noise ratio can be degraded due to external noise and background noise from the metallic parts of the DACs. Various approaches have been used to enhance the sensitivity of the coil systems for ac susceptibility measurements including the approach of this thesis.

The geometry of two opposing diamonds with a metal gasket between them (~2.8 mm in diameter, see Fig. 3.5) pushes the coil system (~3.46 mm inner diameter in the side-by-side coil system, see Fig. 3.7) outside of the sample chamber into which the sub-millimeter sized sample is placed. This leads to a very low filling factor which is closely related to the signal-to-noise ratio in a coil system. Eq. 3.1 can be rewritten as

$$S \sim 2\pi^2 f H N \frac{V_s}{V_c} \chi R^2, \tag{3.3}$$

where V_c is the volume of the pickup coil and the ratio of V_s/V_c is defined as the filling factor (Eq. 3.3 modified from Ref. [65]). For example, the side-by-side coil system has a very small filling

factor of approximately 5.5×10^{-6} (in the case of a $\pi \times 40^2 \times 20$ μm^3 sample volume). One can further enhance this factor by placing the secondary (pickup) coil inside the sample chamber (the gasket hole). For this reason, a micrometer sized coil was adopted and developed by several research groups [65], inspiring us to make a microcoil 100 μm in diameter (~130 μm high with seven turns depending on the number of winding turns and extra glue thickness), which yields a filling factor of 9.8×10^{-2} (Fig. 3.8), an increase of nearly four orders of magnitude.

We now describe the construction of a microcoil 100 μm in inner diameter. An approximately 5 cm long bare tungsten (W) wire 100 μm in diameter is held down by an insulated large alligator clip adapter at each end (the alligator clip adapters are attached onto an acrylic board to prevent movement). The tungsten wire is used as a coil form around which we wind an insulated copper (Cu) wire 16 μm in diameter (Fig. 3.8(a)). In the middle of the tungsten wire, two plastic sheets (1 mm diameter cut from a square plastic weighing dish) and two stainless steel sheets (1 mm diameter, an electro-spark drilled 100 μm diameter hole at center) are inserted and glued down with thick GE varnish (a glue) to facilitate the winding process. Scotch tape is attached to the both ends of 10 mm long, 16 μm diameter Cu wire so that when the wire is carefully wound over the form, the two ends of the wire are stuck to the acrylic board to increase the tension of the wire. After making the desired number of turns, dilute GE varnish is applied to the coil and dried. The completed microcoil is shown in Fig. 3.8(b).

The estimated voltage induced by a superconducting sample in the secondary microcoil (100 μm in diameter, seven turns, 190 μm in height) and with 3×10^{-4} T of ac magnetic field (1023 Hz, 8.3 mA) from the primary microcoil (seven turns) is

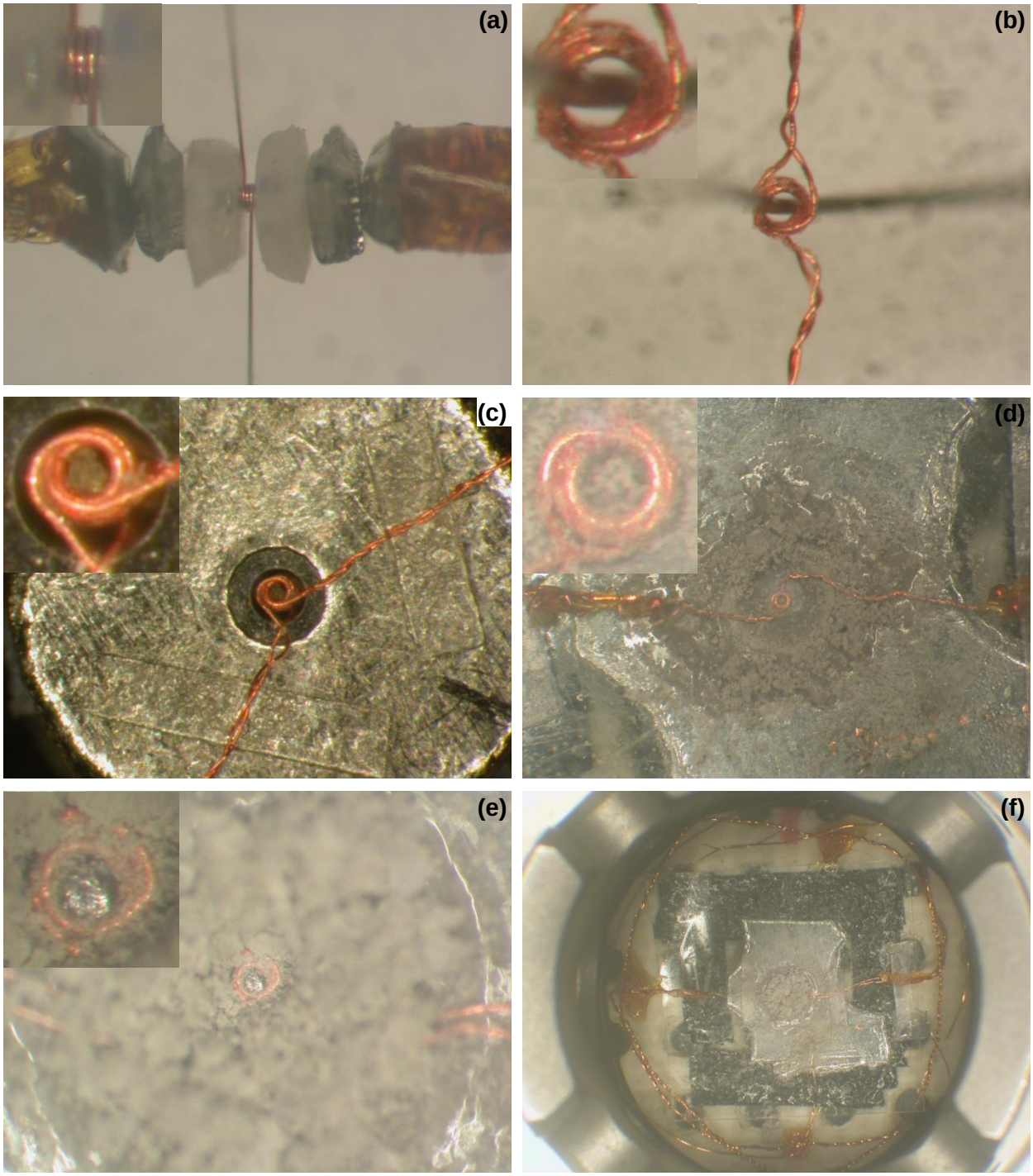

Figure 3.8: Microcoil system (100 μm inner diameter). (a) Coil form (100 μm diameter tungsten (W) wire) around which 16 μm diameter Cu wire is wound and kept between plastic sheets (white colored) and stainless steel sheets (glued on W wire). (b) Completed microcoil (inserted in 50 μm diameter W wire for picture). (c) MgB_2 in microcoil (primary and secondary, seven turns each), positioned in sample chamber (ambient pressure). (d) Microcoil on insulated (cBN-epoxy mixture), single sided pre-indented gasket (see Fig. 3.6). (e) Gd in microcoil, covered by pressure medium (cBN-epoxy mixture). (f) High pressure microcoil system mounted in DAC. All insets are enlarged views of the microcoils.

$$S_{microcoil}\ (\mathrm{nV}) = -\frac{6.29 \times 10^{-5} \times V_s(\mu\mathrm{m}^3)}{(1-D)}. \quad (3.4)$$

Comparing with $S_{side\text{-}by\text{-}side}$ which is 26 nV for a superconducting material with $\pi \times 40^2 \times 20$ μm^3, $S_{microcoil}$ is 20 nV, which is 6 nV (~23%) less despite the identical sample dimension. This arises due to the greater number of turns (180 turns) in the side-by-side system than that of the microcoil system (seven turns). With regards to the signal-to-noise ratio, however, the microcoil is superior due to its significant filling factor enhancement.

Fig. 3.9 shows ac susceptibility measurements for the comparison between the two coil systems in terms of the signal-to-noise ratio and overall (from 5 K to 290 K) temperature-dependent background signal. Magnesium diboride (MgB_2) was used as a superconducting sample (approximately $\pi \times 40^2 \times 80$ μm^3, T_c = 39 K, see Fig. 3.8(c)). The signal-to-noise ratio is 28 for the side-by-side coil system and 92 for the microcoil system. Interestingly, the background signal in the microcoil system shows little temperature dependence (see Fig. 3.9(b)), in contrast to the other coil system.

3.3.3 Resistivity Cell

In addition to the magnetic susceptibility technique, there is a transport measurement for probing the magnetism and superconductivity of materials: the electrical resistivity measurement. Electrical resistivity is a physical property that shows how resistant various materials are to the flow of electrical current, a property that is independent of the shape or size of the material. In other words, it is an intrinsic property of materials (while resistance, a related property, is proportional to the length of materials but inversely proportional to cross-sectional area).

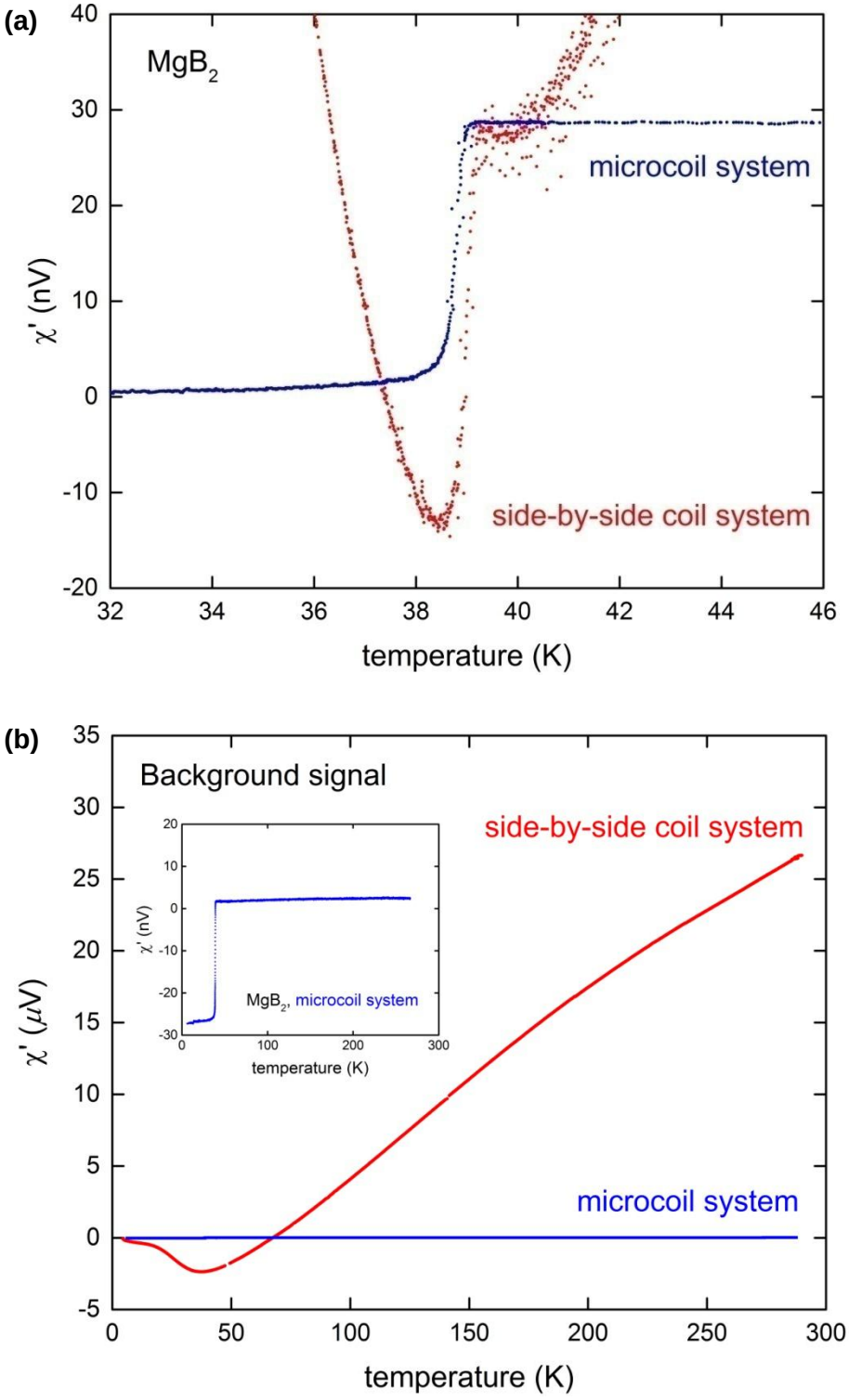

Figure 3.9: Coil system comparison (side-by-side coil system versus microcoil system). (a) Signal-to-noise comparison using the same MgB_2 sample. (b) Temperature-dependent background signal comparison.

In general, electrical resistivity measurements probe the electronic and magnetic phases of materials since resistivity is closely related to the Fermi surface geometry as well as degree and type of conduction electron scattering. Such measurement shows how individual electrons behave and the collective effects of electrons in matter. Typically, metals have low resistivity, insulators have high resistivity, and semiconductors are in the middle. For example, a good conductor, copper (Cu) exhibits 1.70×10^{-6} ohm·cm of resistivity at ambient temperature [42], while glass, which is an insulator, exhibits $10^{12} \sim 10^{16}$ ohm·cm [66]. The semiconductor, germanium (Ge) in its pure state exhibits 6.0×10^{1} ohm·cm [66]. In superconducting material, however, the resistivity drops suddenly down to exactly zero as it cools through the superconducting transition temperature T_c.

The high pressure electrical resistivity measurement technique in a DAC, developed by Shimizu *et al*. [67], was first introduced to our laboratory by T. Matsuoka from Osaka University in Japan and developed further to accommodate 180 μm central flat size of diamond culets, as seen in Fig. 3.11. For accurate resistivity sampling, the four-point configuration of leads is essential to remove any contact and lead resistance, as seen in Fig. 3.11(c).

The detailed process to construct the non-hydrostatic high pressure dc electrical resistivity setup is described here for a diamond culet of 0.18 mm diameter central flat. A rhenium (Re) gasket of approximately 7 mm diameter is pre-indented from 250 μm (initial thickness) to 30 μm thickness, as described in Section 3.2.2, and a 80 μm diameter hole is electro-spark drilled at the center of the indentation (see Fig. 3.10). The Re metal gasket on the front side is then covered overall with scotch tape for insulation, and a section of the tape is removed to expose only the indented area. An insulation layer is made on the indented area, from which the scotch tape is

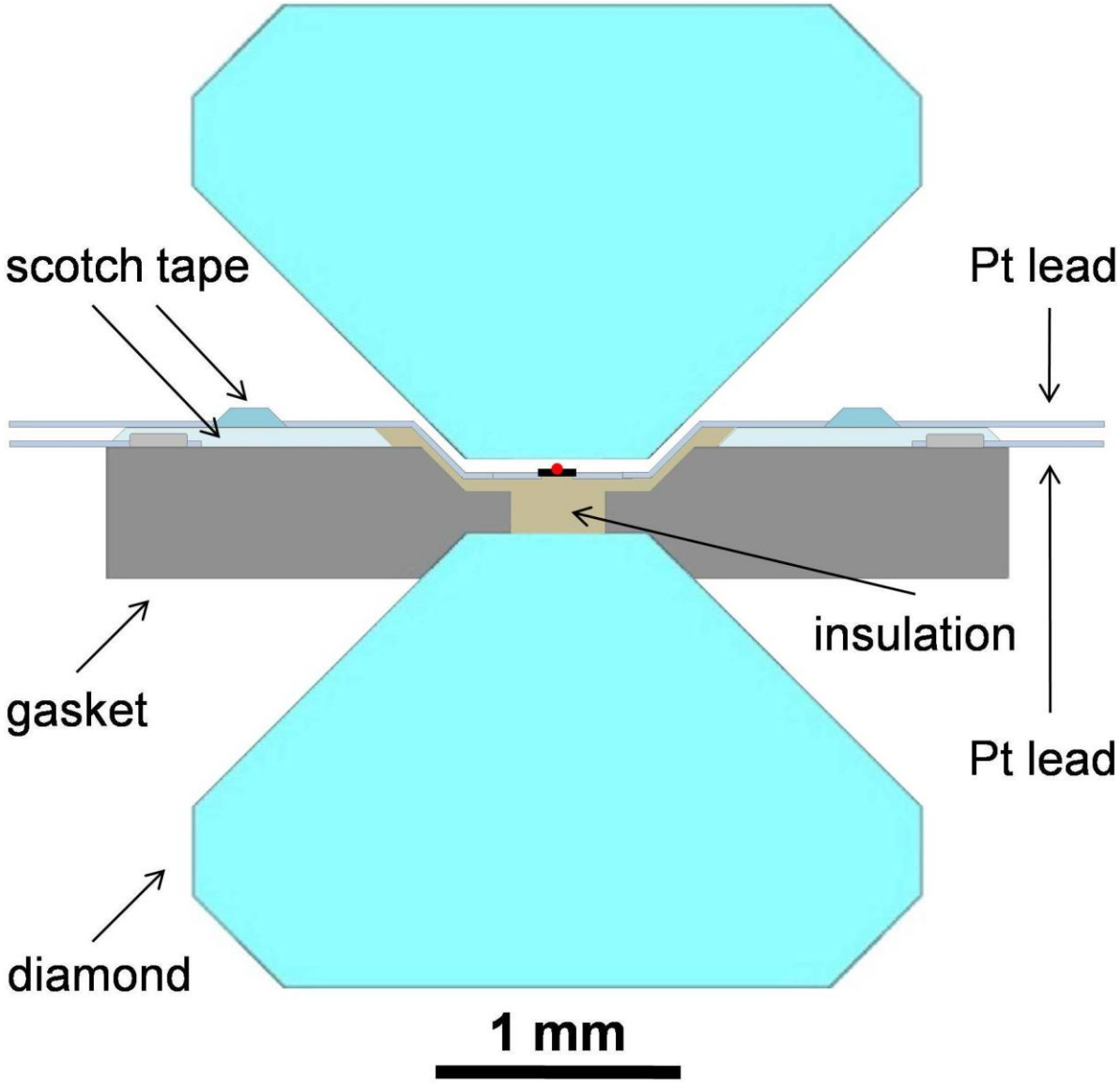

Figure 3.10: Schematic image (side view) of non-hydrostatic high pressure dc electrical resistivity technique originally developed by Shimizu *et al*. [67]. The culet of the diamond is usually less than 1 mm and gasket hole less than 0.5 mm. The sample dimension (black rectangle) is usually $\sim 30 \times 30 \times 5\ \mu m^3$ for a 0.18 mm diameter central flat culet. The red dot indicates a ruby sphere for pressure calibration. The light green area identifies the insulation made by cBN + epoxy mixture, while additional insulation is made by scotch tape on the metal (Re) gasket. Four platinum (Pt) leads, 4 μm in thickness and $\sim 80\ \mu$m long, conduct from the culet-imprinted insulation area to four longer Pt leads ($\sim$2.5 mm long) coming out of the pressure chamber.

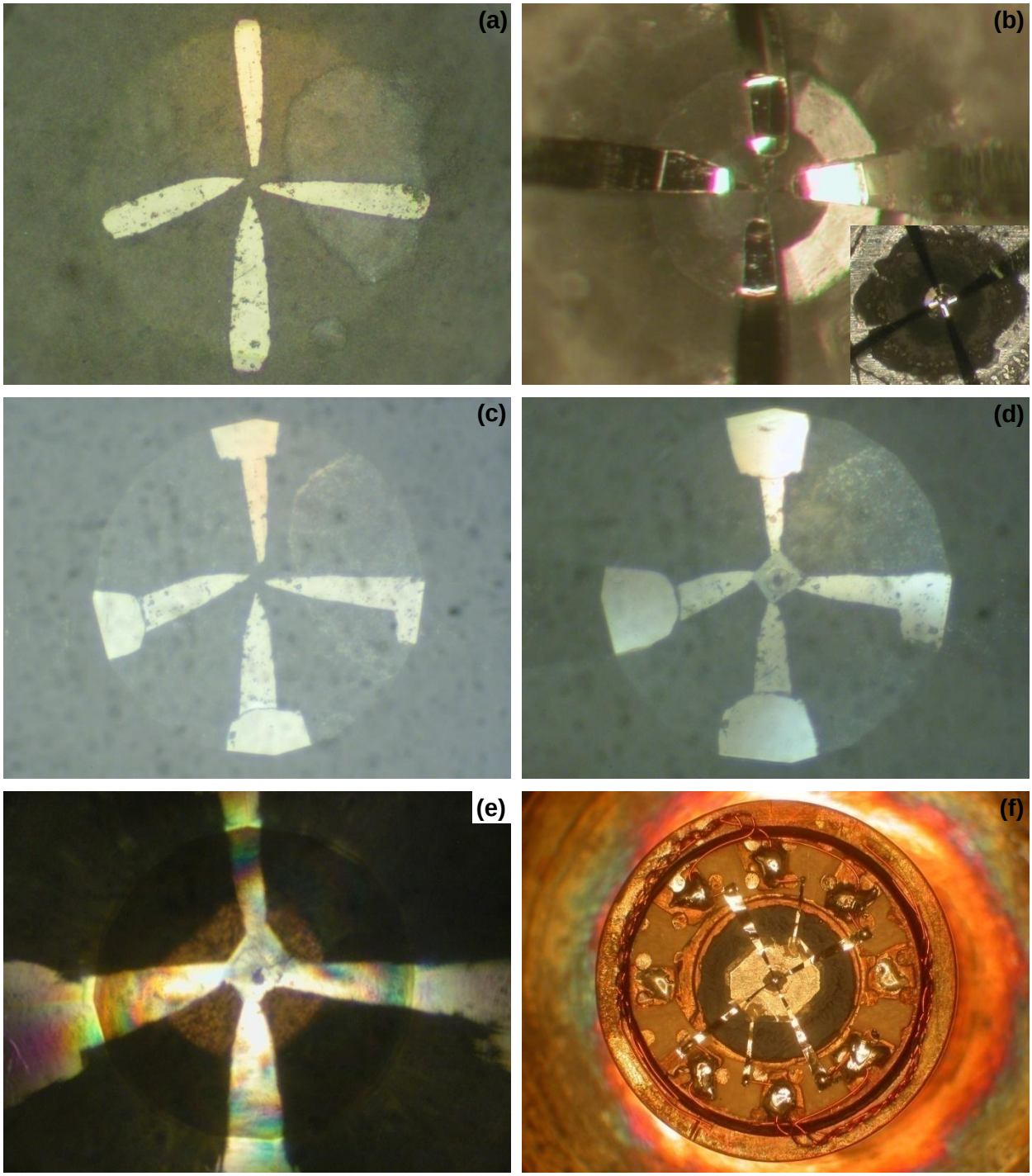

Figure 3.11: Real images (top view) of the non-hydrostatic high pressure dc electrical resistivity setup using 0.18 mm culet. (a) Four tiny Pt strips, which are positioned on the culet-imprinted insulation layer. (b) Four bridge leads making the tiny strips be connected to Cu wires out of gasket (inset shows overview of the insulation area). (c) Tiny strips and bridge leads make contact when the DAC is closed. (d) Dysprosium (Dy) sample ($20 \times 20 \times 2\ \mu m^3$) resting on four strips (two rubies are positioned one on top of the sample and the other by the sample). (e) Dy under over 1 Mbar pressure at which sample area doubles. (f) Overview of the electrical resistivity setup constructed on the piston of the DAC.

removed, by applying first the insulating powder material (a 4:1 cBN-epoxy mixture) and then closing the cell to make culet-imprinted insulation layer, as shown in Fig. 3.10 (light green area) and Fig. 3.11(b). An important point with platinum (Pt) leads is that they should be annealed beforehand with a torch (or a cigarette lighter) in order to get rid of any possible defects in the Pt material; this process will help prevent the strips from breaking under extreme pressures like 1 Mbar. Because of the difficulty in making Pt leads adhere on the insulation layer (especially on the culet-imprinted insulation area), four tiny Pt strips ($80 \times 20 \times 4\ \mu m^3$) with sharp edges are positioned first as shown in Figs 3.10 and 3.11(a). They are then connected to four much bigger and longer Pt leads (around 2.5 mm long), which serve as bridges between the tiny strips (for samples) and Cu wires (140 μm diameter) outside (to be connected to measurement devices) as seen in Figs. 3.10 and 3.11(b), (c), and (f). To reduce the pressure gradient across the sample due to the non-hydrostatic pressure medium (cBN-epoxy mixture), the dimension of the sample is adopted to be extremely small (Fig. 3.11(d) shows $20 \times 20 \times 2\ \mu m^3$ of dysprosium (Dy) sample as an example). A tiny ruby sphere (around 15 μm diameter) is then placed by (or on top of) the sample for sample pressure calibration. In order to check the possible contact between the metal gasket and the Pt leads under extreme pressures, two additional Pt leads are connected to the both ends of gasket, as seen in Figs 3.10 and 3.11(f). The metal gasket resistance and any possible connection between gasket and sample are measured after each application of pressure on the sample.

3.3.4 Liquid Resistivity Cell

Although the non-hydrostatic high pressure electrical resistivity technique still provides valuable information about how the electronic and magnetic phases of matter change under

pressure, the inhomogeneity and anisotropy of the applied pressure often complicate the interpretation of the resulting data. During this Ph.D. research, possible hydrostatic high pressure dc electrical resistivity measurements (the so-called liquid resistivity cell) were carried out by using methanol-ethanol mixture as a hydrostatic pressure medium, inspired by and with the aid of R. Jaramillo *et al.* [68], as shown in Fig. 3.12.

The process to prepare a liquid resistivity setup is described here (for example, using 500 μm diameter culet diamonds). A 300 μm thick stainless steel gasket sheet is pre-indented to 50 μm in thickness, and a 260 μm diameter hole is then electro-spark drilled through the center of the metal gasket. Acetone is used to dissolve a large amount of Al_2O_3 powder into a small amount of epoxy. The Al_2O_3-epoxy solution is drop cast on the pre-indented area of the metal gasket using a syringe and the drop cast composite gasket (metal + ceramic epoxy) is cured using UV light.

Pre-indentation is repeated with the composite gasket making the hole in the metal gasket to reach 330 μm in diameter. An approximately 240 μm diameter hole (sample space) is then drilled through the ceramic insulation mechanically from both sides of the gasket with a tiny 200 μm diameter drill in order to produce a clean hole, as seen in Fig. 3.12(b). Four gold (Au) wires (20 μm in diameter) are spot-welded onto the lead (Pb) sample ($80 \times 80 \times 30$ μm^3) and the sample is carefully positioned in the sample chamber, as seen in Fig. 3.12(c). A 4:1 methanol:ethanol pressure medium is slowly introduced in the sample chamber with a syringe to reduce the chance of trapping any bubble within the chamber. The DAC is then closed within a minute to avoid the complete evaporation of the alcohol pressure medium. With around 1 GPa of pressure, the pressure medium in the sample chamber is sealed.

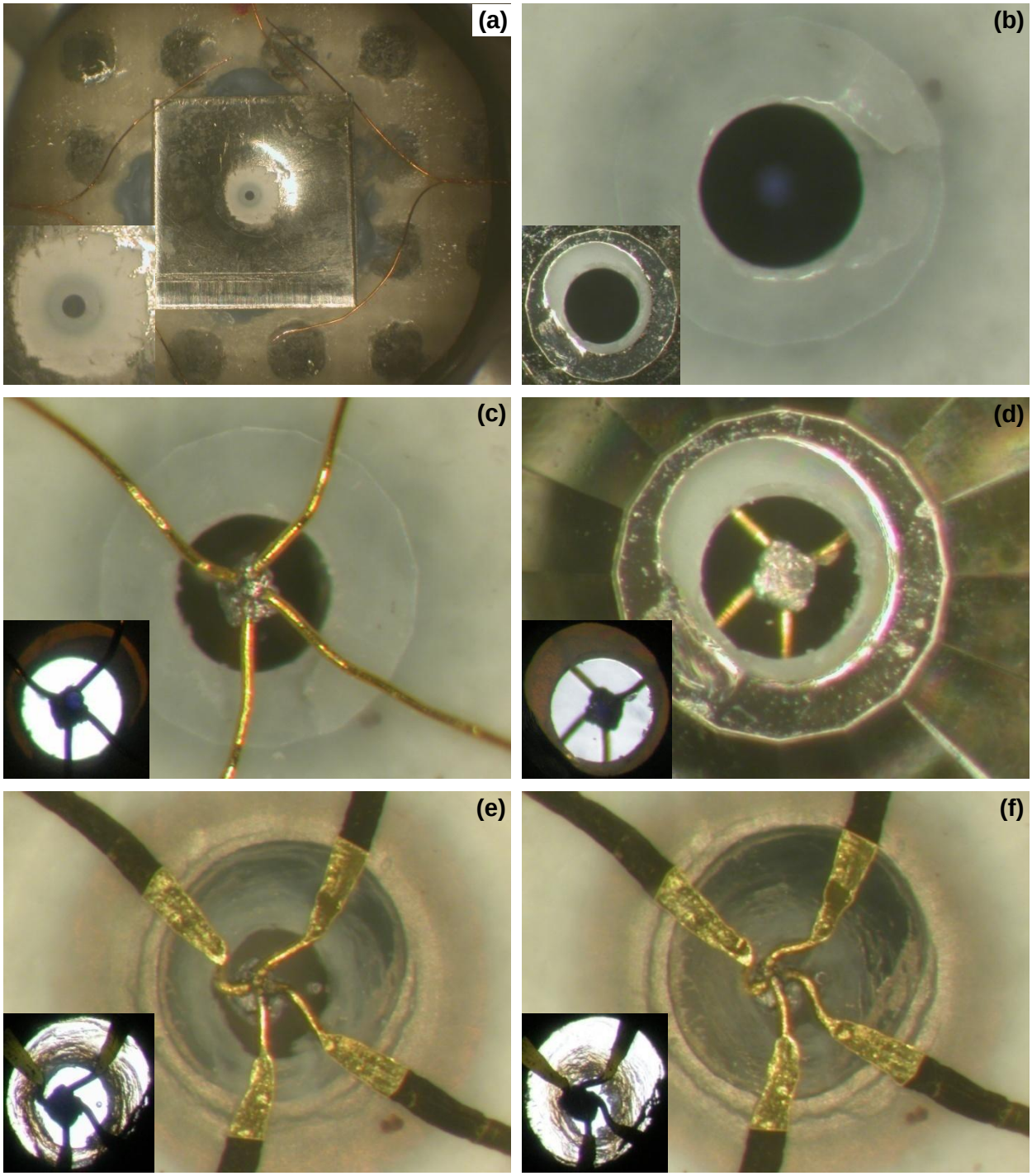

Figure 3.12: Hydrostatic high pressure dc electrical resistivity setup. (a) Pre-indented and insulated (with Al_2O_3-epoxy mixture) stainless steel gasket in DAC. Inset shows enlarged view of insulation area. (b) Ceramic gasket with a hole (about 240 μm diameter). Inset shows the opposite side view of the gasket. (c) Lead (Pb) sample spot-welded with gold wire and positioned in sample chamber at ambient pressure. (d) Opposite side view of the sample chamber. (e) Pb under about 2 GPa (a ruby sphere at the right side of the sample). (f) Pb under around 4 GPa. Insets from (c) to (f) are enlarged views of the sample using a transmitted light.

3.4 Manometer

The accurate determination of the pressure to which a sample is subjected in the DAC motivated much effort in the early stage of the high pressure science field to develop several pressure calibration techniques such as laser-induced fluorescence, internal diffraction standards (for example, using the well-known equation of state of NaCl), Raman spectrum of diamond, and so on. During the course of this dissertation research, ruby fluorescence and diamond vibron were used to calibrate the sample pressures. Both these techniques are described below.

3.4.1 Ruby Fluorescence

The common method for determining sample pressure used in DACs involves use of a tiny luminescent ruby crystal (3000 to 5500 ppm Cr^{3+} doped α-Al_2O_3 [69]) of ~ 10 to 20 μm diameter. Two rubies are positioned one along with a sample and the other outside the sample chamber as a reference. In our laboratory, the doped Cr^{3+} ions of ruby crystal are excited using an argon-ion laser (green, 514 nm line) for pressures up to ~ 80 GPa and an diode laser (blue, 445 nm line) for higher pressures.

The mechanism of ruby fluorescence is as follows. A green or blue laser excites core electrons of the Cr^{3+} ion from a ground state to a broad absorption band *U* (centered at around 18,200 cm^{-1}) or *Y* (centered at around 24,800 cm^{-1}), as seen in Fig. 3.13. These excited electrons quickly decay into metastable ^2E levels without radiation (called "phonon-assisted relaxation") and continuously decay into the ground state causing ruby fluorescence of R_1 and R_2 lines as shown in Fig. 3.13. The spectrum of the fluorescence radiation from a ruby at ambient condition exhibits sharp peaks at 694.25 nm (14,404 cm^{-1}, R_1 line) and 692.86 nm (14,433 cm^{-1}, R_2 line)

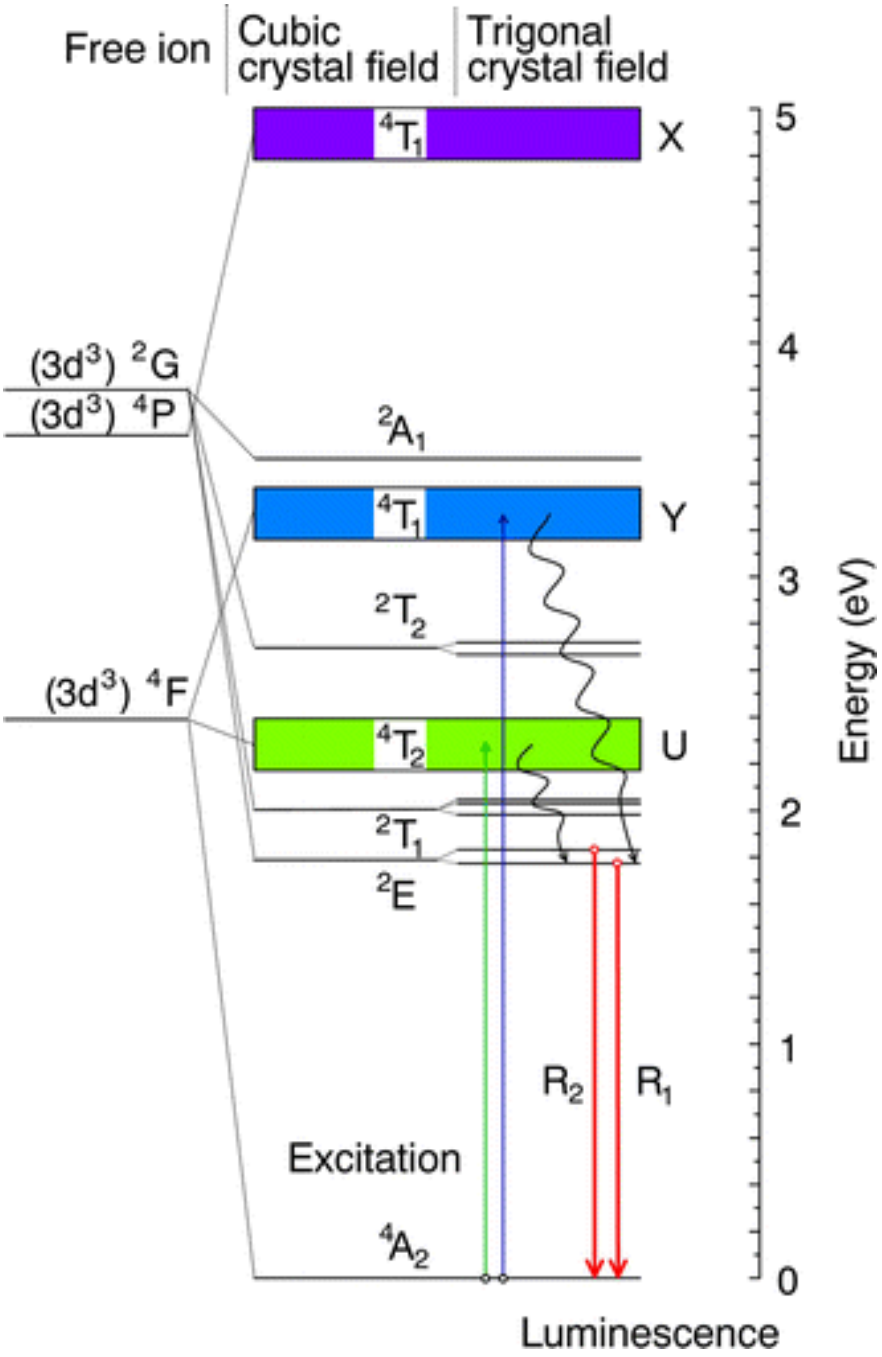

Figure 3.13: Energy level diagram of the Cr^{3+} ion in ruby. Optical absorption (by a green or blue laser) into the *U* or *Y* broad band leads the population in the metastable ^2E states through non-radiative decay and thereby leads to the R_1 and R_2 ruby fluorescence (luminescence) by radiative decay. Figure taken from Ref. [70].

and they shift monotonically with pressure.

Under pressure the ^2E levels are lowered, and R_1 and R_2 lines exhibit the red-shift [70]. The wavelength shift of the R_1 line by applying pressure is used to determine the sample pressure. Throughout this research, a pressure calibration using ruby fluorescence to 150 GPa by Chijioke *et al*. [71], which considers various results of quasi-hydrostatic pressure environments, was used in the form

$$P(\text{GPa}) = \frac{1876}{10.71}\left[\left(\frac{\lambda}{\lambda_0}\right)^{10.71} - 1\right], \tag{3.5}$$

where λ and λ_0 are the wavelength of the R_1 line at high and ambient pressures respectively.

The R_1 and R_2 line intensities, which are related to the population of two ^2E levels, are governed by the Boltzmann distribution $\exp(-\Delta E/k_B T)$. At room temperature both intensities are comparable since the difference ΔR_{12} = 42 K (29 cm^{-1} or 3.6 meV) is much smaller than 300 K (~ 25 meV, 202 cm^{-1}). At low temperature, however, the lower ^2E level is more populated leading decrease in R_2 line intensity, and also the wavelengths of R_1 and R_2 lines shift to slightly lower values as temperature decreases (the temperature dependence of R_1 line can be found in Refs [72,73]).

It is known that a non-hydrostatic pressure condition makes not only each ruby fluorescence line (R_1 and R_2 lines) broaden but also the separation between them increase [74]. Under extreme pressures, the intensity of the ruby signal significantly decreases as the absorption bands *U* and *Y* shift to higher energy causing the less efficiency of optical pumping by a green or blue laser. Due to this limitation, a diamond Raman vibron technique is used to determine pressures above 1 Mbar.

3.4.2 Diamond Vibron

An alternate method for determining pressure due to the difficulties in the ruby fluorescence technique at extreme pressures is to measure the first-order Raman spectrum of diamond vibron. This calibration technique has several advantages in that it needs no use of any pressure calibrating materials to place in the sample chamber. It reduces the error range of sample pressure in non-hydrostatic pressure conditions (which can cause a pressure marker to be away from the sample) because it simply measures the pressure of culet surface of diamond at which the sample is positioned.

Raman spectroscopy uses the inelastic scattering of photons (for example, a laser). It observes the vibrational and rotational modes of a system and is used to detect phase and structural transitions. Raman scattering occurs when an incident light (photon) of frequency v interacts with a material (phonon) and excites their energy states leading a small fraction of inelastically scattered photons of different frequency $v' = v \pm v_{vib}$ (v_{vib} indicates the vibrational frequency of the system), which is the so-called Raman effect (see Fig. 3.14). Most incident photons, however, scatter elastically with the same frequency v. This is called Rayleigh scattering. The Raman scattering is classified into two types, the Stokes line with a photon of $v - v_{vib}$ (slightly lower energy) and the anti-Stokes line with a photon of $v + v_{vib}$ (slightly higher energy).

The vibrational mode of diamond (diamond vibron) is measured in the first-order Raman scattering. At ambient pressure, a single peak occurs in the Raman spectrum (Stokes line) of diamond and the Raman edge (peak) frequency locates at v_0 = 1334 cm^{-1} in the Raman shift (frequency difference between incident and scattered photons). Under pressure the vibrational

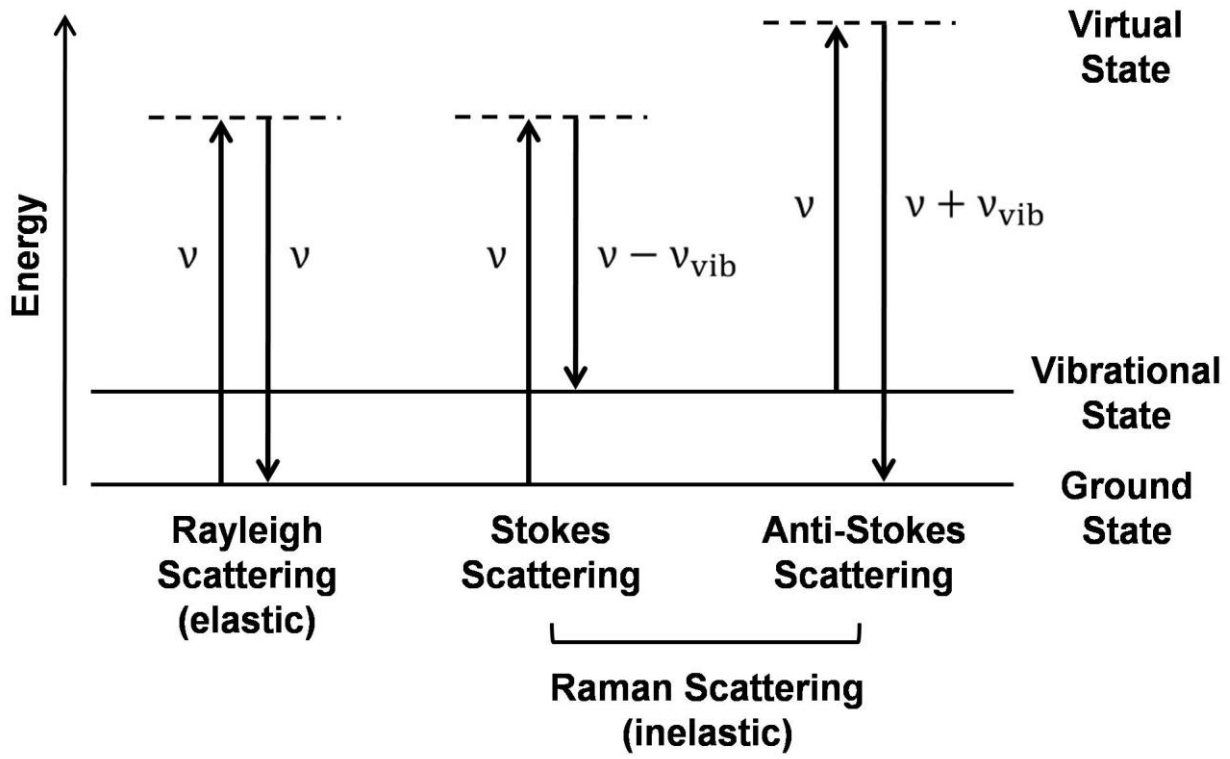

Figure 3.14: Energy level diagram of the Raman scattering (inelastic) in comparison with Rayleigh scattering (elastic). Most incident photons with frequency *v* scatter back elastically at the same frequency *v*. A small fraction (around 0.1 ppm), however, scatters inelastically with frequency $v - v_{vib}$ or $v + v_{vib}$. The dashed lines refer to the virtual states.

energy levels of diamond shift and the peak position increases. Since most parts of diamond are at ambient pressure except for the culet area, the peak from ambient pressure dominates over the peak from higher pressure, making the Raman spectrum broad. The highest Raman edge frequency yields the sample pressure.

The recent pressure calibration using the high frequency edge of the Raman spectrum of diamond vibron to 310 GPa is done by Akahama *et al.* [75] and was used throughout this research in the form

$$P(\mathrm{GPa}) \cong K_0 \frac{\Delta\nu}{\nu_0}\left[1 + \frac{1}{2}(K_0' - 1)\frac{\Delta\nu}{\nu_0}\right], \tag{3.6}$$

where ν_0 = 1334 cm^{-1}, K_0 = 547(11) GPa, K_0' = 3.75(20), and $\Delta\nu = \nu - \nu_0$. The diamond vibron measurement in our laboratory uses an Ar-ion laser (green, 514 nm, 19460 cm^{-1}) along with a QE65000 spectrometer (Ocean Optics) which measures spectra from 515 nm to 615 nm wavelength. This range corresponds from 40 cm^{-1} to 3190 cm^{-1} in Raman shift.

Chapter 4

Results and Discussion

Of the elemental metals in the periodic table, lanthanides have many unique properties which are closely related to their strongly localized 4*f* electrons (or highly correlated electron behaviors). One might expect that at sufficiently high pressure the lanthanides may undergo dramatic changes as the degree of localization of their 4*f* orbitals decreases and may become unstable. For example, most of the lanthanides suffer the so-called volume collapse (in the molar volume) at a critical pressure P_{vc} and the origin is still a matter of intense debate. Recent high pressure electrical resistivity measurements on the heavy lanthanides dysprosium (Dy), gadolinium (Gd), and terbium (Tb), and their dilute doping into the superconducting host yttrium (Y), show anomalous behaviors in the pressure dependence of both the magnetic ordering temperature T_o and the superconducting transition temperature T_c, respectively. These results provide insights into possible Kondo physics involvement in the selected heavy lanthanides under extreme pressure.

4.1 Previous Studies

One of the most fascinating phenomena the lanthanide metals exhibit is their volume

collapse (VC) at a critical pressure P_{vc}, usually accompanied by a structural transition from high to low symmetry [76]. Delocalization of the 5*f* electrons (local-to-band transition) is widely accepted as an explanation for the appearance of low-symmetry structures for the actinides lighter than americium (Am). The question is whether the VC in the lanthanides is also actually driven by a local-to-band transition in the 4*f* electron state. Another outstanding property of the lanthanides is their magnetic ordering, known to result from the so-called Ruderman-Kittel-Kasuya-Yosida (RKKY) indirect exchange interaction between the localized 4*f* magnetic moment and the surrounding conduction electrons. Within the RKKY interaction the magnetic ordering temperature T_o follows standard de Gennes scaling at ambient pressure. Another question is how the T_o evolves as a function of pressure to extreme compression, in particular at P_{vc}.

4.1.1 Pressure-Induced Volume Collapse

Most lanthanide metals suffer a sudden drop in their molar volume at a critical pressure P_{vc}, the largest being 16% in cerium (Ce) at only 0.7 GPa [35,77–79], praseodymium (Pr) 9.1% at 21 GPa [80], europium (Eu) 3% at 12 GPa [81,82], gadolinium (Gd) 5% at 59 GPa [83,84], terbium (Tb) 5% at 53 GPa [85], dysprosium (Dy) 6% at 73 GPa [86], holmium (Ho) 3% at 103 GPa [87], thulium (Tm) 1.5% at 120 GPa [88], and lutetium (Lu) 5% at 90 GPa [89], accompanied by a structural transition to a lower symmetry (except Ce's isostructural transition).

Three models involving 4*f* interactions have been proposed to describe the pressure-induced volume collapse phenomena in the lanthanides at P_{vc} [90]: first, the *valence transition model* where a 4*f* electron jumps into the *spd*-electron conduction band, enhancing the crystalline binding and leaving a sudden reduction in the ionic radius [91]; second, the *Mott-Hubbard model*

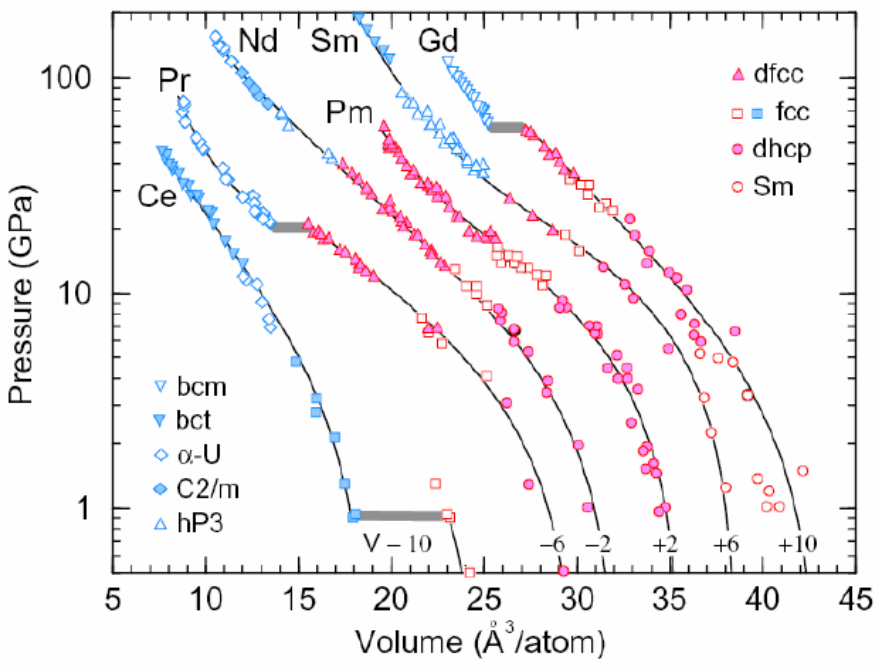

Figure 4.1: Equation of state at room temperature for the early lanthanide metals showing volume collapse under pressure in Ce, Pr, and Gd, accompanied by structural transitions form high to low symmetry. Red (blue) symbols identify high (low) symmetry structures. Figure taken from Ref. [76].

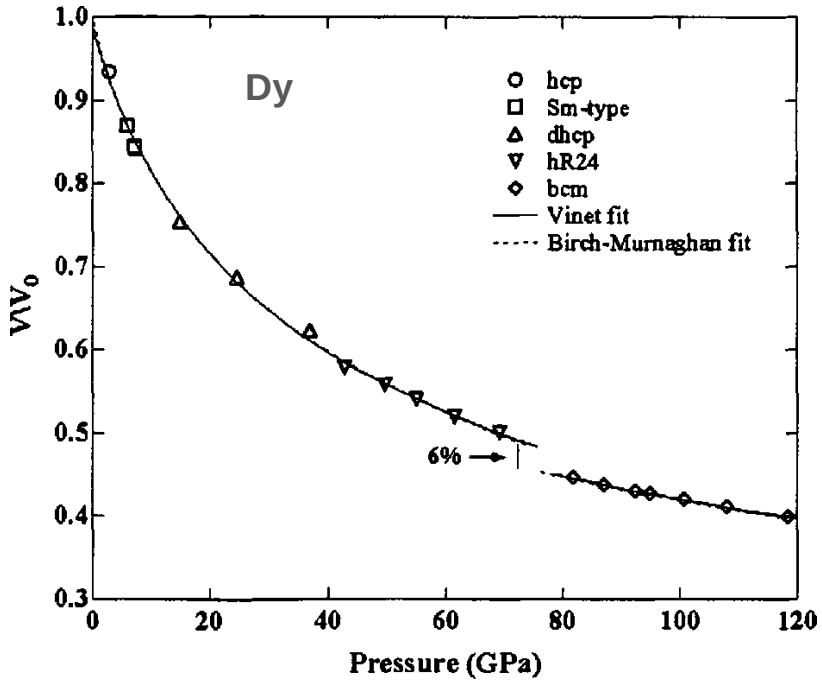

Figure 4.2: Equation of state at room temperature for Dy showing 6% volume collapse at 73 GPa. Notice that hR24 (hexagonal) structure is the distorted fcc (dfcc) phase. Figure modified from Ref. [86].

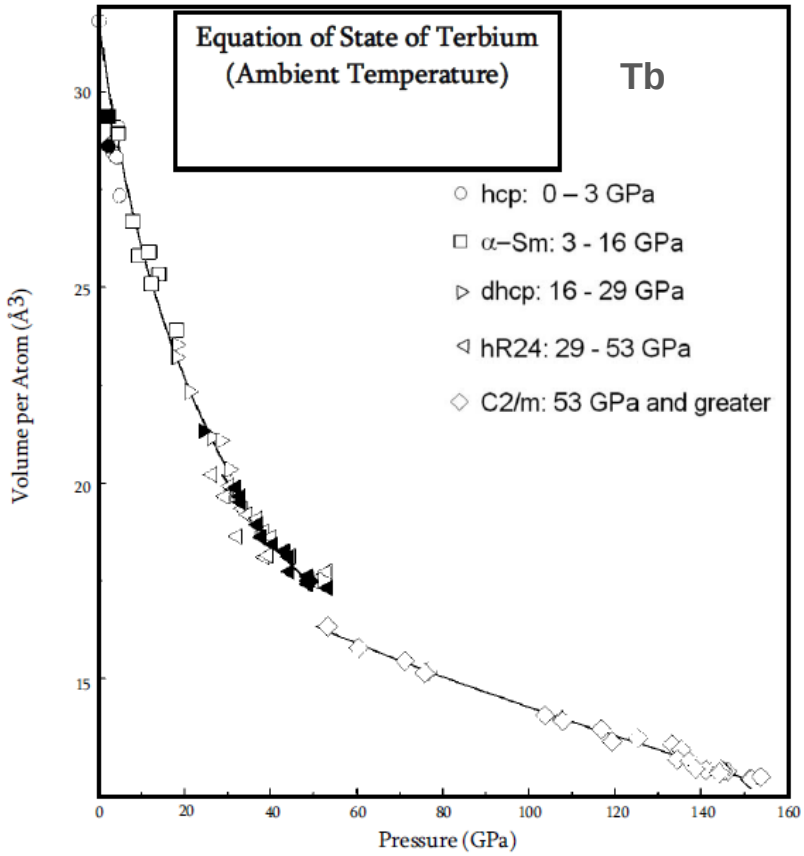

Figure 4.3: Equation of state at room temperature for Tb showing 5% volume collapse at 53 GPa. Notice that body centered monoclinic (bcm) phase is a monoclinic fcm (C2/m) structure. Figure modified from Ref. [85].

(local-to-itinerant transition) where the 4*f* electrons no longer remain localized but become itinerant and make a significant contribution to the crystalline binding [92]; third, the *Kondo volume collapse model* where the approach of the 4*f* state to the Fermi energy during compression (hybridization between 4*f* electrons and conduction electrons) leads to an increase in the Kondo temperature T_K and thereby the Kondo binding energy kT_K, and this additional binding reduces the sample volume and further enhances T_K and kT_K, finally leading to the so-called Kondo volume collapse [93]. In addition, there is a fourth model where 4*f*-electron

involvement is not necessary to cause a volume collapse. In the *s* → *d charge transfer model*, the increase in the number of *d* electrons in the conduction band under pressure leads a structural phase transition accompanied by a volume collapse [90].

4.1.2 Magnetic Ordering under High Pressure

At ambient pressure heavy lanthanide elements, such as gadolinium (Gd), terbium (Tb), and dysprosium (Dy), exhibit magnetic ordering at low temperatures. Gd metal is trivalent with hcp structure, a half-filled $4f^{7}$ electron configuration, and ferromagnetic below 293 K at ambient pressure [5,6]. Tb has the same number of valence electrons as Gd with hcp structure at ambient pressure, a partially filled $4f^{8}$ electron configuration, antiferromagnetic below 229 K, and ferromagnetic below 221 K [5,6]. Dy is also a trivalent heavy lanthanide having hcp structure at ambient pressure with a partially filled $4f^{9}$ electron configuration, antiferromagnetic below 174 K, and ferromagnetic below 90 K [5,6] as seen through the resistance curve in Fig. 4.4. Electrical resistivity measurements can provide valuable information about not only the behavior of single electron but also collective electromagnetic effects such as ferromagnetism or antiferromagnetism for magnetic materials. In Fig. 4.4 the temperature-dependent resistance curve shows the magnetic ordering temperature T_o, which is identified by a distinct slope change (or kink) in the resistance curve.

Because of the highly localized 4*f*-electron orbitals, heavy lanthanide metals stand out among other elemental metals by the strong local moment magnetism. One can estimate that in order to delocalize the 4*f* orbitals (a local-to-itinerant transition), it might be necessary to compress them by approximately fivefold in the molar volume, where the nearest 4*f*-electron wave functions possibly overlap each other [24]. This, in turn, would lead to 4*f* band formation

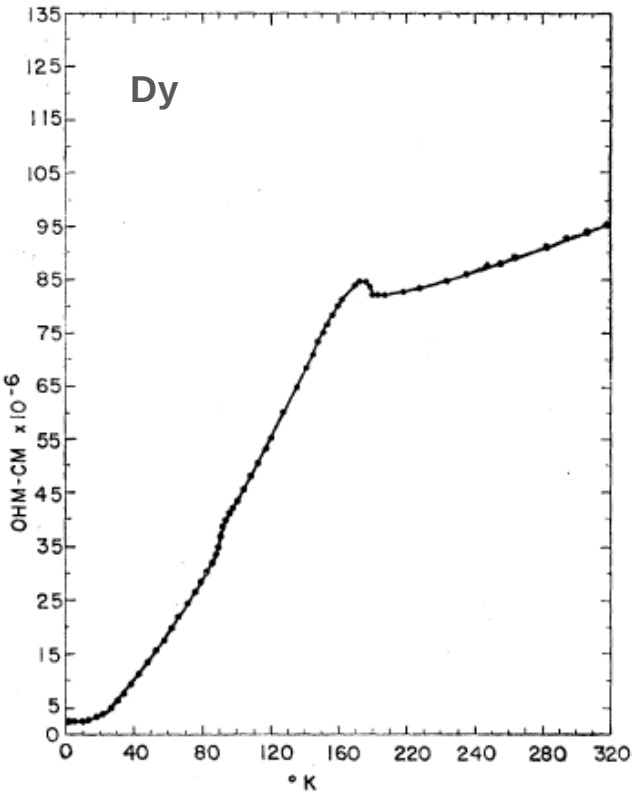

Figure 4.4: Electrical resistivity of Dy versus temperature between 1.3 K to 320 K at ambient pressure. Notice that a kink at 90 K is associated with ferromagnetism below 90 K and a kink at 174 K is associated with antiferromagnetism from 90 K to 174 K. Above 174 K it is a paramagnetic regime. Figure modified from Ref. [6].

and a loss of magnetism by the further band broadening at high pressures. Except for these heavy lanthanides, other types of magnetism (for example, 3*d* band magnetism of chromium (Cr), manganese (Mn), iron (Fe), cobalt (Co), and nickel (Ni)) may require relatively less pressure to lead to a loss of magnetism (or at least to magnetic instabilities).

Jackon *et al*. [29] recently carried out ac magnetic susceptibility measurements on the heavy lanthanides gadolinium (Gd), terbium (Tb), dysprosium (Dy), holmium (Ho), erbium (Er), and thulium (Tr) under high pressure to around 10 GPa. They reported that the magnetic ordering

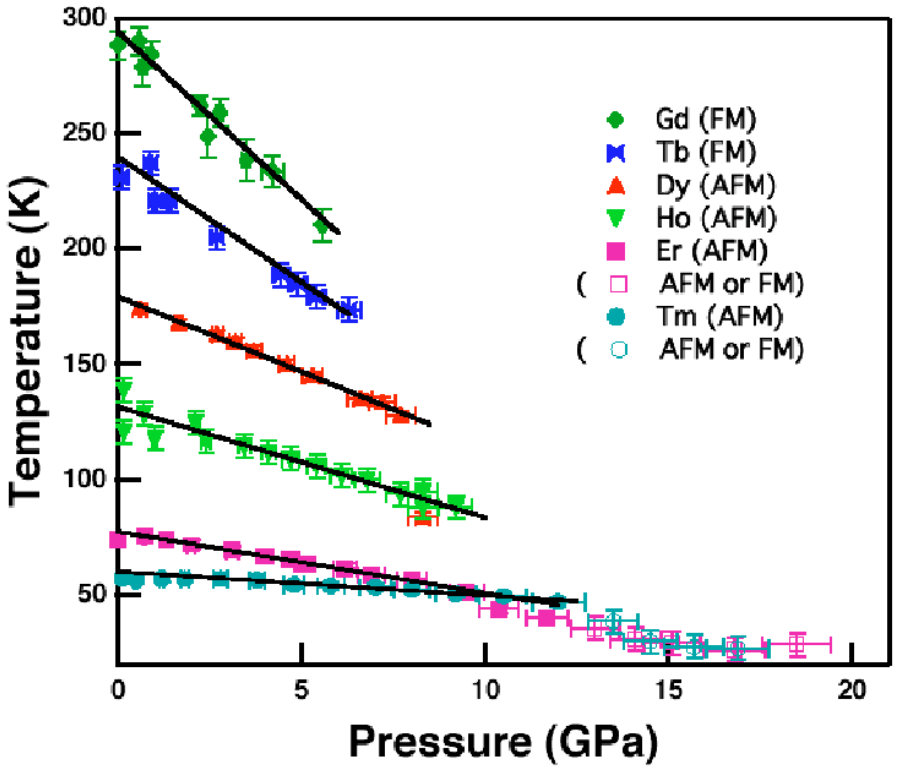

Figure 4.5: Magnetic ordering temperatures of the heavy lanthanides as functions of pressure. FM (AFM) refers to ferromagnetic (antiferromagnetic) transition temperature. The solid straight lines are a guide to the eye. Figure taken from Ref. [29].

temperature T_o, such as ferromagnetic transition temperature T_C (Curie temperature) or antiferromagnetic transition temperature T_N (Néel temperature), of the heavy lanthanides tends to decrease monotonically with increasing pressure (as seen in Fig. 4.5) retaining conventional (or stable) magnetic ordering behavior scaled by de Gennes factor $(g_J - 1)^2 J_t(J_t+1)$, where g_J is the Landé g-factor and J_t is the total angular momentum of the heavy lanthanide ions as determined according to the Hund's rules (see Table 4.1).

4.1.3 Volume Collapse and Magnetic Instability

More than 60 years ago, a large isostructural (fcc) volume collapse under pressure was

Table 4.1 Landé *g*-factor and de Gennes factor for lanthanide ions according to the Hund's rules, as given by table in Ref. [94].

Ion	Shell	S	L	J_t	g_J	$(g_J-1)^2J_t(J_t+1)$	Ion	Shell	S	L	J_t	g_J	$(g_J-1)^2J_t(J_t+1)$
La^{3+}	$4f^0$	0	0	0	–	–	Gd^{3+}	$4f^7$	$\frac{7}{2}$	0	$\frac{7}{2}$	2	15.75
Ce^{3+}	$4f^1$	$\frac{1}{2}$	3	$\frac{5}{2}$	$\frac{6}{7}$	0.18	Tb^{3+}	$4f^8$	3	3	6	$\frac{3}{2}$	10.50
Pr^{3+}	$4f^2$	1	5	4	$\frac{4}{5}$	0.80	Dy^{3+}	$4f^9$	$\frac{5}{2}$	5	$\frac{15}{2}$	$\frac{4}{3}$	7.08
Nd^{3+}	$4f^3$	$\frac{3}{2}$	6	$\frac{9}{2}$	$\frac{72}{99}$	1.84	Ho^{3+}	$4f^{10}$	2	6	8	$\frac{5}{4}$	4.50
Pm^{3+}	$4f^4$	2	6	4	$\frac{3}{5}$	3.20	Er^{3+}	$4f^{11}$	$\frac{3}{2}$	6	$\frac{15}{2}$	$\frac{6}{5}$	2.55
Sm^{3+}	$4f^5$	$\frac{5}{2}$	5	$\frac{5}{2}$	$\frac{2}{7}$	4.46	Tm^{3+}	$4f^{12}$	1	5	6	$\frac{7}{6}$	1.17
Eu^{3+}	$4f^6$	3	3	0	–	–	Yb^{3+}	$4f^{13}$	$\frac{1}{2}$	3	$\frac{7}{2}$	$\frac{8}{7}$	0.32
							Lu^{3+}	$4f^{14}$	0	0	0	–	–

discovered in cerium (Ce) [77,78] with the volume contraction of 16% at 0.7 GPa, as seen in Fig 4.6(a), which is the largest volume contraction and the lowest pressure of any lanthanide with volume collapse phenomena. The sudden and large decrease in the dc magnetic susceptibility (magnetic-nonmagnetic transition or γ-α transition) of Ce across the volume collapse pressure P_{vc} at 0.7 GPa [95] indicates that the 4*f* local moments play an important role in this mechanism, as seen in Fig. 4.6(b). The electronic properties of Ce were recently investigated by spectroscopic measurements such as x-ray absorption near-edge structure (XANES) [96], resonant inelastic x-ray scattering (RIXS) [96], and non-resonant x-ray emission spectroscopy (XES) [97]. All the results strongly support the Kondo volume collapse model for Ce at P_{vc}.

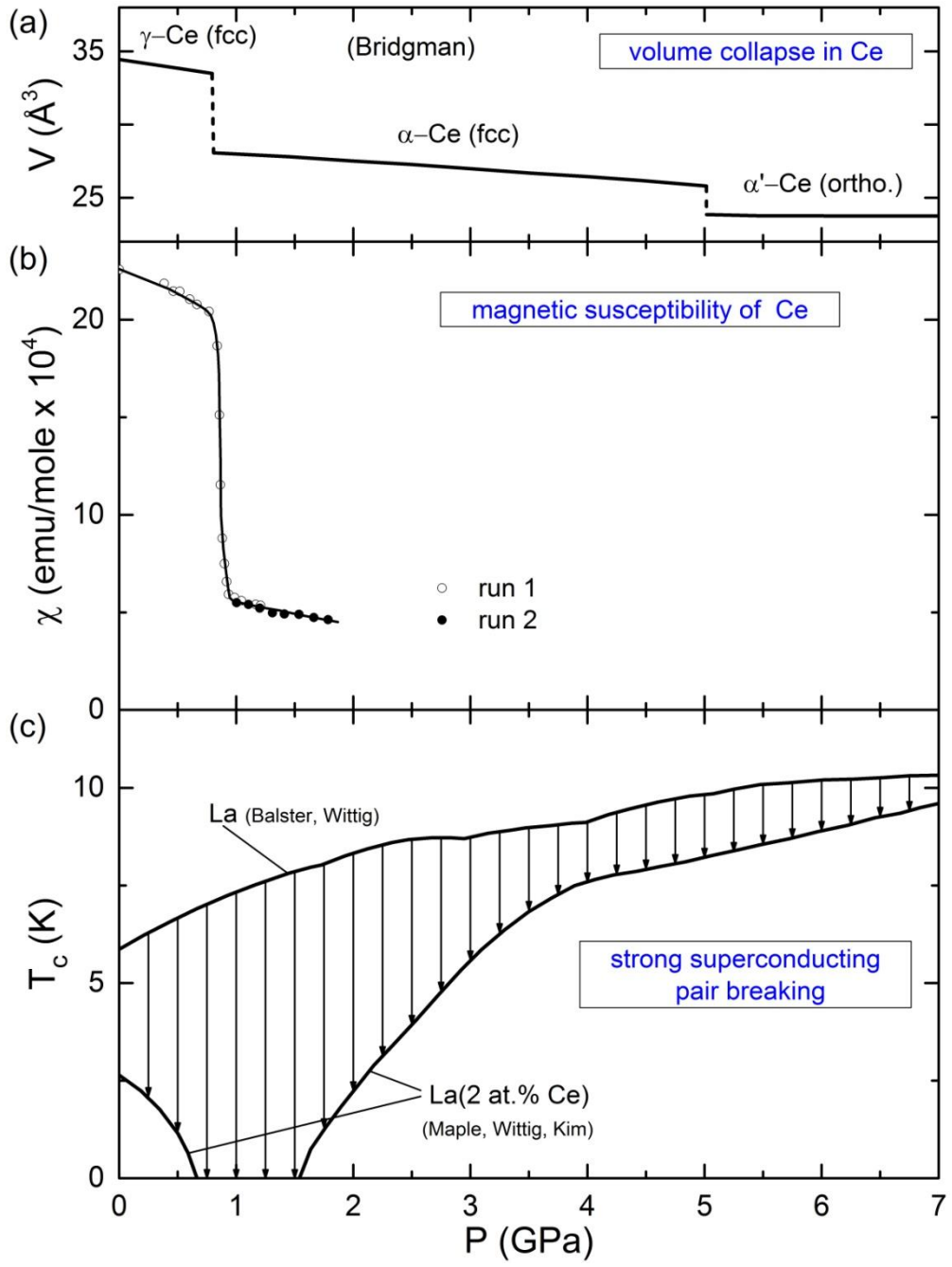

Figure 4.6: Volume collapse and magnetic instability of Ce. (a) Isostructural (fcc) γ-α transition of Ce with 16% volume collapse at 0.7 GPa. (b) Pressure dependence of the magnetic susceptibility of Ce at room temperature showing strong decrease across the volume collapse pressure P_{vc} at 0.7 GPa. (c) Superconducting transition temperature versus pressure for dilute concentration 2% of the magnetic Ce impurity in the superconducting La host compared to that of pure La. Notice La(2% at. Ce) shows a dramatic "sinkhole-like" suppression at around 0.7 GPa, which is a signature (hallmark) of giant Kondo pair-breaking. Figures taken from Refs. [34,35,95].

In more than 20 years since the discovery of the isostructural volume collapse in Ce, M. B. Maple *et al.* [34] reported interesting experimental results that the superconducting transition temperature T_c in the superconducting lanthanum (La) host was strongly suppressed by the dilute Ce ions across the pressure where the pure Ce's volume collapse occurs (around 0.7 GPa) as seen in Fig. 4.6(c). Their strategy was to employ superconductivity as a sensitive probe for the magnetic character of the impurity in the dilute alloys containing a superconducting host [98]. In other words, the degree of pair breaking in the superconductivity (reflected in the suppression of superconducting transition temperature) by the dilute magnetic impurity under pressure can tell about the pressure-induced magnetic properties of the impurity metal itself. They suggested that the strong pair breaking resulted from a significantly increased antiferromagnetic coupling between conduction electrons and magnetic impurity spins (which is known as pair breaking by the Kondo effect or Kondo pair breaking) with increasing pressure and thus strongly supports the Kondo volume collapse model for Ce at 0.7 GPa.

The next element to Ce in the lanthanide series is praseodymium (Pr), which also undergoes a 10% volume collapse at 21 GPa [80]. XANES [99] and XES [100] studies confirm that neither the valence nor the bare 4*f* local magnetic moment changes in Pr for pressures across the volume collapse transition at 21 GPa. In addition, recent resonant x-ray emission spectroscopy (RXES) measurements suggest the presence of 4*f*-conduction electron hybridization over the collapse region [101]. The dilute magnetic alloy La(Pr), as found in La(Ce), also showed a strong suppression of T_c at a pressure close to 21 GPa [102] but a full recovery of $T_c(P)$ was not seen due to the maximum pressure limit at 27 GPa. The recent analogous measurements on Y(Pr) by G. Fabbris *et al*. [103] clearly show the characteristic Kondo-sinkhole suppression in the dilute

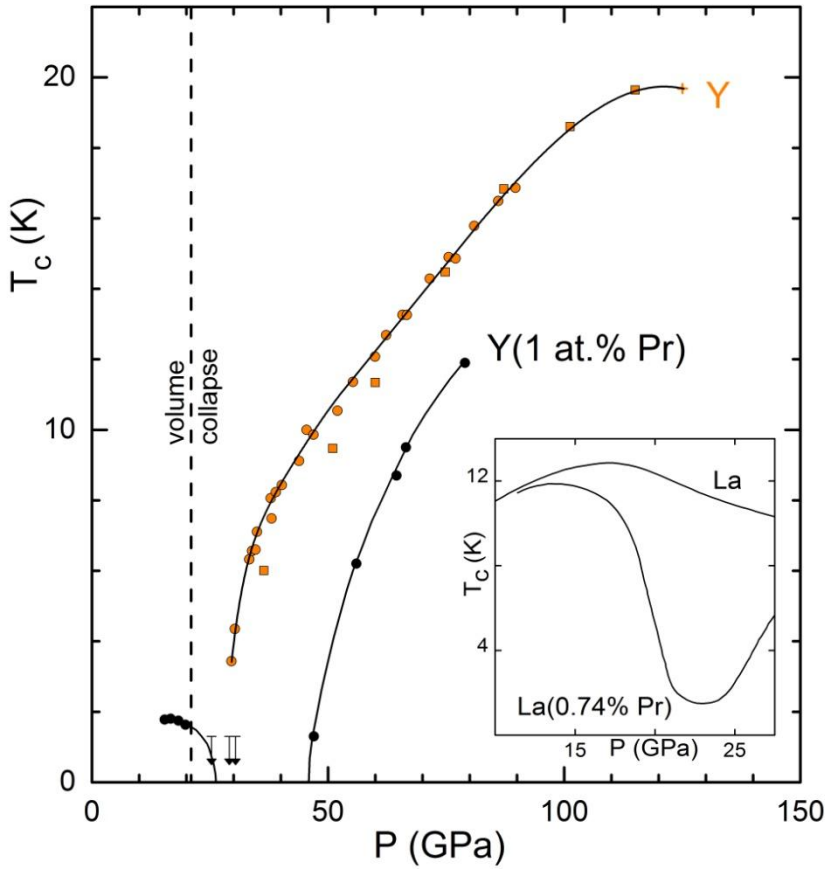

Figure 4.7: Superconducting transition temperature T_c versus pressure for 1% concentration of the Pr impurity in the superconducting Y host compared that of pure Y. Vertical dashed line refers to the critical pressure for the volume collapse in Pr. Inset shows data for La and La(Pr) alloy adapted from Ref. [102]. Notice Y(1 at.% Pr) sample shows a dramatic "sinkhole-like" suppression in T_c. Figure modified from Ref. [103].

magnetic alloy as seen in Fig. 4.7. Thus, all these results support the Kondo volume collapse model for Pr at 21 GPa.

It would be very interesting, as was the motivation for this dissertation research, to see how the pressure-induced magnetic instability affects the magnetic ordering temperature T_o for heavy lanthanides such as Gd, Tb, and Dy under extreme pressure to over 1 Mbar, especially in conjunction with their pressure-induced volume collapse phenomena.

4.2 Experimental Results and Analysis

The research contained within this dissertation focuses on the non-hydrostatic high pressure dc electrical resistivity measurements on the heavy lanthanides, dysprosium (Dy), gadolinium (Gd), terbium (Tb) as well as their alloys containing a superconducting host, yttrium (Y). These studies were in conjunction with several high pressure synchrotron spectroscopic measurements such as x-ray absorption near edge structure (XANES), x-ray emission spectroscopy (XES), x-ray fluorescence (XRF), and x-ray absorption fine structure (XAFS) measurements performed by G. Fabbris *et al.* [103] at the Advanced Photon Source (APS), Argonne National Laboratory (ANL). All these studies utilized diamond anvil cells (DACs) with type Ia diamond anvils of 180 μm to 500 μm diameter culet (or central flat of culet, see Section 3.2.1 regarding performing the fine culet surface alignments) and generating pressures on the samples to mostly around or over 100 GPa (1 Mbar, one million higher than the atmospheric pressure). Rhenium (Re) gaskets, unless otherwise stated, were used with the pre-indented thickness and hole diameter according to the description in Section 3.2.2. Pressure was calibrated and determined using either the ruby fluorescence or diamond vibron (see Sections 3.4.1 and 3.4.2) at the desired temperatures. The temperature range was from the ambient temperature (room temperature, around 295 K) cooling down to temperatures as low as about 1.3 K. The non-hydrostatic high pressure electrical resistivity techniques, described in Section 3.3.3, were used to detect the magnetic ordering temperatures T_o as well as superconducting the transition temperatures T_c under extreme pressures.

4.2.1 Dysprosium

Three separate electrical resistivity measurements on elemental dysprosium (Dy) metal were

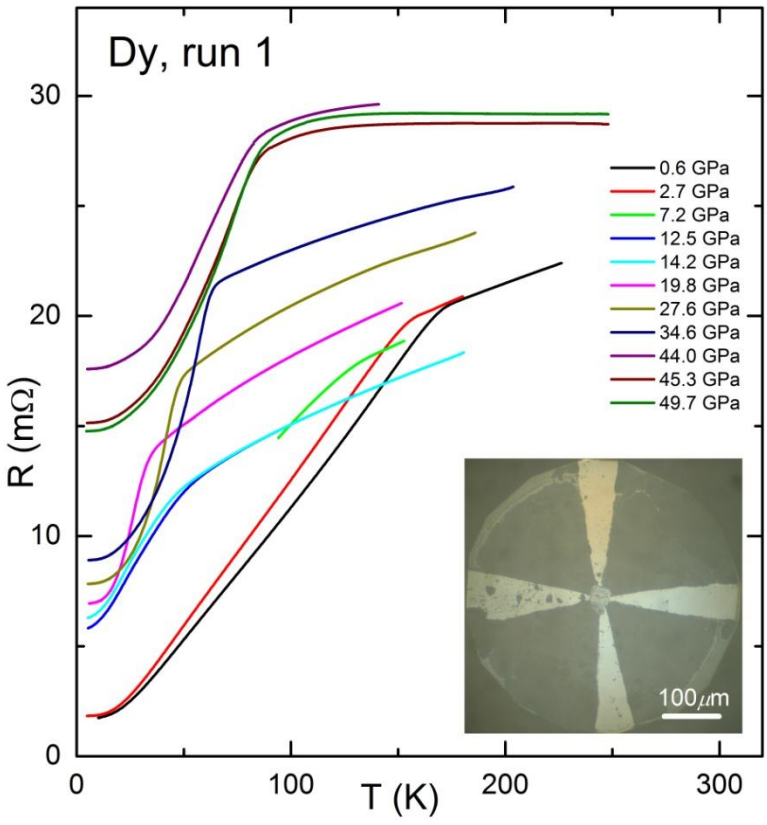

Figure 4.8: Resistance of Dy from run 1 versus temperature in pressure range from 1 to 50 GPa. The magnetic ordering transition is identified by the distinct slope change (kink) in the resistance with increasing temperature (warming). Inset shows photograph of Dy sample ($30 \times 30 \times 5$ μm^3) and 500 μm diameter culet of diamond. Figure modified from Ref. [104].

carried out under high pressure. Fig. 4.8 shows the electrical resistance $R(T)$ versus temperature (warming) at 11 different increasing pressures to 50 GPa from run 1 with the estimated pressure accuracy of $\pm$10%. In Fig. 4.9 the same type of data from run 2 is plotted at 12 different pressures to approximately 108 GPa. Notice that in this run 2 above 63 GPa, the values of pressure are estimated from the pressure in the He-gas driven membrane (in the units of bar), which pushes the piston into the body of cell (also called double-diaphragm, see Fig. 3.3(a)). In Fig. 4.10 the electrical resistance versus temperature (warming) from run 3 is shown at 14 different pressures with the estimated pressure accuracy of $\pm$10%. All three runs show the

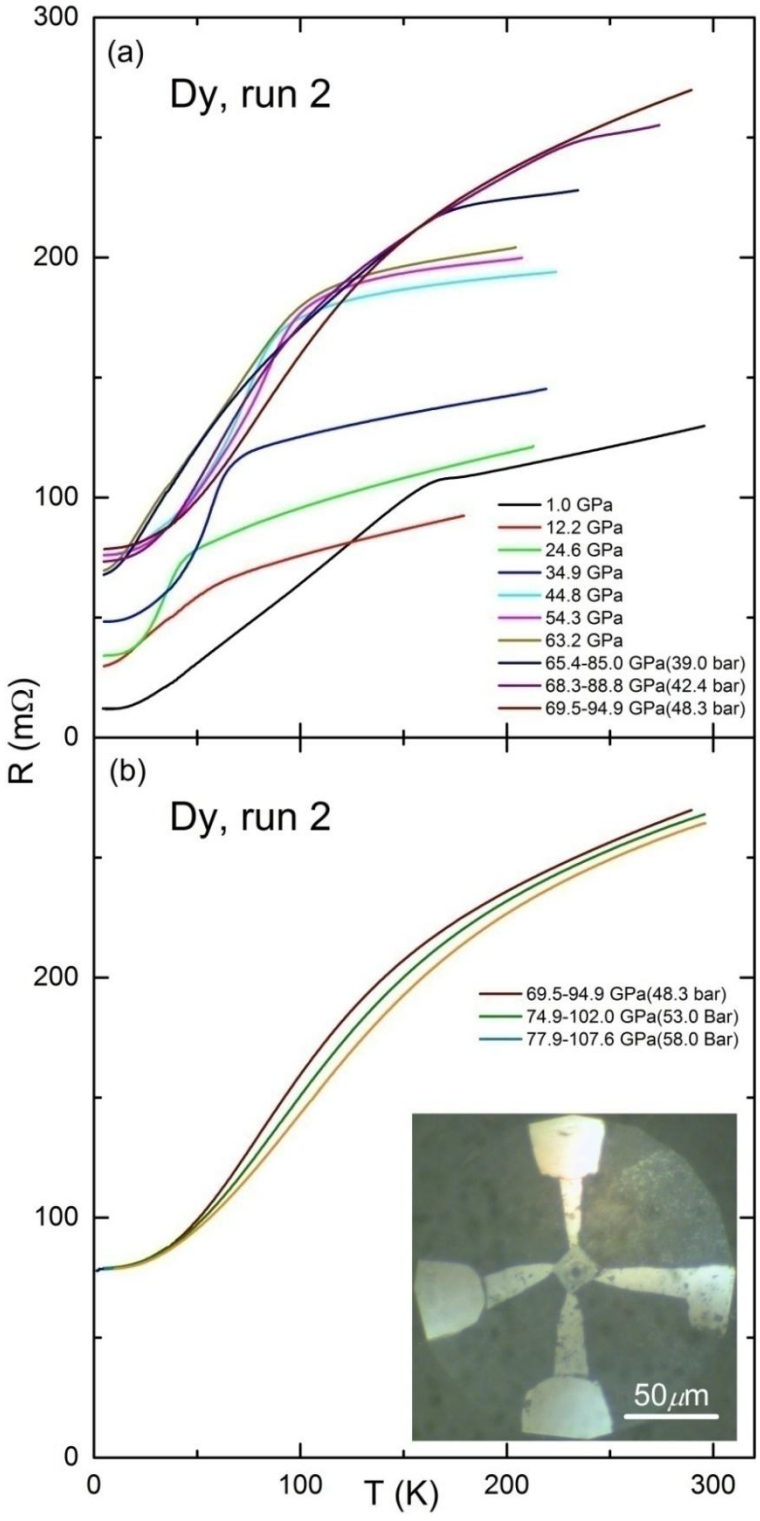

Figure 4.9: Resistance of Dy from run 2 versus temperature (warming) in pressure range: (a) 1–95 GPa, and (b) 95–108 GPa. The kink in the resistance with increasing temperature remarks T_o. Inset shows image of Dy sample ($20 \times 20 \times 2\ \mu m^3$) and 180 μm diameter central flat of diamond culet. Figure modified from Ref. [104].

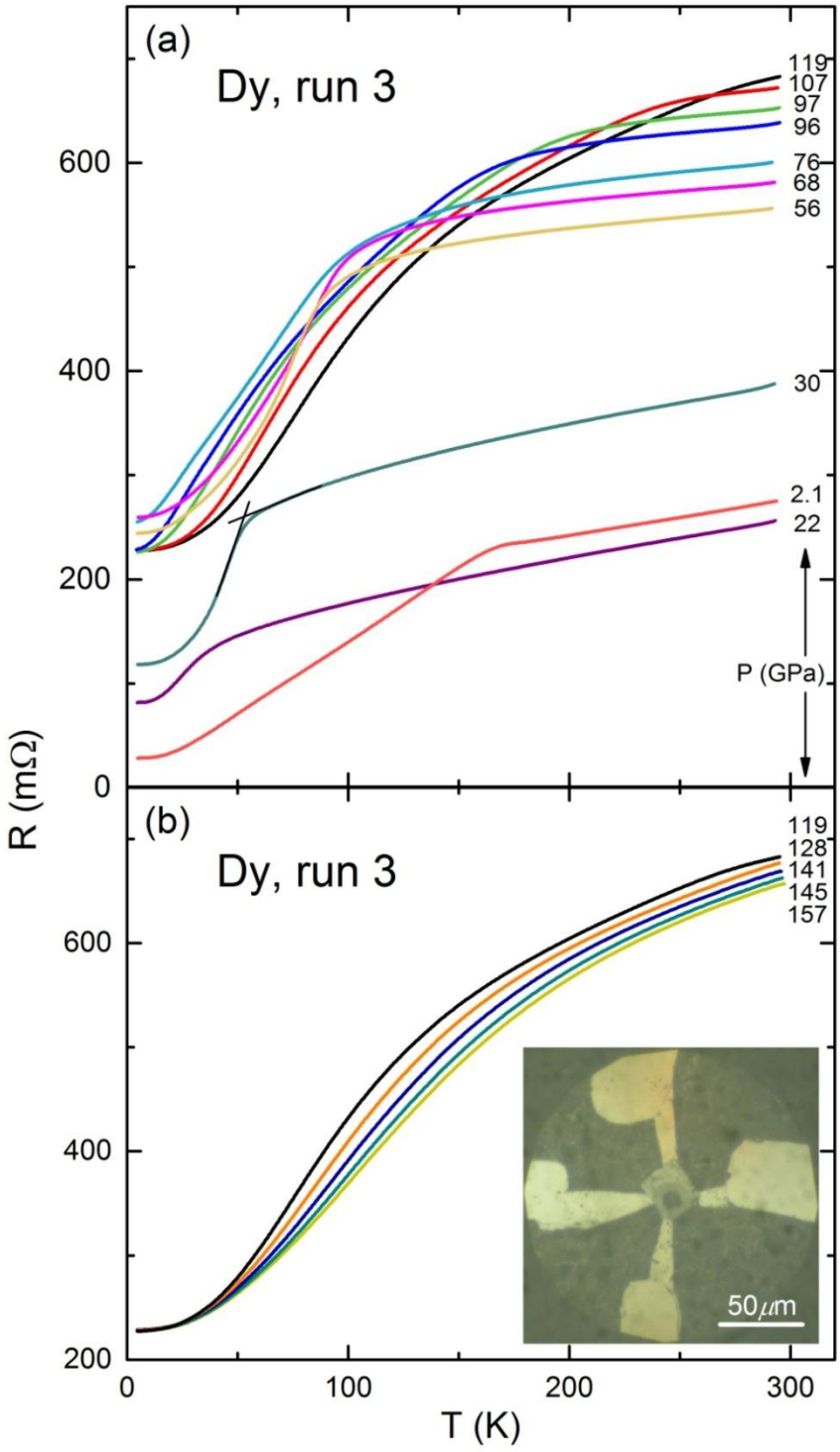

Figure 4.10: Resistance of Dy from run 3 versus temperature (warming) to 295 K in pressure range: (a) 2.1–119 GPa and (b) 119–157 GPa with the estimated pressure accuracy of $\pm$10%. The magnetic ordering is identified by the distinct slope change (kink) in the temperature-dependent resistance curve, as illustrated in (a) at 30 GPa. Inset shows image of Dy sample ($30 \times 30 \times 5\ \mu m^3$) and 180 μm diameter central flat of diamond culet. Figure modified from Ref. [104].

distinct slope change (kink) in the resistance with increase in temperature revealing the magnetic ordering transition as long as it is present below 295 K the highest available temperature of the measurements. Notice that Figs. 4.8–4.10 are raw data plots without any further analysis.

In Fig. 4.10 the residual resistance R_d (due to the defect scattering) at around 5 K increases initially since applying pressure generates more defects into the sample through the non-hydrostatic pressure condition of the measurement. For pressures higher than 56 GPa, however, the cell appears to stabilize as evidenced by almost constant R_d values. This trend of the defect scattering applies to all three measurements as seen in Figs. 4.8 and 4.9.

Resistivity measurements are able to reveal the magnetic properties of matter since the behavior of conduction electrons is very sensitive to their magnetic environment. The magnetic ordering transition (antiferromagnetic ordering for dysprosium at least until 7.4 GPa [29]) is clearly seen by the distinct kink in the temperature-dependent resistance curve near 170 K at 2.1 GPa (the lowest pressure in run 3) in Fig. 4.10. The increase in the slope of the resistance curve upon cooling represents the suppression of spin-disorder scattering resistance R_{sd} due to the influence of magnetic ordering environment from Dy^{3+} ions in the system [105]. At higher pressures the kink broadens and takes on a knee shape because of the presence of pressure gradients across the sample, but still the characteristic magnetic transition remains visible until 107 GPa. The magnetic ordering temperature T_o is defined by the intersection point of two straight (black) lines above and below the knee, as illustrated for the data at 30 GPa in Fig. 4.10(a).

Fig. 4.11 shows selection of resistance versus temperature curves for Dy from run 3 in Fig. 4.10 where they are shifted vertically for clarity. The red lines in the figure refer to the suggested

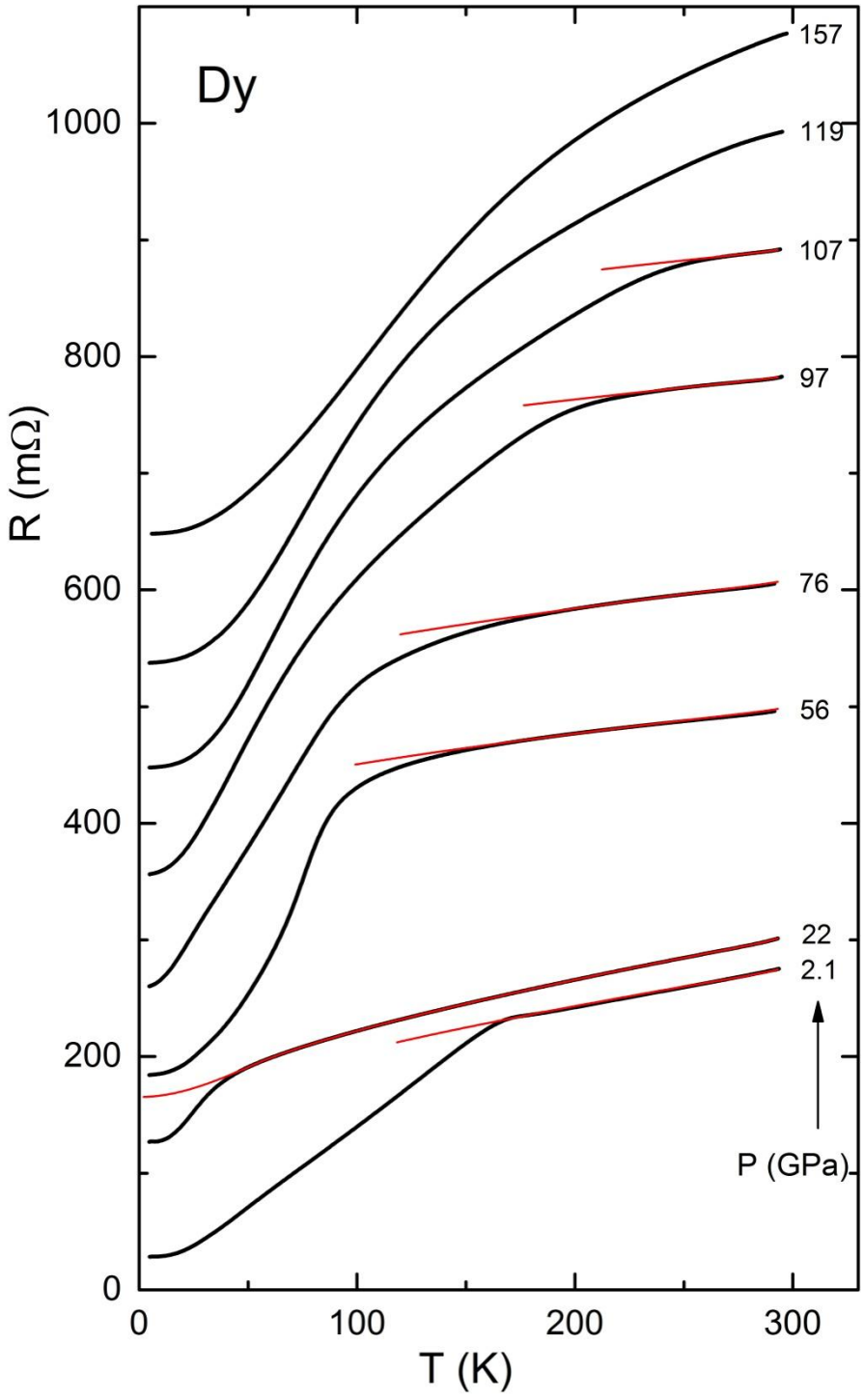

Figure 4.11: Selection of temperature-dependent resistance curves for Dy from run 3 in Fig. 4.10. Notice that the curves have been shifted vertically for clarity, except for 2.1 GPa. Red lines with small positive slope give temperature-dependent phonon resistance curves for $T \gtrsim T_o$. R(T) at 22 GPa is used as a canonical phonon resistance curve, which is extended to 0 K.

phonon resistance $R_{ph}(T)$ for each pressure by utilizing $R(T)$ at 22 GPa (which has the lowest T_o value) as the canonical phonon resistance curve (extended to 0 K) and adjusting its slope to match with the other $R(T)$ curves.

Matthiessen's rule suggests that the total resistance $R(T)$ for magnetic materials is the sum of three terms, $R(T) = R_d + R_{ph}(T) + R_{sd}(T)$. Notice R_d is the temperature-independent term corresponding to the defects embedded in the system. Dy, above the magnetic ordering temperature T_o, is in a paramagnetic state, $R(T > T_o) = R_d + R_{ph}(T > T_o) + R_{sd}^{max}$, where R_{sd} is temperature-independent and takes on its maximum value. Upon cooling through T_o, $R(T < T_o) = R_d + R_{ph}(T < T_o) + R_{sd}(T < T_o)$, a broad kink (or knee) appears in $R(T)$ curves as the spin-disorder scattering weakens and vanishes at the lowest temperatures, as seen in Figs. 4.10(a).

Simple *sp*-electron metals, in the high temperature limit (above the Debye temperature), exhibit resistivity $R(T)$ with linear dependence on temperature. Many lanthanide metals in early studies were also assumed to be linear in temperature even to 0 K in their phonon scattering resistance $R_{ph}(T)$ [6]. This is, however, not valid since the conduction electrons in lanthanides involve a strong *d*-electron band character, which would give rise to a small negative curvature to $R_{ph}(T)$ above T_o, as seen in Fig. 4.10(a). Among the $R(T)$ curves at all pressures, the data at 22 GPa in Fig. 4.10(a) has the widest temperature range (40 K to 295 K) for the $R_{ph}(T)$ contribution to the total resistance. The temperature-dependent canonical phonon resistance $R_{ph}^{22}(T)$ can be then constructed by simply extrapolating this to 0 K. Since the temperature-dependent phonon resistance $R_{ph}(T)$ is also slightly pressure-dependent, for each pressure the $R_{ph}(T)$ can be estimated simply by multiplying the canonical phonon resistance $R_{ph}^{22}(T)$ by a phonon factor α such that for temperatures above T_o the slope of $R(T > T_o)$ matches with that of $\alpha\, R_{ph}^{22}(T > T_o)$

Table 4.2 Values for Dy of the magnetic ordering temperature T_o, maximum spin-disorder resistance R_{sd}^{max} for $T > T_o$, and phonon factor α as a function of pressure to 157 GPa from run 3. Table modified from Ref. [104].

P (GPa)	T_o (K)	R_{sd}^{max} (mΩ)	α
2.1	167	126	0.89
22	40	39	1.0
30	53	118	1.1
56	91	231	0.6
68	99	254	0.5
76	102	271	0.55
96	170	334	0.55
97	195	352	0.55
107	239	369	0.55
119	280	384	0.55
128	300	388	0.55
141	330	392	0.55
145	350	396	0.55
157	370	398	0.55

and the quantity $R(T > T_o) - \alpha\, R_{ph}^{22}(T > T_o)$ becomes temperature independent. Table 4.2 lists the values of the phonon factor α at all pressure to 157 GPa in run 3. Now that the $R(T)$ curves for pressures above 107 GPa appear to have the $R_{ph}(T > T_o)$ above 295 K, the phonon factor α for those pressures are assumed to be the average value 0.55 as seen in Table 4.2.

The spin-disorder resistance $R_{sd}(T)$ for all pressures can be now estimated by subtracting R_d and $\alpha\, R_{ph}^{22}(T)$ from the total resistance $R(T)$, that is, $R_{sd}(T) = R(T) - R_d - \alpha R_{ph}^{22}(T)$, as seen in Fig. 4.12 for pressures to 107 GPa. From 76 GPa and above the knee (magnetic ordering transition) seems to increase dramatically, finally disappearing above 295 K (the maximum temperature limit of the experiment) from 119 GPa so that one cannot determine R_{sd}^{max} directly from resistance data. In order to estimate the maximum spin-disorder resistance R_{sd}^{max} for

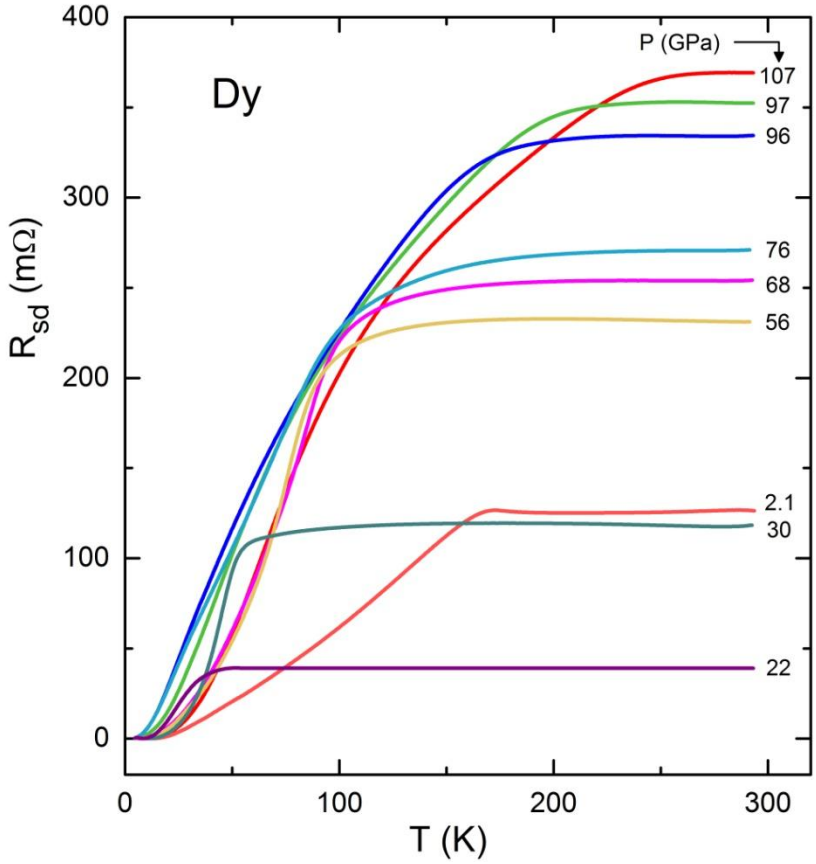

Figure 4.12: Spin-disorder resistance R_{sd} versus temperature curves for Dy from run 3 to 107 GPa where T_o lies below room temperature (295 K). The phonon resistance $R_{ph}(T)$ and defect resistance R_d have been subtracted from the total resistance $R(T)$ in Fig. 4.10(a). Figure taken from Ref. [104].

pressures above 107 GPa, it is assumed that $R_{sd} = R_{sd}(T/T_o)$ for pressures from 96 to 157 GPa. Fig. 4.13 shows the normalized $R_{sd}(T)$ by R_{sd}^{max} versus log T for pressures at 96, 97, and 107 GPa. Notice that over wide temperature range (5 K < T < T_o), the $R_{sd}(T)$ curves for those pressures appear to be roughly parallel to one another on the log T scale. By dividing the $R_{sd}(T)$ data for pressures above 107 GPa by some factors which make them relatively parallel to those at the lower pressures, the values of the temperature-independent and maximum spin-disorder resistance R_{sd}^{max} are estimated and plotted in Fig. 4.13 and also listed in Table 4.2. Now, the

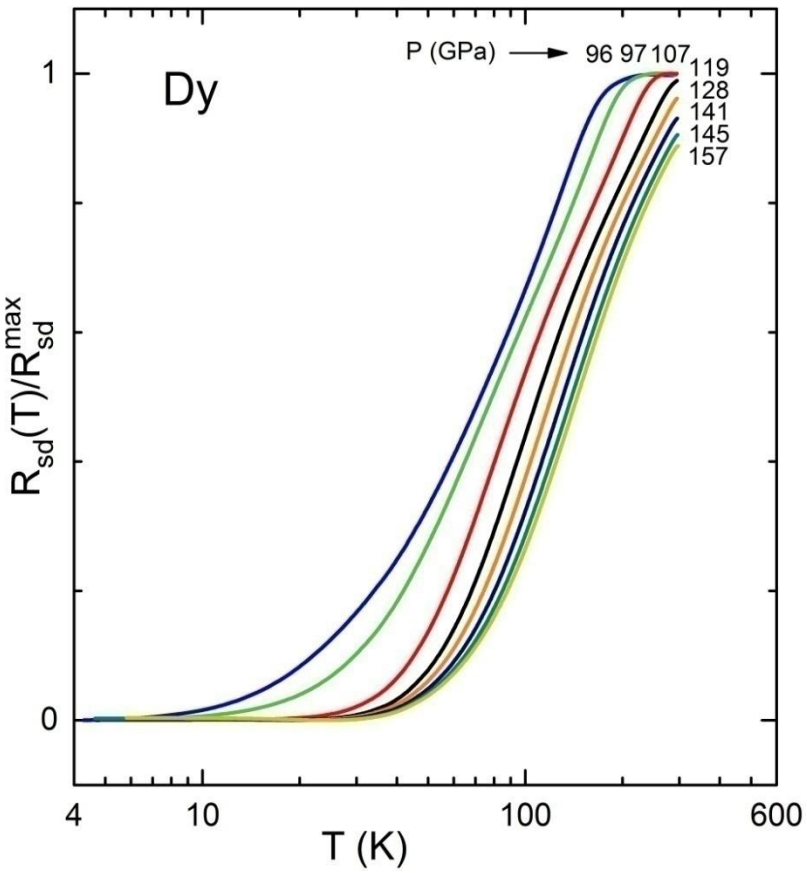

Figure 4.13: Normalized spin-disorder resistance $R_{\mathrm{sd}}(T)/R_{\mathrm{sd}}^{\mathrm{max}}$ versus log T curves for Dy from run 3. At 119, 128, 141, 145, and 157 GPa, $R_{\mathrm{sd}}^{\mathrm{max}}$ is estimated by adjusting slopes to match those at 96, 97, and 107 GPa. Above 107 GPa the pressure dependence of the magnetic ordering temperature T_{o} is estimated from relative horizontal shifts of the curves halfway down the transition. Figure taken from Ref. [104].

magnetic ordering temperature T_{o} and maximum ordering temperature $T_{\mathrm{o}}^{\mathrm{max}}$ for pressures above 107 GPa can be approximately estimated from the shift of $R_{\mathrm{sd}}(T)/R_{\mathrm{sd}}^{\mathrm{max}}$ curves of 96, 97, and 107 GPa along the log T axis to match that of the higher pressures, as listed in Table 4.2.

Fig. 4.14(a) shows the magnetic ordering temperature T_{o} versus pressure for all three experiments on Dy. The results are in good agreement with the earlier studies by Jackson *et al*. [29] to 7.4 GPa and Samudrala *et al*. [106] to 69 GPa. Overall, the pressure dependence $T_{\mathrm{o}}(P)$

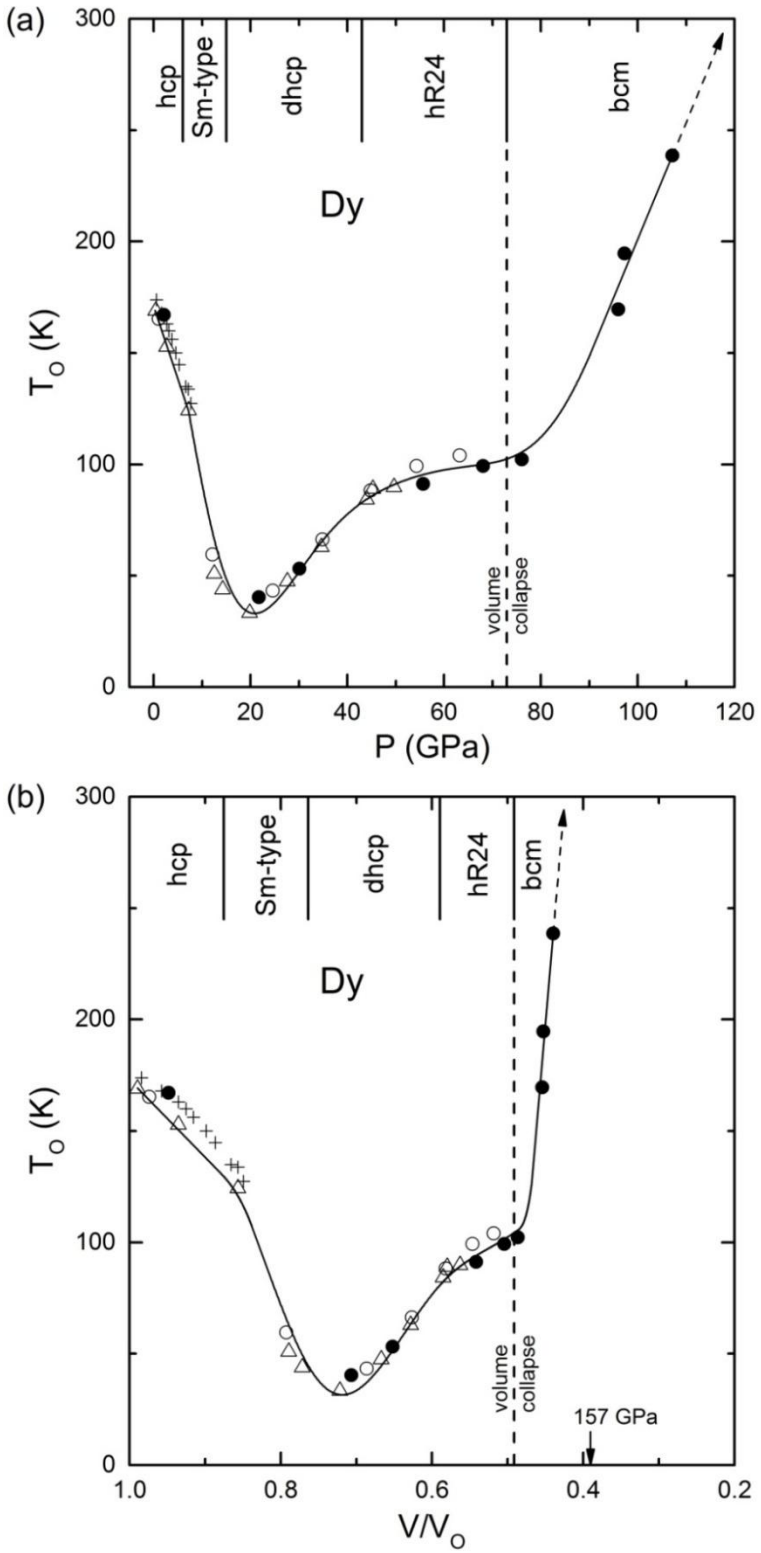

Figure 4.14: T_o of Dy versus (a) pressure or (b) relative volume. (+) earlier studies to 7.4 GPa [29], (Δ) present measurements in run 1, (○) run 2, (●) run 3. Vertical dashed line for volume collapse pressure of Dy at 73 GPa. Crystal structures for Dy [86] at top of graph. Extended solid line is a guide to the eye. Figure taken from Ref. [104].

for Dy appears highly nonmonotonic following the multiple structural transitions denoted at the top of Fig. 4.14 (Notice the phase boundaries are based on room temperature measurements and may slightly change at low temperature). In the graph particularly interesting is the presence of a sharp upturn after 73 GPa, where Dy suffers 6% volume collapse accompanied by a structural transition from hR24 to body-centered monoclinic (bcm). Fig. 4.14(b) shows how sharp the upturn is by plotting T_o versus relative sample volume V/V_o using the known equation of state from Ref. [86]. The rate of increase of $T_o(P)$ below $V/V_o \simeq 0.51$ (above 73 GPa) is much steeper than the initial rate of decrease of $T_o(P)$ near $V/V_o = 1$ (to 7.4 GPa). According to the analysis and linear extrapolation, the magnetic ordering temperature T_o exhibits anomalously high values in the range 370–430 K at 157 GPa, which would be the highest known transition temperature among the lanthanides (current highest value is 292 K for Gd at ambient pressure [6]).

4.2.2 Terbium

Two separate high pressure resistivity measurements were carried out on elemental terbium (Tb) metal. Fig. 4.15 shows data from run 1 for the electrical resistance R versus temperature T at 18 different pressures up to 135 GPa. Run 2 is plotted in Fig. 4.16 with $R(T)$ curves at 17 different pressures in range 2-141 GPa. The magnetic ordering transition T_o is identified by a kink (or a knee shape at higher pressures due to pressure gradient on the sample) in the temperature-dependant resistance curve, for example around 210 K in $R(T)$ at 2 GPa from run 1 (see Fig. 4.15). The kink in the $R(T)$ curve originates from the suppression of spin-disorder scattering $R_{sd}(T)$ through the effect of magnetic ordering of Tb^{3+} ions.

In order to facilitate the identification of the magnetic transition, in Fig. 4.17 the selected $R(T)$ curves from run 2 are plotted again in a vertically shifted manner. The phonon resistance

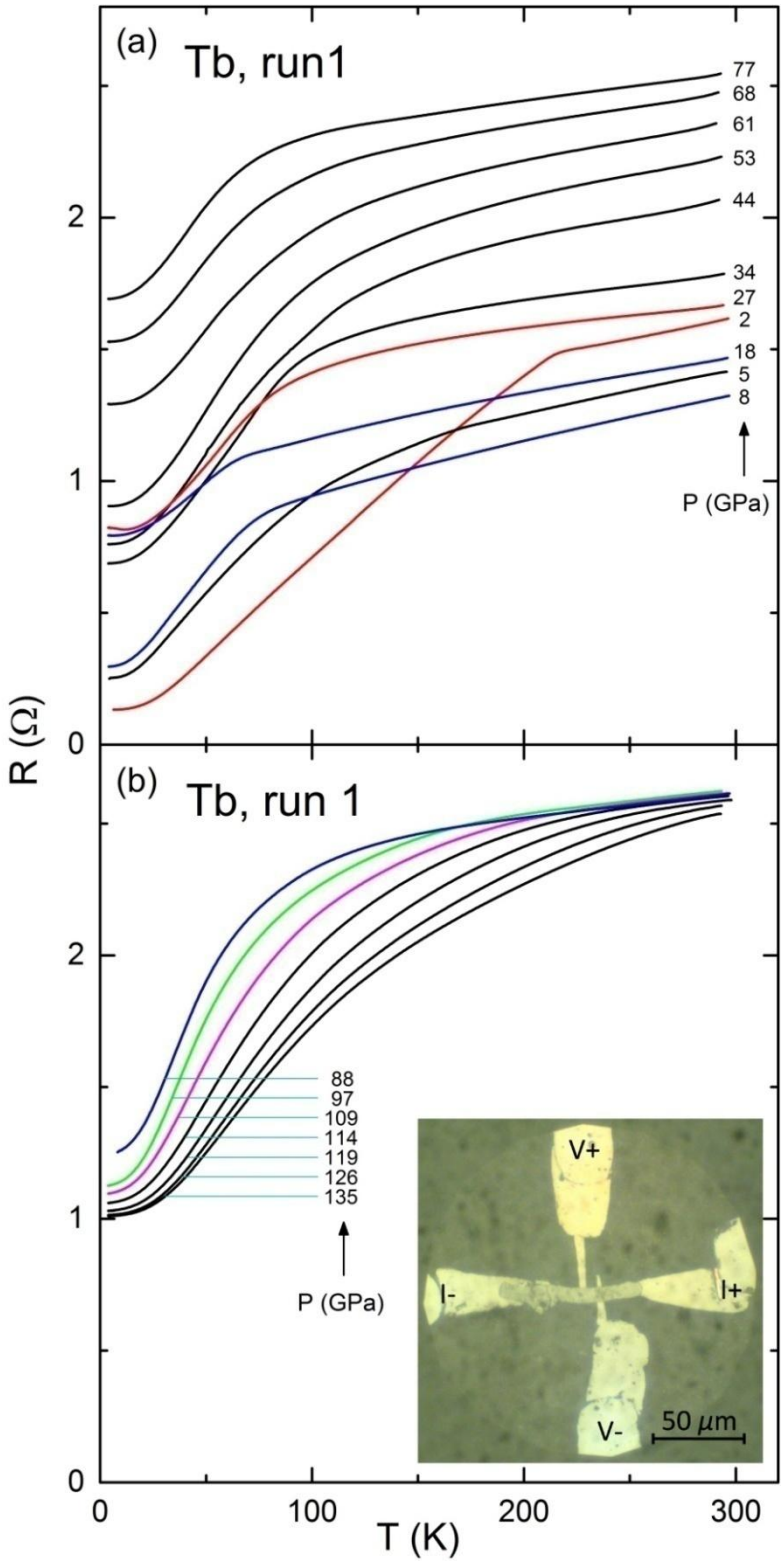

Figure 4.15: Resistance of Tb from run 1 versus temperature in pressure ranges: (a) 2–77 GPa, and (b) 88–135 GPa. The kink in the resistance curve remarks magnetic ordering transition. Inset in (b) shows image of elongated Tb sample ($\sim 8 \times 80 \times 3\ \mu m^3$) and 180 μm diameter central flat of diamond culet. Figure modified from Ref. [107].

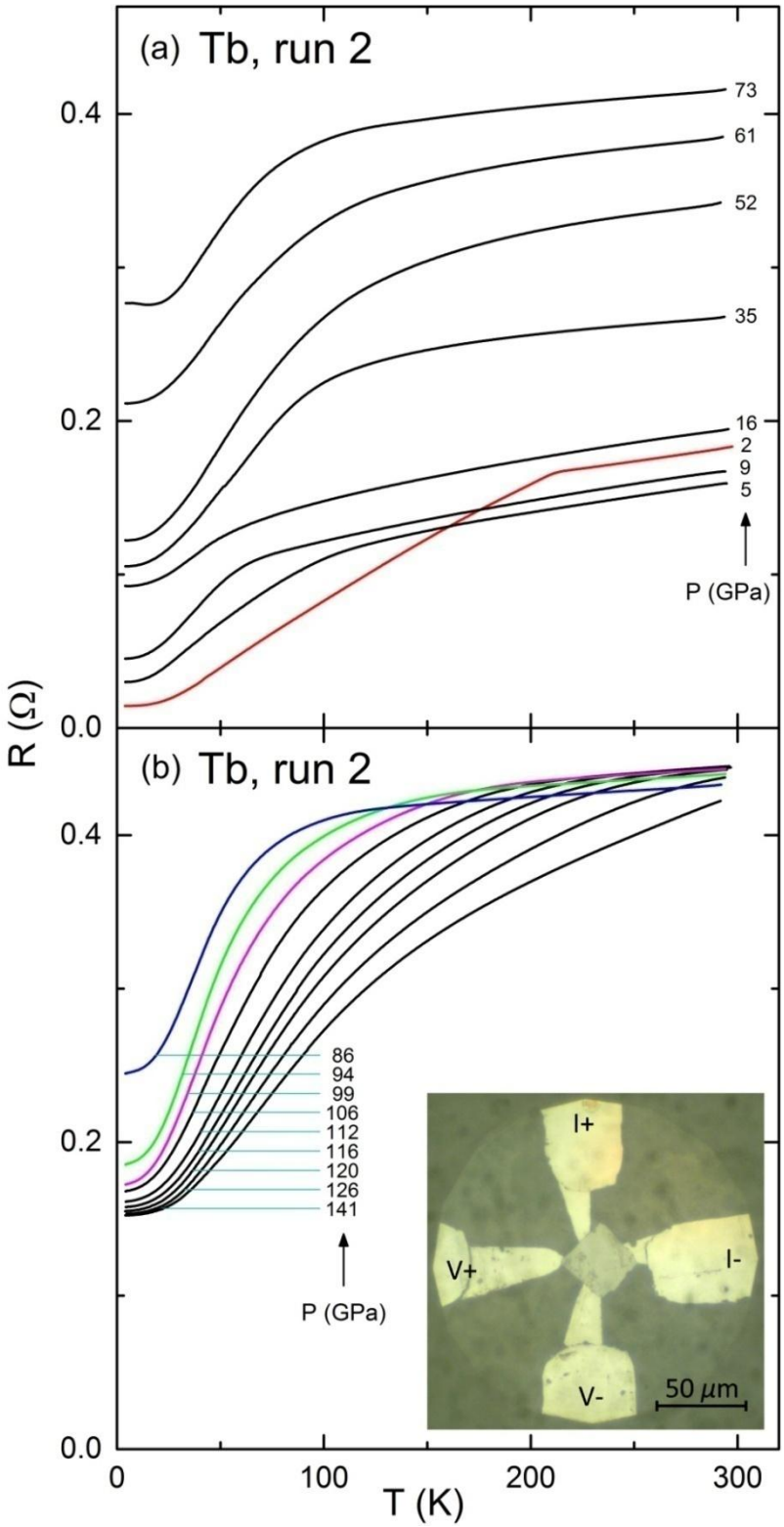

Figure 4.16: Resistance of Tb from run 2 versus temperature in pressure ranges: (a) 2–73 GPa, and (b) 86–141 GPa. The kink in the resistance curve remarks magnetic ordering transition. Inset in (b) shows image of square Tb sample ($\sim 30 \times 30 \times 5\ \mu m^3$) and 180 μm diameter central flat of diamond culet. Figure modified from Ref. [107].

contribution $R_{ph}(T)$ is given by the red lines using $R(T)$ at 16 GPa (with extrapolation to 0 K) as the canonical phonon resistance. The same analysis was used for the Dy measurements. The values of the phonon factor α for Tb are listed in Table 4.3 for runs 1 and 2 at all pressures. T_x is defined by the intersection of the red (phonon resistance) curve with the low temperature tangent red line, as seen in Fig. 4.17. Tb is in a paramagnetic state, which is the relatively flat region above the knee in the $R(T)$ curves where the red (phonon) line overlaps the data. When the red line starts to deviate from the original $R(T)$ curve, it reveals that the magnetic ordering transition has set in. Due to the presence of pressure gradient across the sample, some regions of the sample will exhibit a lower magnetic ordering temperature and, as a result, the kink broadens to a knee at higher pressures. Note that for pressures above 120 GPa the knee appears to rise above room temperature (the highest temperature of this experiment). The average values like $\alpha = 0.69$ for run 1 and $\alpha = 0.41$ for run 2 are assumed in Table 4.3 for pressures of 120 GPa and above.

Fig. 4.18 shows selected spin-disorder resistance $R_{sd}(T)$ curves at 5, 35, and 86 GPa in run 2 after subtracting phonon and defect contributions from the total resistance ($R_{sd}(T) = R(T) - \alpha R_{ph}^{16}(T) - R_d$). Above the magnetic transition temperature, R_{sd} takes on its maximum value with no temperature dependence, which is R_{sd}^{max}, as listed in Table 4.3 for all pressures from runs 1 and 2. The average magnetic ordering temperature T_o is defined by the intersection of the two straight red lines as seen in Fig. 4.18. Since the pressure gradient across the sample results a variation of the magnetic ordering temperature as seen in the knee shape transition, it is useful to define the maximum ordering temperature T_o^{max}, at which the spin-disorder resistance $R_{sd}(T)$ drops from its maximum value by 1%. When dT_o/dP is positive, then T_o^{max} represents the magnetic ordering temperature at the center of the sample where the pressure is highest. All

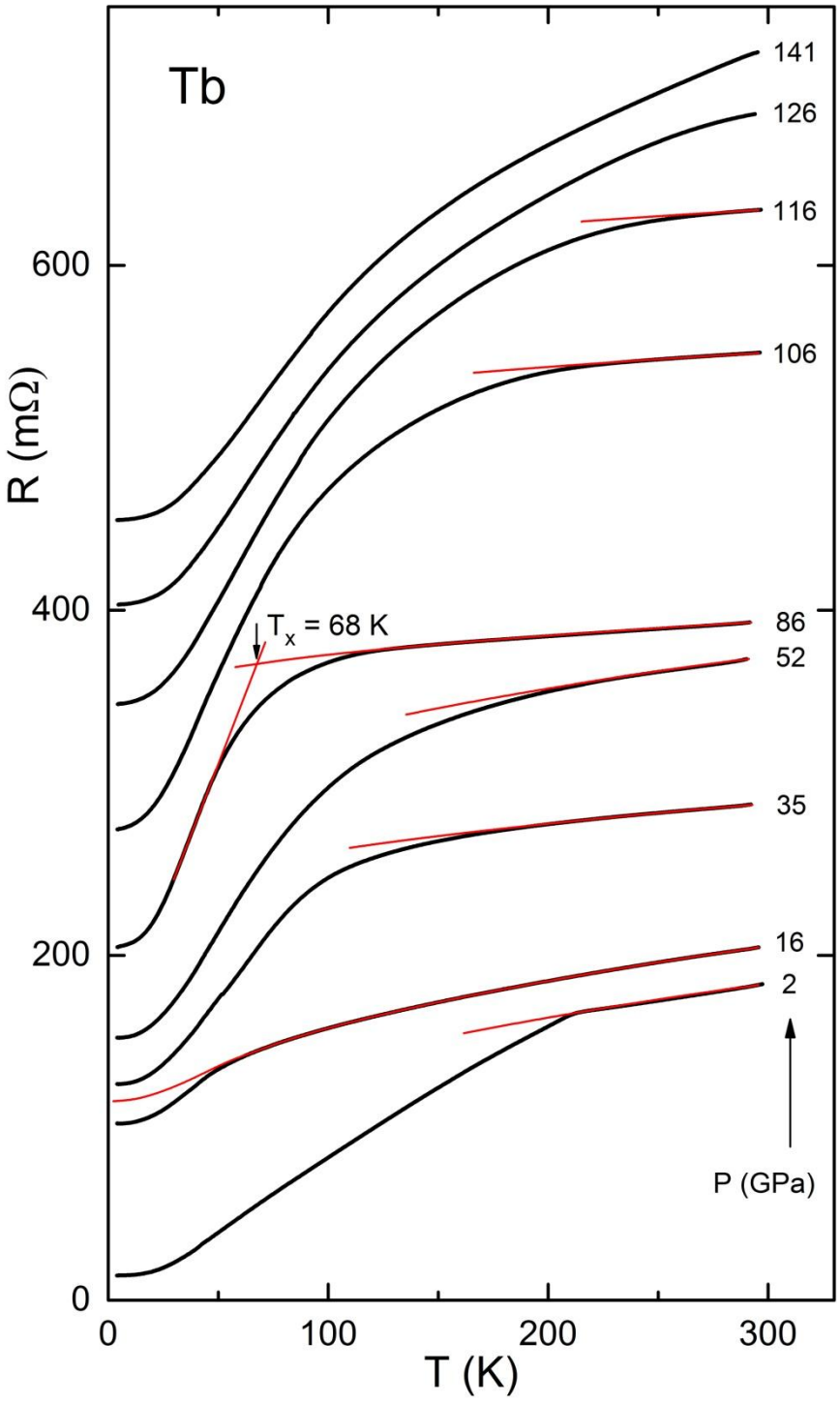

Figure 4.17: Selection of temperature-dependent resistance curves for Tb from run 2 in Fig. 4.16. Notice that the curves have been shifted vertically for clarity, except for 2 GPa. Red lines with small positive slope give temperature-dependent phonon resistance curves for $T \gtrsim T_x$. R(T) at 16 GPa is used as a canonical phonon resistance curve, which is extended to 0 K. Figure taken from Ref. [107].

Table 4.3 Values for Tb of the average and maximum magnetic ordering temperatures T_o and T_o^{max}, maximum spin-disorder resistance R_{sd}^{max} for $T > T_o^{max}$, and phonon factor α as a function of pressure to 135 GPa from run 1 and to 141 GPa from run 2. Table modified from Ref. [107].

run	P (GPa)	T_o (K)	T_o^{max} (K)	R_{sd}^{max} (mΩ)	α	run	P (GPa)	T_o (K)	T_o^{max} (K)	R_{sd}^{max} (mΩ)	α
1	2	211	214	881	1.16	2	2	208	210	83	0.98
1	5	117	163	523	1.24	2	5	103	142	43	0.98
1	8	73	84	380	1.24	2	9	57	66	36	0.98
1	18	64	70	154	1.0	2	16	52	66	13	1.0
1	27	95	145	513	0.66	2	35	106	177	111	0.58
1	34	101	165	721	0.72	2	52	111	199	138	0.92
1	44	112	188	769	1.02	2	61	101	183	103	0.79
1	53	105	196	746	1.11	2	73	82	159	91	0.56
1	61	101	179	518	1.05	2	86	69	113	152	0.41
1	68	86	154	479	0.89	2	94	76	154	219	0.41
1	77	72	105	469	0.74	2	99	88	180	234	0.41
1	88	73	145	1001	0.69	2	106	111	205	239	0.41
1	97	83	173	1140	0.69	2	112	133	232	247	0.41
1	109	107	206	1165	0.69	2	116	148	249	250	0.41
1	114	131	230	1189	0.69	2	120	163	274	252	0.41
1	119	150	253	1201	0.69	2	126	183	306	252	0.41
1	126	172	291	1211	0.69	2	141	203	341	243	0.41
1	135	192	323	1214	0.69						

values of T_o and T_o^{max} in both runs are listed in Table 4.3.

Fig. 4.19(a) is plotted with all the values of T_o and T_o^{max} (from Table 4.3) as a function of pressure to 141 GPa, the maximum pressure of the experiment. T_o^{max} is seen as light blue data connected to the value of T_o. Since above 120 GPa, T_o^{max} appears to rise above room temperature (available maximum temperature of the experiment), both magnetic ordering temperatures T_o and T_o^{max} are estimated in the same way as described for Dy (see Section 4.2.1). The initial pressure dependence of the magnetic ordering temperature is in good agreement with previously studied

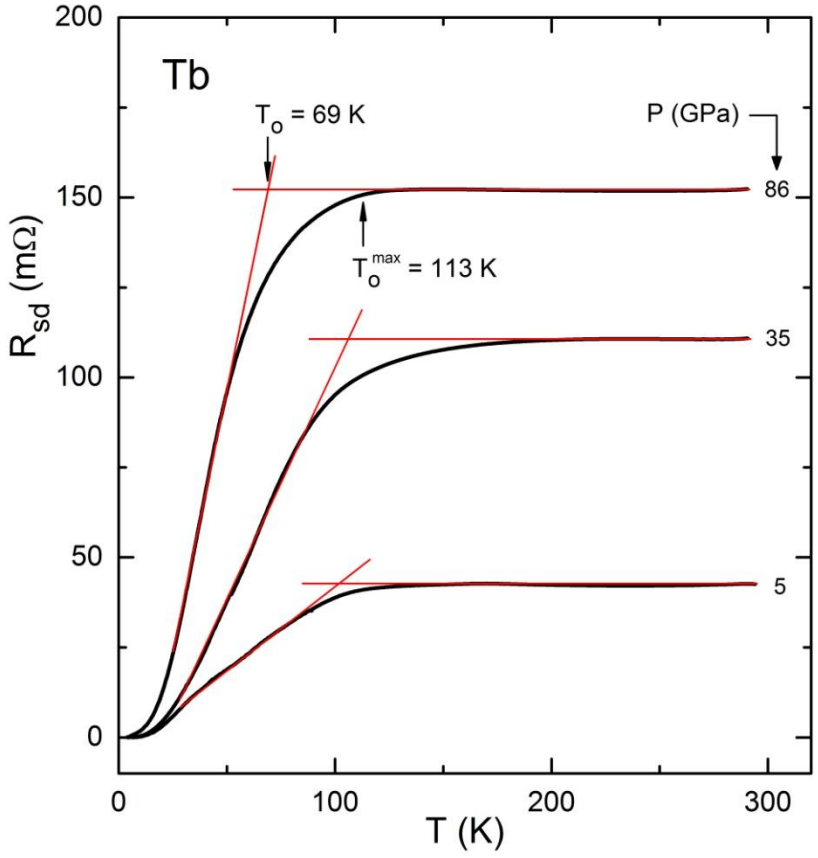

Figure 4.18: Selected spin-disorder resistance R_{sd} curves versus temperature T for Tb at three pressures from run 2. The phonon resistance $R_{ph}(T)$ and defect resistance R_d have been subtracted from the total resistance $R(T)$. The average magnetic ordering temperature T_o is defined by intersection point of two tangent lines. T_o^{max} gives temperature at which maximum spin-disorder resistance has dcreased by 1%. Figure taken from Ref. [107].

ac magnetic susceptibility measurements by Jackson *et al*. [29] to 6.3 GPa. For higher pressures $T_o(P)$ becomes in a highly non-monotonic fashion, corresponding to the several structural phase transitions as seen at the top of Fig. 4.19(a) (the crystal structures are indentified by x-ray diffraction measurements at room temperature and may shift somewhat at low temperatures). Comparing $T_o(P)$ for Tb in Fig. 4.19(a) with $T_o(P)$ for Dy in Fig. 4.14(a), the similarity of the magnetic phase diagrams stands out below their volume collapse pressures P_{vc} indicating that

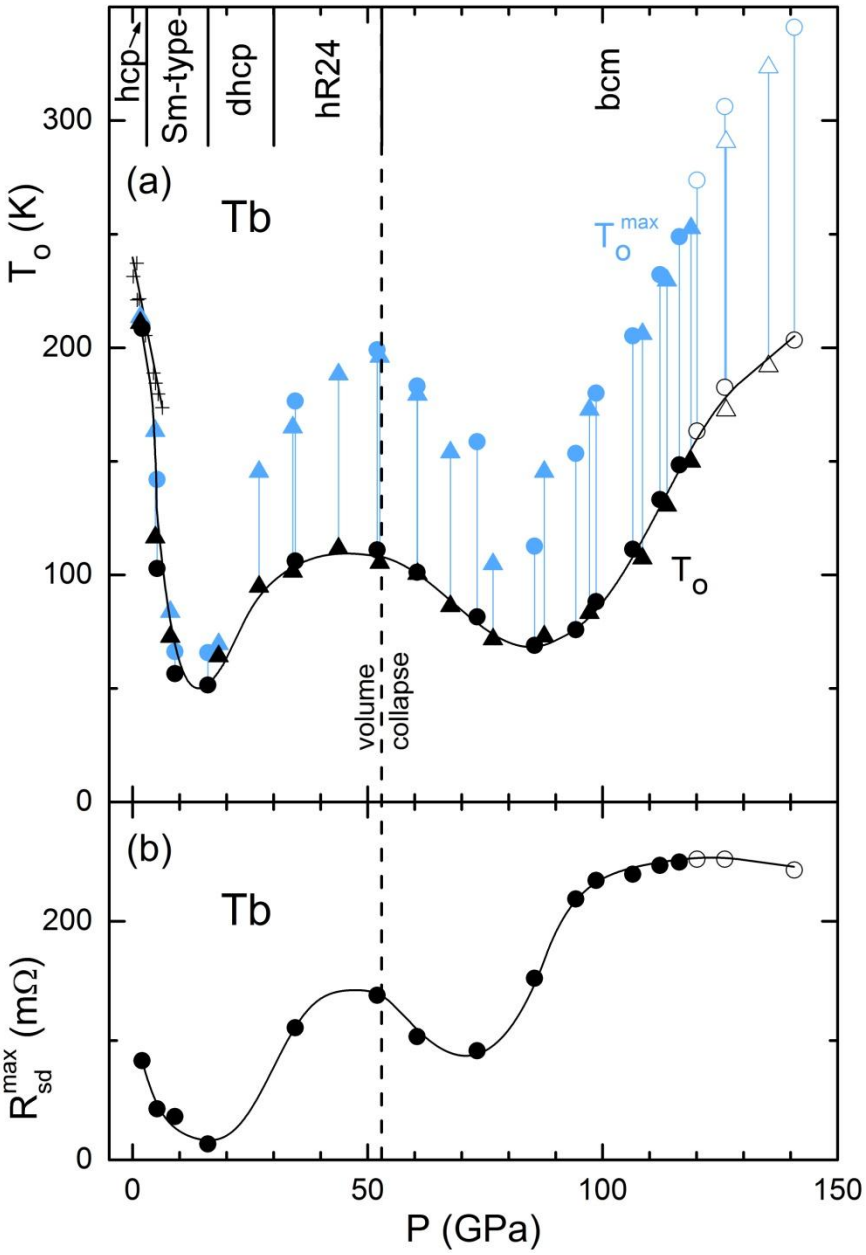

Figure 4.19: (a) Average magnetic ordering temperature T_o of Tb versus pressure. (+) earlier susceptibility studies to 6.3 GPa [29], (▲) present measurements in run 1, (●) run 2. Light blue data connected vertically to each value of T_o gives maximum ordering temperature T_o^{max} at that pressure. Open symbols indicate estimated values according to the shift in the $R_{sd}(T)/R_{sd}^{max}$ curves. Vertical dashed line marks volume collapse pressure of Tb at 53 GPa. Crystal structures for Tb [85] are seen at top of graph. (b) R_{sd}^{max} versus pressure from run 2 appears to track the trend of $T_o(P)$ in (a). In both graphs the extended solid line is for a guide to the eye. Figure modified from Ref. [107].

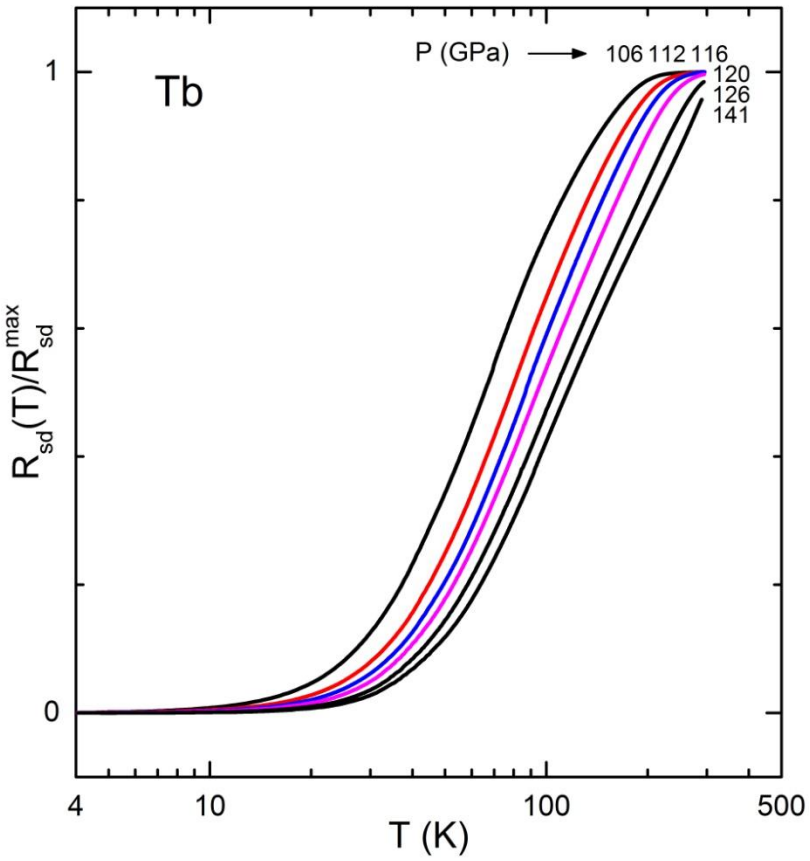

Figure 4.20: Normalized spin-disorder resistance $R_{sd}(T)/R_{sd}^{max}$ versus log T curves for Tb from run 2. At 120, 126, and 141 GPa, R_{sd}^{max} is estimated by adjusting slopes to match those at 106, 112, and 116 GPa. Above 107 GPa the pressure dependence of the magnetic ordering temperature T_o is estimated from relative horizontal shifts of the curves. Figure taken from Ref. [107].

perhaps the same mechanism is responsible. On the other hand, for pressures above P_{vc} for Tb the initial decrease of T_o right before going up rapidly at around 80 GPa significantly differs from that of Dy. By using the known equation of state for Tb [85], T_o versus the relative volume V/V_o reveals that the increase of T_o at around 80 GPa is much sharper than the initial decrease of T_o to 6.3 GPa. As seen in Fig 4.20, the same analysis by the relative horizontal shift in the $R_{sd}(T)/R_{sd}^{max}$, which was applied to Dy to estimate quantitatively the values of T_o above room temperature, shows that the average magnetic ordering temperature T_o at 141 GPa is anticipated

to be 199 K and the maximum ordering temperature T_o^{max} to be 333 K. In Fig. 4.19(b) the bottom graph shows that the spin-disorder resistance in the paramagnetic state R_{sd}^{max} tracks the magnetic ordering temperature T_o as a function of pressure, as found previously for Dy.

4.2.3 Gadolinium

It is interesting to compare $T_o(P)$ for Dy and Tb with that for the magnetically most stable element Gd (gadolinium) [108]. Fig. 4.21 shows the magnetic ordering temperature T_o in Gd versus pressure to 105 GPa from two separate experiments. As in the case for Dy and Tb, a remarkable similarity is found in the $T_o(P)$ for Gd below its volume collapse pressure P_{vc} at 59 GPa. On the other hand, above P_{vc}, $T_o(P)$ for Gd significantly differs from that of Dy and Tb in that $T_o(P)$ only gradually increases over the entire pressure ranges from 59 to 105 GPa with no sign of any sharp upturn, although the same structural transition from hR24 to bcm as in Dy and Tb occurs with a 5% of volume collapse.

4.3 Discussion

The experimental results in the previous section have showed a highly nonmonotonic pressure dependence of the magnetic ordering temperature T_o for Dy, Tb, and Gd below P_{vc}, the pressure where the volume collapse occurs for each element. In that pressure range, the $T_o(P)$ magnetic phase diagrams of Dy, Tb, and Gd are very similar, indicating that the same mechanism is likely responsible, one which can be characterized as magnetically conventional (or stable) obeying de Gennes scaling. Above P_{vc} $T_o(P)$ increases sharply for Dy and for Tb (after the initial decrease), but not for Gd, suggesting that under extreme pressures Dy and Tb are transformed into an unconventional (or unstable) magnetic state, which possibly involves Kondo

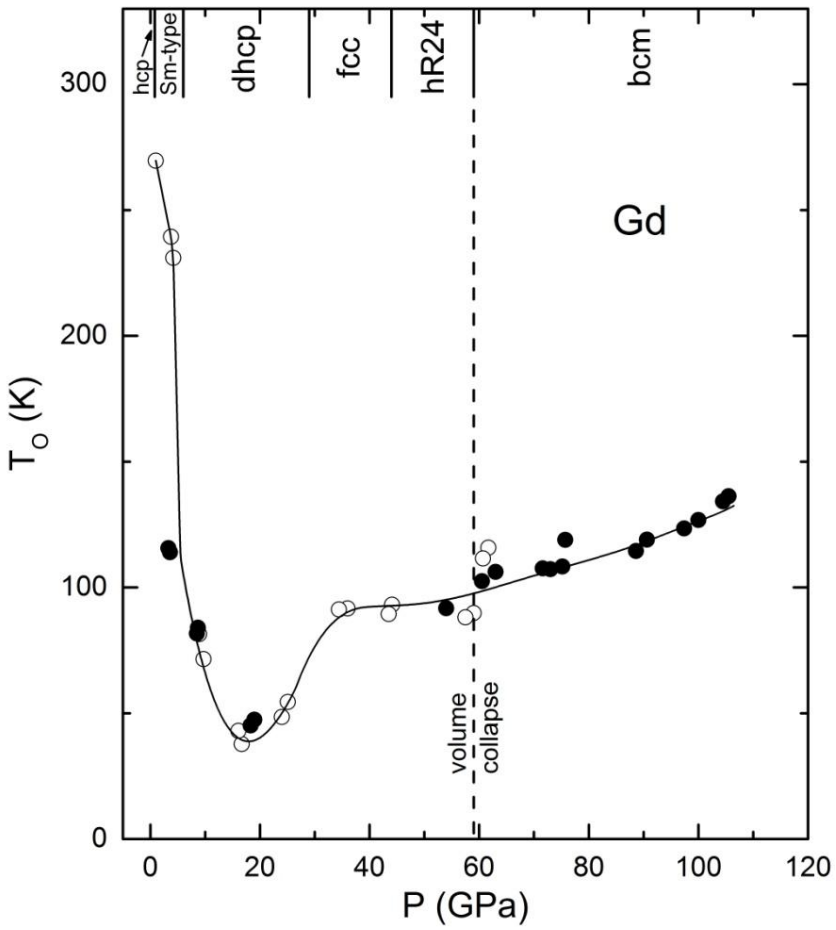

Figure 4.21: Magnetic ordering temperature T_o of Gd versus pressure to 105 GPa in two experiments (○) run 1, (●) run 2. Vertical dashed line marks for volume collapse pressure of Gd at 59 GPa. Crystal structures are at top of graph for Gd [83,109]. Extended solid line is a guide to the eye. Figure taken from Ref. [104].

physics. In contrast, Gd remains magnetically stable for pressures above P_{vc}.

4.3.1 Conventional Magnetic Ordering below P_{vc}

The magnetic phase diagrams $T_o(P)$ of Dy, Tb, and Gd to P_{vc} (where their atomic volume collapse occurs at 73, 53, and 59 GPa respectively) are remarkably similar (see Figs. 4.14(a), 4.19(a), and 4.21), indicating that a common mechanism seems likely in this pressure range. The fact that the local magnetic state of Gd with its half-filled $4f^7$ is magnetically by far the most

stable of all lanthanides suggests that for pressures below P_{vc} Dy, Tb, and Gd remain in a conventional (stable) magnetic state following de Gennes scaling.

The RKKY indirect exchange interaction for a particular lanthanide ion with a local magnetic moment results in magnetic ordering at a temperature T_o, given by Eq. 2.8. Considering the pressure dependence of each term in Eq. 2.8 provides insight into the anticipated behavior of the magnetic ordering temperature T_o under high pressure (here we do not consider any valence transition under pressure, which would affect the value of the de Gennes factor itself). The last term $\phi\left(2k_F\left|\mathbf{R}_i-\mathbf{R}_j\right|\right)$ in Eq. 2.8 has little pressure dependence since in the first approximation $\left|\mathbf{R}_i-\mathbf{R}_j\right|$ is proportional to a as well as $k_F \sim 1/a$, in the free electron approximation where a represents the interatomic distance [29]. As a result, the pressure-dependent terms in Eq. 2.8 may be written as

$$T_o \propto \left[J^2 N(E_F)\right]\left[\left(g_J-1\right)^2 J_t(J_t+1)\right], \tag{4.1}$$

where J is the exchange coupling constant between the 4*f* ion and the surrounding conductions electrons, $N(E_F)$ is the density of states at the Fermi level, g_J is the Landé-g factor, and J_t is the total angular momentum determined according to Hund's rules (see Table 4.1). The second term is known as the so-called de Gennes factor $(g_J-1)^2 J_t(J_t+1)$.

The fact that the de Gennes factor would remain unchanged (as in the case of Tb [103] and Gd [76]), unless a valence transition occurs under pressure, gives weight to the pressure dependence of $J^2N(E_F)$ as the origin of the strong similarity between the highly nonmonotonic pressure dependencies of T_o for Dy, Tb, and Gd below P_{vc}. This idea also gets support from the almost identical sequence of the structural phase transitions under pressure [83,85,86] (driven by

the enhancement of the *d* character in the conduction band [110]), which also causes distinct changes in the shape of the Fermi surface. In fact, electronic structure calculations for Dy [111] and mean field theory method for Gd [112] suggest that the large decrease in $N(E_F)$ is responsible for the sharp negative initial pressure dependence of T_o [113].

4.3.2 Strong Enhancement of Magnetism in Dy and Tb at Extreme Pressure

What might be then the driving mechanism for the dramatic increase of magnetic ordering temperature T_o for Dy and Tb under extreme pressures above P_{vc}, the pressure where the volume collapse occurs? According to the volume collapse models involving 4*f* electrons, it might be a result from (1) increase in valence driven by promotion of a 4*f* electron to the *spd*-electron conduction band, (2) local-to-itinerant transition of the 4*f* state through increased overlap of 4*f* wave functions, (3) approach of the localized 4*f* level to the Fermi level (E_F) leading to strong Kondo screening (or Kondo physics).

Recent synchrotron spectroscopy measurements such as x-ray absorption near-edge structure (XANES) and nonresonant x-ray emission spectroscopy (XES) studies on Tb to extreme pressures (well above P_{vc} at 53 GPa) performed by Fabbris *et al.* [103] (see Fig. 4.22) have shown that there is no change either in valence nor in the bare 4*f* local moment across the volume collapse pressure P_{vc}, strongly supporting the Kondo volume collapse model for Tb, as seen in Fig. 4.22. Due to its close proximity to Gd, whose magnetic state is the most stable of all lanthanides, Tb with $4f^8$ would be more likely to undergo a valence transition than Dy with $4f^9$. Therefore, it is reasonable to anticipate that Dy, as for Tb, would remain trivalent with a strongly localized $4f^9$ state across its P_{vc} at 73 GPa, also giving support to the Kondo physics scenario for Dy. Perhaps, the volume collapse itself is a strong signature revealing that Dy and Tb are

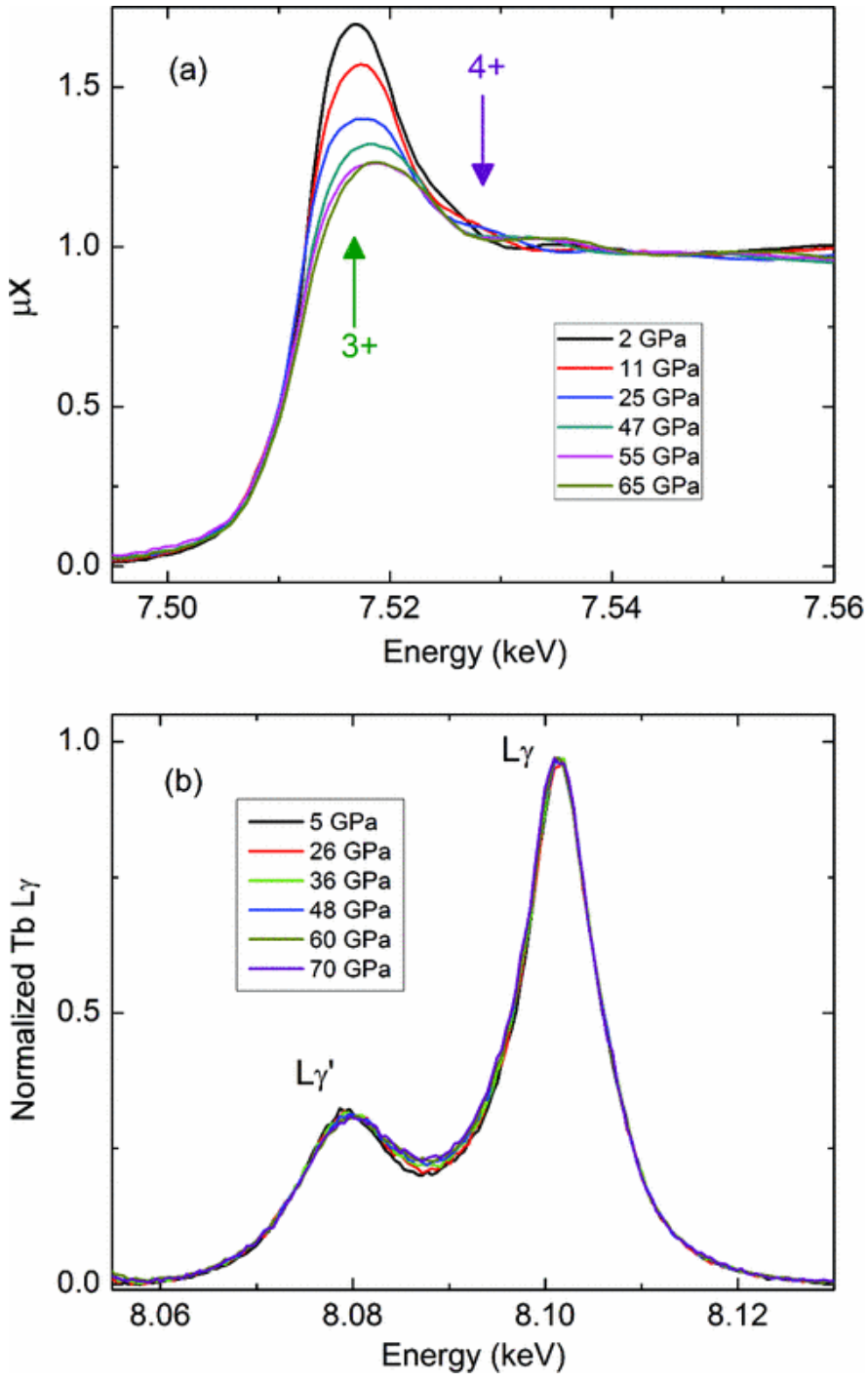

Figure 4.22: (a) Pressure dependence of L_3 XANES data for Tb showing no 4+ or mixed valence transition to 65 GPa (P_{vc} at 53 GPa for Tb) at room temperature. Arrow for 3+ (4+) marks absorption peak position of trivalent (tetravalent) Tb. (b) Pressure dependence of L_γ nonresonant XES data for Tb showing no change in $4f^8$ local magnetic moment (no $4f^8$ local-itinerant transition) to 70 GPa. Figure taken from Ref. [103].

entering a region of anomalous magnetism with dense Kondo behavior and in turn experiencing anomalously high magnetic ordering temperatures T_o at extreme pressures.

It is well known that superconductivity is very sensitive to magnetism in that they normally compete with each other. Superconductivity in a metal even can be rapidly destroyed by adding magnetic impurities (time-reversal symmetry breaking). Therefore, superconductivity is an excellent probe to investigate the properties of a local magnetic impurity (an ion with local moments) in superconducting host metals at ambient or high pressure. Such behavior of superconductivity led Maple, Wittig, and Kim [34] to carry out the experiments tracking the superconducting transition temperature $T_{c,alloy}$ as a function of pressure in the dilute magnetic alloy of La(Ce) and found that $T_{c,alloy}$ shows a strong Kondo sinkhole-like suppression around 0.7 GPa compared to $T_{c,host}$ for La, the pressure where Ce's volume collapse occurs, as seen in Fig. 4.6(c). The degree of suppression of superconducting transition temperature of a superconducting host metal by a substituted magnetic impurity in the alloy under pressure, $\Delta T_c(P) = T_{c,host}(P) - T_{c,alloy}(P)$, identifies the type of the pressure-induced pair breaking (breaking up the electron-electron pair) [98]. Yttrium (Y) appears to be the ideal host superconductor for Dy, Tb, and Gd ions (magnetic impurity) since the properties of the *spd*-electron conduction band, the structural sequence, and the elemental metallic radii closely match with that of the heavy lanthanides [103].

Two separate four-point electrical resistivity measurements were carried out on the dilute magnetic alloy Y(1 at.% Dy) under extreme pressures. Fig. 4.23(a) shows the electrical resistance *R* versus temperatures *T* at 7 different pressures up to 73 GPa from run 1. In Fig. 4.23(b) the same kind graph is plotted from run 2 at 12 different pressures to approximately 114

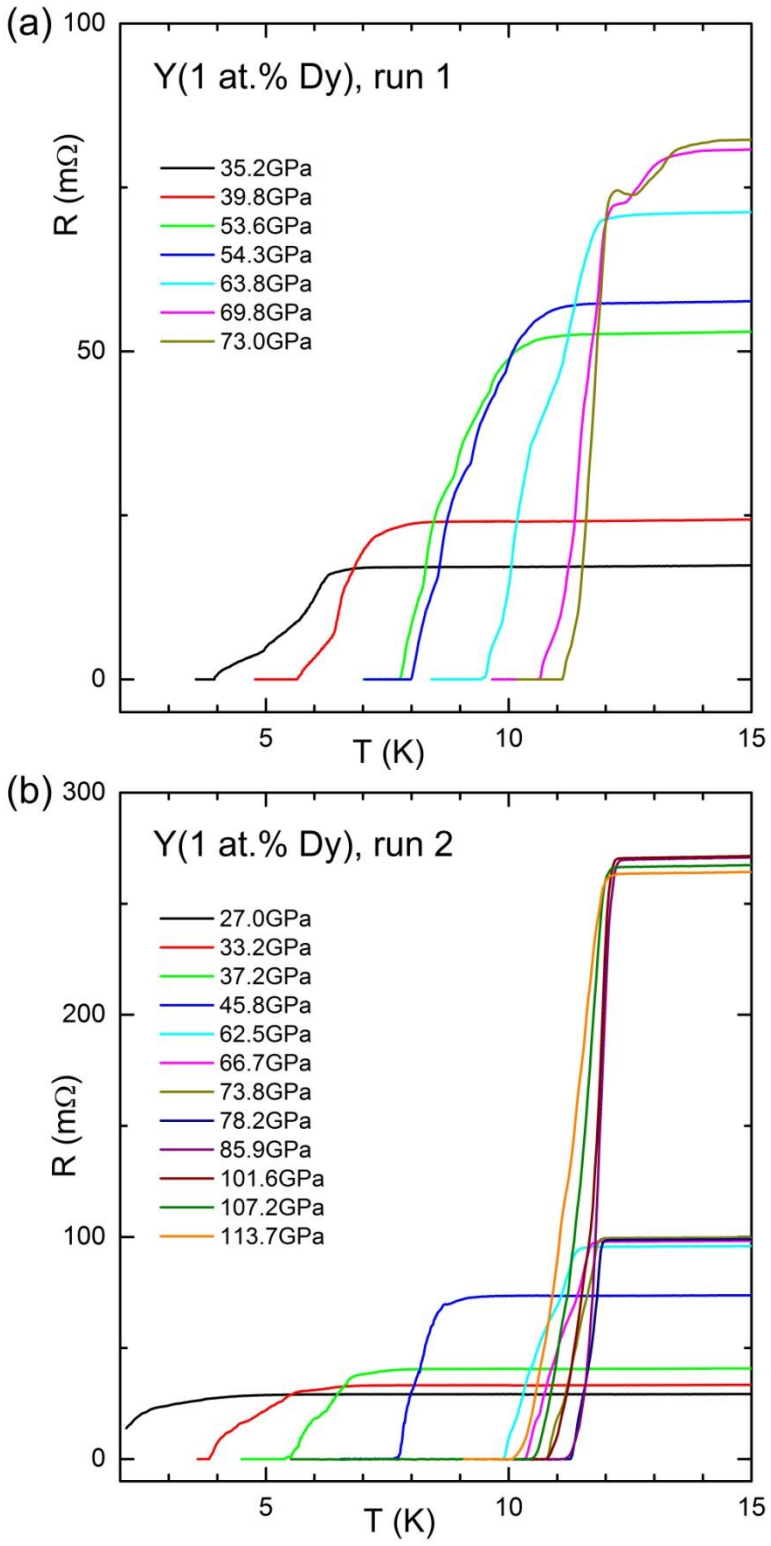

Figure 4.23: Resistance versus temperature for Y(1 at.% Dy) from (a) run 1 to 73 GPa and (b) run 2 to 114 GPa. The superconducting transition temperature T_c is defined at that temperature where the temperature-dependent resistance curve drops down by 50%. In both graphs the superconducting transition temperature initially increases with pressure.

GPa. As expected in the four-point method, the resistance R vanishes to zero below the superconducting transition temperature T_c for all pressures except for 27 GPa in Fig. 4.23(b) where it was restricted by the low temperature limit of the experiment. The width of the superconducting transition is related to both the pressure gradient across the sample (due to the non-hydrostatic pressure medium) and the feature of the $T_c(P)$ whether it passes through a maximum (or minimum) or keeps increasing (or decreasing). Notice that above 63 GPa the width of the superconducting transition narrows considerably, in spite of the pressure gradient across the sample, consistent with the fact that $T_c(P)$ passes through a maximum.

Fig. 4.24(a) shows the pressure dependence of the superconducting transition temperature $T_c(P)$ of Y(1 at.% Dy) in comparison with the published $T_c(P)$ data for superconducting Y metal from ac susceptibility measurements [114]. Below 70 GPa T_c(P) for Y(1 at.% Dy) seems to track that for pure Y with a somewhat reduced slope, but just above 73 GPa, where elemental Dy suffers 6% volume collapse, the difference in superconducting transition temperature ΔT_c increases rapidly, reaching nearly 9 K at the highest pressure 114 GPa. As found in La(Ce), La(Pr), and Y(Pr) in the previous studies (see Section 4.1.3), such a drastic suppression of superconductivity in the Y host metal by 1 at.% Dy magnetic impurity points to giant Kondo pair breaking.

Fig. 4.24(b) [103] shows the superconducting transition temperature T_c of Y(0.5 at.% Tb) versus pressure compared to that for pure Y [114]. Beginning at around 54 GPa, where pure Tb metal undergoes a 5% volume collapse, the $T_c(P)$ dependence for the alloy metal also markedly deviates from that of elemental Y metal, reaching a maximum suppression $\Delta T_c \approx 5$ K at 81 GPa, the highest pressure of the experiment. As has been observed in Y(Dy), this strong suppression

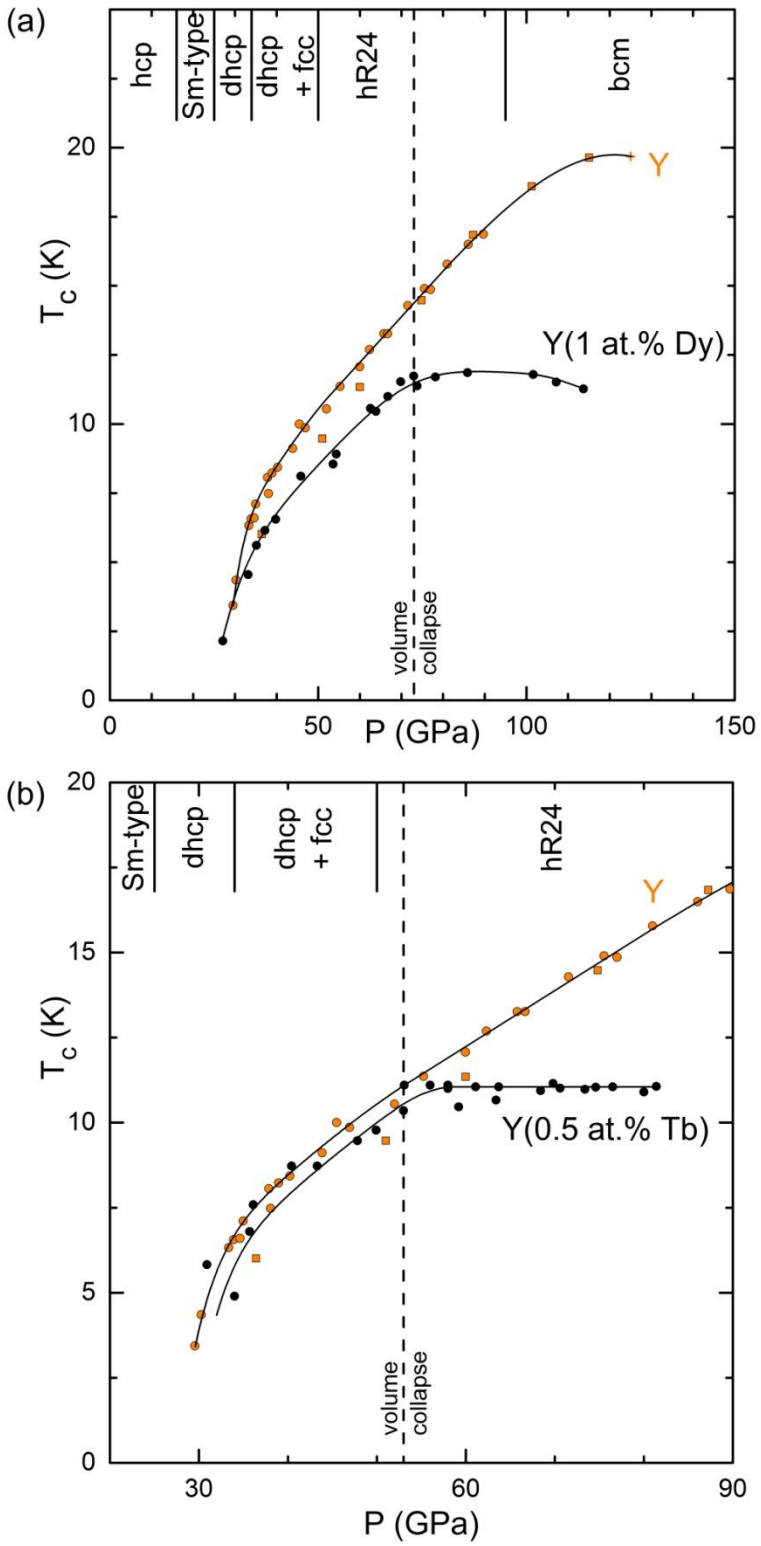

Figure 4.24: Superconducting transition temperature T_c versus pressure for (a) Y(1 at.% Dy) and (b) Y(0.5 at.% Tb) compared to that for Y [114]. In both graphs the vertical dashed lines mark pressure of volume collapse for Dy at 73 GPa and Tb at 53 GPa. At top of both graphs are crystal structures taken on by superconducting host Y [115]. Figures taken and modified from Refs. [103,104].

of superconductivity in Y host metal by dilute Tb ions also points to strong Kondo effect in pair breaking.

The question is then how the Kondo physics gives rise to the rapid increase in $T_o(P)$ for Dy above P_{vc} and for Tb above some point after P_{vc}. The total exchange coupling constant J includes a positive parallel coupling J_+ and a negative anti-parallel coupling J_- between a magnetic ion and the surrounding conduction electrons in the indirect exchange interaction (RKKY interaction) [116]. For elemental lanthanide metals, J_- is dependent on the mixing matrix element V_{sf} (subscripts *s* and *f* refer to conduction electrons and localized magnetic ions respectively) and the 4*f*-electron stabilization energy E_{ex} in the relation $J_- \propto -|V_{sf}|^2/E_{ex}$, where E_{ex} is relatively small in comparison to the electron-electron Coulomb repulsion in the same orbital [117]. As the energy level of the 4*f*-state approaches close to the Fermi level by applying pressure, E_{ex} decreases and at the same time V_{sf} increases. Therefore, J_- becomes large and dominates in the total exchange coupling constant $J = J_+ + J_-$. In this stage, the local magnetic moment starts to be compensated by the spins of conduction electrons through the so-called Kondo screening, which will exponentially increase with J (namely $T_K \propto \exp[-1/|J|N(E_F)]$, see Section 2.4.3) as proposed by Doniach in his Kondo lattice model (KLM) [36,118]. Since the magnetic ordering temperature T_o is proportional to J^2, it is suggested that the initial process of Kondo lattice behavior leads to an anomalously high magnetic ordering temperature T_o, as seen in Dy and Tb at extreme pressure above P_{vc}. This competition between the RKKY interaction and Kondo spin screening would eventually lead the heavy lanthanides Dy and Tb toward a magnetic instability, but first results in a strong enhancement of magnetism over that possible with normal positive exchange. When the Kondo spin screening wins over RKKY interaction at

higher pressures, it would lead to a quenching or at least a weakening of the 4*f* local moment by the surrounding conduction electrons (the so-called Kondo spin compensation) and thus a destruction of magnetic ordering.

More than three decades ago, a similar enhancement of magnetism in a lanthanide was also found in a ferromagnetic compound $CeRh_3B_2$ with an anomalously high Curie temperature $T_o \approx$ 115 K [119]. This was not expected according to the simple de Gennes factor in comparison with $GdRh_3B_2$ whose T_o is only 90 K [120] (de Gennes factor for Ce^{3+} and Gd^{3+} is 0.18 and 15.75 respectively, see Table 4.1). Moreover, the magnetic ordering temperature T_o in $CeRh_3B_2$ initially increased under pressure [121] but began to decrease above 2.5 GPa, eventually disappearing rapidly at 6.5 GPa [122]. Also, the substitution of less than 0.3% of La with Ce in $La_{1-x}Ce_xRh_3B_2$ suppresses and destroys the superconductivity of $LaRh_3B_2$ with initial rate of decrease −5.6 K/at.% Ce. These results strongly support the Kondo physics scenario for Ce in $CeRh_3B_2$ and in turn give weight to the assertion that Kondo physics is responsible for the anomalously high magnetic ordering temperature for Dy and Tb above P_{vc}.

As for Gd Fig. 4.25 shows that $T_c(P)$ for Y(0.5 at.% Gd) has no marked deviation from that of pure Y metal, especially across the P_{vc} at 59 GPa where Gd suffers 5% volume collapse. $T_c(P)$ for Y(0.5 at.% Gd) appears to track that of Y to the maximum pressure 127 GPa. The absence of anomalies in $T_o(P)$ and ΔT_c for Gd across the P_{vc} at 59 GPa to 120 GPa indicates that it remains magnetically stable to that pressure following the simple de Gennes scaling factor. This result is expected since the local magnetic state of Gd with its half-filled $4f^7$ is the most stable among all magnetic elements, where the $4f^7$ level lies ~ 9 eV below the Fermi level [108].

Interestingly, the pressure dependence of the magnetic ordering temperature $T_o(P)$, the spin-

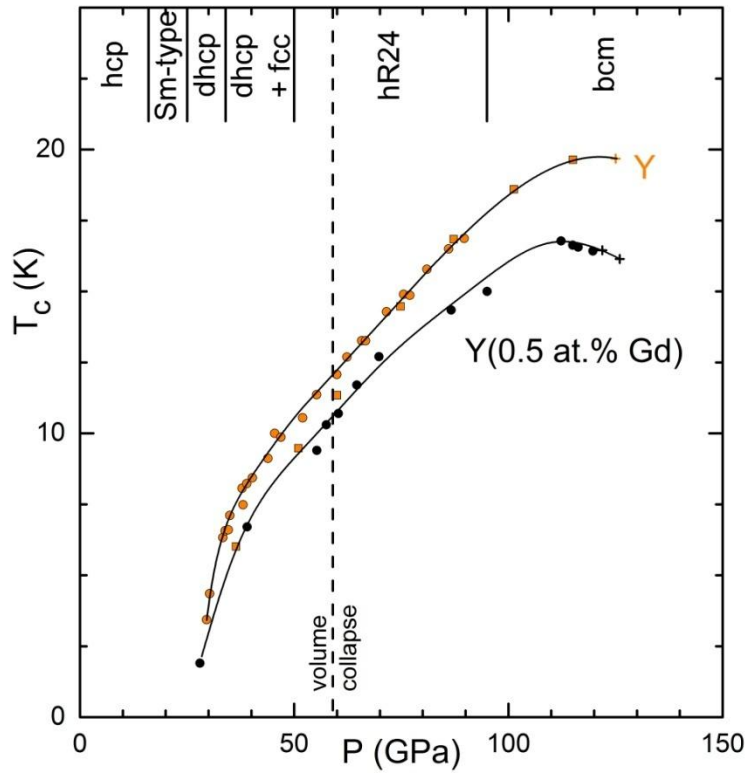

Figure 4.25: $T_c(P)$ for Y(0.5 at.% Gd) compared to that for Y [114]. Vertical dashed line marks P_{vc} at 59 GPa. At top graph are crystal structures taken on by Y [115]. Figure taken and modified from Ref. [103].

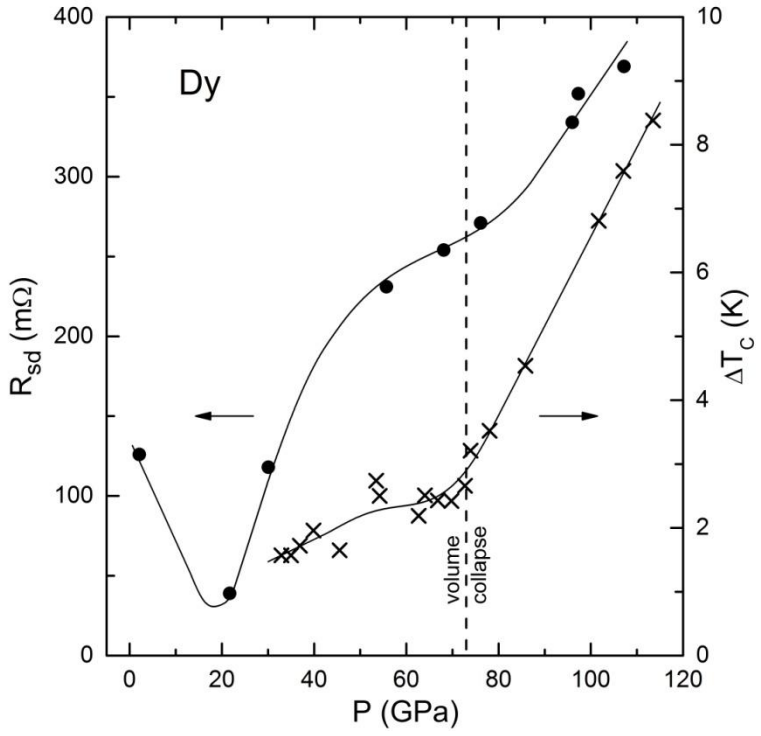

Figure 4.26: $R_{sd}(P)$ for Dy and $\Delta T_c(P)$ for the difference in $T_c(P)$ of Y(1 at.% Dy) compared to that of pure Y. Extended solid lines through data points are guides to the eye. Figure taken from Ref. [104].

disorder resistance $R_{sd}(P)$, and the suppression of the superconducting transition temperature $\Delta T_c(P)$ in a dilute magnetic alloy all track each other for Dy, Tb, and Gd (see Fig 4.26 for Dy), displaying their correlations. According to theoretical calculations [30], all three quantities are proportional to two terms, $J^2N(E_F)$ and the de Gennes factor $(g_J - 1)^2 J_t(J_t+1)$, where J is the exchange coupling constant between the 4*f* ion and the surrounding conduction electrons, $N(E_F)$ is the density of states at the Fermi level, g_J is the Landé-g factor, and J_t is the total angular momentum determined by Hund's rules.

One might also invoke the effect of crystalline electric fields (CEF) in order to explain the anomalously high magnetic ordering temperatures T_o in Dy and Tb at extreme pressures. More than 30 years ago, Noakes *et al.* [123] and Dunlap *et al.* [124] have shown that when CEF splitting is strongly anisotropic, as for a series of *RE*Rh_4B_4 compounds, where *RE* is a lanthanide, it may cause a strong enhancement of T_o. They suggested that when the anisotropies of single-ion magnetic moment is strong, the CEF can enhance the magnetic ordering temperature T_o of the RKKY interaction by the factor $\alpha = 3J_t/(J_t + 1)$, where for example, $\alpha = 2.6$ for trivalent Dy with $S = 5/2$, $L = 5$, $J_t = 15/2$ and $\alpha = 2.6$ for trivalent Tb with $S = 3$, $L = 3$, $J_t = 6$ according to Hund's rules. Since Gd carries no orbital moment ($L = 0$), it does not have CEF effects. This would then be consistent with the absence of strongly enhanced T_o, as well as a sharply increased ΔT_c, for Gd across the P_{vc}. It is also consistent with the similarity of pressure dependence of T_o between Gd, Dy, and Tb below P_{vc} where $T_o(P)$ is not due to CEF effects. On the other hand, this CEF effect scenario does not fully explain the strong suppression of superconductivity in Y by 1 at.% Dy and 0.5 at.% Tb above P_{vc} at 73 GPa and 53 GPa, respectively. This strong suppression of superconductivity by the dilute magnetic impurity can be only explained by the giant Kondo pair breaking effect, strongly supporting Kondo physics involvement in Dy and Tb above P_{vc}.

Inelastic neutron and x-ray scattering studies to extreme pressures should be helpful to pin down whether or not crystal electric field splittings play a role in the anomalously high values of T_o in Dy and Tb. In addition, going up to much higher pressures, like over 2 Mbars, would also test for Kondo physics behavior which would reveal a characteristic sinkhole-like suppression of $T_c(P)$, as observed in Kondo superconductors such as La(Ce) [34], La(Pr) [102], and Y(Pr) [103]. The search for a resistivity minimum in the dilute magnetic alloys Y(Dy) and Y(Tb) at different concentrations would also provide strong support for Kondo effect phenomena in Dy and Tb ions. Further experiments are necessary to establish the mechanism behind the anomalously high magnetic ordering temperature T_o for Dy and Tb above P_{vc}.

Chapter 5

Summary

- At ambient pressure the heavy lanthanides Gd, Tb, and Dy order magnetically at temperatures at or below ambient. With the indirect RKKY exchange interaction, the magnetic ordering temperature T_o is expected to be proportional to the de Gennes factor, as is indeed the case for the heavy lanthanide metals at ambient pressure. Electrical resistivity measurements have been carried out on the heavy lanthanides Gd, Tb, and Dy under extreme pressures well above P_{vc} where their volume collapse occurs. For $P < P_{vc}$ the pressure dependence of the magnetic ordering temperature $T_o(P)$ exhibits a remarkable similarity in those metals, signaling that this dependence is most likely governed by the density of states at the Fermi level $N(E_F)$. The fact that T_o(P) for Dy and Tb closely tracks that for Gd suggests that they are all magnetically stable below P_{vc}, following simple de Gennes scaling.

- The volume collapse phenomena in lanthanides seem to result from pressure-driven magnetic instability of the 4*f* local moment as evidenced, for example, by the strong decrease in the magnetic susceptibility for Ce across P_{vc}. For $P > P_{vc}$ $T_o(P)$ for Dy and Tb

rapidly increases above room temperature and deviates significantly from that for Gd, indicating a marked departure from conventional magnetic ordering.

- Synchrotron spectroscopy experiments find no change in valence or the localized magnetic state across P_{vc} in Tb, with a high likelihood that Dy would do the same. To test for the presence of Kondo effect phenomena in Dy and Tb, they were doped in dilute concentration into the superconducting host Y. High pressure electrical resistivity experiments were then carried out on Y(1 at.% Dy), Y(0.5 at.% Tb), and Y(0.5 at.% Gd). A strong suppression of the superconducting transition temperature T_c in Y by the dilute magnetic impurities Dy and Tb begins to occur above P_{vc}, pointing to the presence of giant Kondo pair breaking, in contrast to the case for Gd impurities. Together with the anomalously high value of T_o, the present results suggest possible Kondo lattice behavior in Dy and Tb above P_{vc}.

- The magnetic ordering temperature T_o appears to rise well above room temperature to 370 K for Dy and 341 K for Tb at the highest pressures of 157 GPa and 141 GPa, respectively. If confirmed, these transition temperatures would be record high values among the lanthanide metals where the current highest value is 292 K for Gd at ambient pressure.

Bibliography

[1] J. J. H. Hamlin, Superconductivity Studies at Extreme Pressure, Ph.D. Thesis, Washington University, St. Louis, Missouri, 2007.

[2] H. Beidenkopf, P. Roushan, J. Seo, L. Gorman, I. Drozdov, Y. S. Hor, R. J. Cava, and A. Yazdani, Nat. Phys. **7**, 939 (2011).

[3] P. Aynajian, E. H. da Silva Neto, A. Gyenis, R. E. Baumbach, J. D. Thompson, Z. Fisk, E. D. Bauer, and A. Yazdani, Nature **486**, 201 (2012).

[4] D. J. Scalapino, Rev. Mod. Phys. **84**, 1383 (2012).

[5] W. C. Koehler, J. Appl. Phys. **36**, 1078 (1965).

[6] R. V. Colvin, S. Legvold, and F. H. Spedding, Phys. Rev. **120**, 741 (1960).

[7] J. S. Schilling, Hyperfine Interact. **128**, 3 (2000).

[8] H. G. Drickamer, in *Prog. Very High Press. Res.*, edited by F. P. Bundy, W. R. Hibbard Jr., and H. M. Strong (John Wiley & Sons, Inc., New York, 1960).

[9] C. Kittel and H. Kroemer, *Thermal Physics*, 2nd ed. (W. H. Freeman, United States, 1980).

[10] P. W. Bridgman, Rev. Mod. Phys. **7**, 1 (1935).

[11] D. Goodstein and J. Goodstein, Phys. Perspect. **2**, 30 (2000).

[12] H. K. Onnes, KAWA (1911).

[13] J. F. Annett, *Superconductivity, Superfluids and Condensates*, 1st ed. (Oxford University Press, United States, 2004).

[14] W. Meissner and R. Ochsenfeld, Naturwissenschaften **21**, 787 (1933).

[15] N. W. Ashcroft and N. D. Mermin, *Solid State Physics* (Thomas Learning, Inc., United States, 1976).

[16] J. Bardeen, L. N. Cooper, and J. R. Schrieffer, Phys. Rev. **108**, 1175 (1957).

[17] W. L. McMillan, Phys. Rev. **167**, 331 (1968).

[18] A. S. Alexandrov, *Theory of Superconductivity from Weak to Strong Coupling* (Institute of Physics, London, 2003).

[19] J. J. Hopfield, Physica **55**, 41 (1971).

[20] A. F. Goncharov and V. V. Struzhkin, Physica C **385**, 117 (2003).

[21] J. S. Schilling, *Handbook of High Temperature Superconductivity: Theory and Experiment, Chapter 11* (Springer, Hamburg, 2007).

[22] M. Debessai, T. Matsuoka, J. J. Hamlin, W. Bi, Y. Meng, K. Shimizu, and J. S. Schilling, J. Phys. Conf. Ser. **215**, 012034 (2010).

[23] M. Sakata, Y. Nakamoto, K. Shimizu, T. Matsuoka, and Y. Ohishi, Phys. Rev. B **83**, 220512(R) (2011).

[24] J. S. Schilling, Phys. B+C **139-140**, 369 (1986).

[25] A. D. Mclean and R. S. Mclean, At. Data Nucl. Data Tables **26**, 197 (1981).

[26] G. Fabbris, Tuning Electronic Correlation with Pressure, Ph.D. Thesis, Washington University, St. Louis, Missouri, 2014.

[27] A. J. Freeman and R. E. Watson, Phys. Rev. **127**, 2058 (1962).

[28] M. A. Ruderman and C. Kittel, Phys. Rev. **96**, 99 (1954).

[29] D. Jackson, V. Malba, S. Weir, P. Baker, and Y. Vohra, Phys. Rev. B **71**, 184416 (2005).

[30] K. N. R. Taylor and M. I. Darby, *Physics of Rare Earth Solids* (Chapman and Hall Ltd, London, 1972).

[31] W. Meissner and G. Voigt, Ann. Phys. **7**, 892 (1930).

[32] J. Kondo, Prog. Theor. Phys. **32**, 37 (1964).

[33] J. S. Schilling and W. B. Holzapfel, Phys. Rev. B **8**, 1216 (1973).

[34] M. Maple, J. Wittig, and K. Kim, Phys. Rev. Lett. **23**, 1375 (1969).

[35] P. W. Bridgman, Proc. Am. Acad. **76**, 55 (1948).

[36] S. Doniach, in *Val. Instab. Relat. Narrow-Band Phenom.*, edited by R. D. Parks (Plenum, New York, 1977), p. 169.

[37] S. Doniach, Physica B+C **91**, 231 (1977).

[38] L. C. Martin, The Kondo Lattice Model : A Dynamical Cluster Approximation Approach, Ph.D. Thesis, Julius-Maximilians-Universit¨at W¨urzburg, 2009.

[39] S. Sykora and K. W. Becker, Sci. Rep. **3**, 2691 (2013).

[40] J. Blair and N. Ramsay, editors , *English Medieval Industries: Craftsmen, Techniques, Products* (Cambridge University Press, London, 2001).

[41] Q. Huang, D. Yu, B. Xu, W. Hu, Y. Ma, Y. Wang, Z. Zhao, B. Wen, J. He, Z. Liu, and Y. Tian, Nature **510**, 250 (2014).

[42] C. Kittel, *Introduction to Solid State Physics*, 8th ed. (John Wiley & Sons, Inc., United States, 2005).

[43] L. Pan, editor , *Diamond: Electronic Properties and Applications* (Kluwer Academic, United States, 1995).

[44] S. Jacobsen, Touching Beveled Culet Anvils, The Diamond Anvil Cell (DAC), Teaching Mineralogy Topical Resources, Retrieved December 11, 2014, From, http://serc.carleton.edu/NAGTWorkshops/mineralogy/mineral_physics/diamond_anvil.html, 2013.

[45] A. Dadashev, M. P. Pasternak, G. K. Rozenberg, and R. D. Taylor, Rev. Sci. Instrum. **72**, 2633 (2001).

[46] W. Bi, Studies in Magnetism and Superconductivity under Extreme Pressure, Ph.D. Thesis, Washington University, St. Louis, Missouri, 2011.

[47] Q. Sun and M. Alam, **139**, 933 (1992).

[48] R. Miletich, D. R. Allan, and W. F. Kuhs, Rev. Mineral. Geochemistry **41**, 445 (2000).

[49] N. Foroozani, J. Lim, J. S. Schilling, R. Fotovat, C. Zheng, and R. Hoffmann, J. Phys. Conf. Ser. **500**, 032007 (2014).

[50] S. Deemyad and J. S. Schilling, Phys. Rev. Lett. **91**, 167001 (2003).

[51] J. Hamlin, V. Tissen, and J. S. Schilling, Phys. Rev. B **73**, 094522 (2006).

[52] M. Debessai, J. Hamlin, and J. S. Schilling, Phys. Rev. B **78**, 064519 (2008).

[53] J. Lim, G. Fabbris, D. Haskel, and J. S. Schilling, arXiv:1404.4256 [cond-Mat.str-El] (2014).

[54] N. J. Hillier and J. S. Schilling, High Press. Res. **34**, 1 (2014).

[55] M. Seal, *Diamond Anvil Technology. In High-Pressure Research in Mineral Physics* (American Geophysical Union, Washington, D. C., 1987).

[56] J. S. Schilling, *High Pressure in Science and Technology: Part I, Collective Phenomena and Transport Properties* (North Holland, New York, 1984).

[57] *Diamond Anvil Cell Manual: Cell Preparation, AC Susceptibility and Electrical Resistivity Measurements, Accessory Equipment* (Schilling High Pressure Laboratory Manual, Washington Univesity, St. Louis, unpublished, 2014).

[58] E. Hecht, *Optics*, 4th ed. (Addison Wesley, United States, 2002).

[59] D. J. Dunstan, Rev. Sci. Instrum. **60**, 3789 (1989).

[60] J. K. Hulm and B. B. Goodman, Phys. Rev. **106**, 659 (1957).

[61] P. E. Frieberthauser and H. A. Notarys, J. Vac. Sci. Technol. **7**, 485 (1970).

[62] S. Jacobsen, The Heart of a Diamond Anvil Cell, The Diamond Anvil Cell (DAC), Teaching Mineralogy Topical Resources, Retrieved December 11, 2014, From, http://serc.carleton.edu/NAGTWorkshops/mineralogy/mineral_physics/diamond_anvil.html, 2013.

[63] B. Ley, Diameter of a Human Hair, The Physics Factbook, Retrieved December 16, 2014, From, http://hypertextbook.com/facts/1999/BrianLey.shtml, n.d.

[64] D.-X. Chen, J. A. Brug, and R. B. Goldfarb, IEEE Trans. Magn. **27**, 3601 (1991).

[65] P. L. Alireza and S. R. Julian, Rev. Sci. Instrum. **74**, 4728 (2003).

[66] H. D. Young and R. A. Freedman, *Sears and Zemansky's University Physics : With Modern Physics*, 13th ed. (Addison-Wesley, United States, 2012).

[67] K. Shimizu, K. Amaya, and N. Suzuki, J. Phys. Soc. Japan **74**, 1345 (2005).

[68] R. Jaramillo, Y. Feng, and T. F. Rosenbaum, Rev. Sci. Instrum. **83**, 103902 (2012).

[69] J. D. Barnett, S. Block, and G. J. Piermarini, Rev. Sci. Instrum. **44**, (1973).

[70] K. Syassen, High Press. Res. **28**, 75 (2008).

[71] A. D. Chijioke, W. J. Nellis, A. Soldatov, and I. F. Silvera, J. Appl. Phys. **98**, 114905 (2005).

[72] S. Buchsbaum, R. L. Mills, and D. Schiferl, J. Phys. Chem. **88**, 2522 (1984).

[73] N. J. Hillier, High Pressure Studies of Superconductivity, Ph.D. Thesis, Washington University, St. Louis, Missouri, 2013.

[74] D. M. Adams, R. Appleby, and S. K. Sharma, J. Phys. E. Sci. Instrum. **9**, 1140 (1976).

[75] Y. Akahama and H. Kawamura, J. Appl. Phys. **100**, 043516 (2006).

[76] C.-S. Yoo, B. Maddox, and V. Iota, MRS Proc. **1104**, (2008).

[77] P. W. Bridgman, Proc Am Acad Arts Sci **62**, 207 (1927).

[78] A. Lawson and T.-Y. Tang, Phys. Rev. **76**, (1949).

[79] M. Lipp, D. Jackson, H. Cynn, C. Aracne, W. Evans, and A. McMahan, Phys. Rev. Lett. **101**, 165703 (2008).

[80] N. Cunningham, N. Velisavljevic, and Y. K. Vohra, Phys. Rev. B **71**, 012108 (2005).

[81] K. Takemura and K. Syassen, J. Phys. F. Met. Phys. **15**, 543 (1985).

[82] W. Bi, Y. Meng, R. S. Kumar, A. L. Cornelius, W. W. Tipton, R. G. Hennig, Y. Zhang, C. Chen, and J. S. Schilling, Phys. Rev. B **83**, 104106 (2011).

[83] H. Hua, V. K. Vohra, J. Akella, S. T. Weir, R. Ahuja, and B. Johansson, Rev. High Press. Sci. Technol. **7**, 233 (1998).

[84] D. Errandonea, R. Boehler, B. Schwager, and M. Mezouar, Phys. Rev. B **75**, 014103 (2007).

[85] N. Cunningham, W. Qiu, K. Hope, H.-P. Liermann, and Y. K. Vohra, Phys. Rev. B **76**, 212101 (2007).

[86] R. Patterson, J. Appl. Phys. **95**, 5443 (2004).

[87] Y. K. Vohra, B. R. Sangala, A. K. Stemshorn, and K. M. Hope, Mater. Res. Soc. Symp. Proc. **1104**, NN01 (2008).

[88] J. M. Montgomery, G. K. Samudrala, G. M. Tsoi, and Y. K. Vohra, J. Phys. Condens. Matter **23**, 155701 (2011).

[89] G. N. Chesnut and Y. K. Vohra, Phys. Rev. B **57**, 10221 (1998).

[90] J. Lim, G. Fabbris, D. Haskel, and J. S. Schilling, J. Phys. Conf. Ser. **500**, 192009 (2014).

[91] R. Ramirez and R. M. Martin, Phys. Rev. B **3**, 2425 (1971).

[92] B. Johansson, Philos. Mag. **30**, 469 (1974).

[93] J. W. Allen and R. M. Martin, Phys. Rev. Lett. **49**, 1106 (1982).

[94] S. Blundell, *Magnetism in Condensed Matter* (Oxford University Press, New York, 2001).

[95] M. MacPherson, G. Everett, D. Wohlleben, and M. Maple, Phys. Rev. Lett. **26**, 20 (1971).

[96] J.-P. Rueff, J.-P. Itié, M. Taguchi, C. Hague, J.-M. Mariot, R. Delaunay, J.-P. Kappler, and N. Jaouen, Phys. Rev. Lett. **96**, 237403 (2006).

[97] M. J. Lipp, A. P. Sorini, J. Bradley, B. Maddox, K. T. Moore, H. Cynn, T. P. Devereaux, Y. Xiao, P. Chow, and W. J. Evans, Phys. Rev. Lett. **109**, 195705 (2012).

[98] M. B. Maple, Appl. Phys. **9**, 179 (1976).

[99] J. Roehler and R. Luebbers, Phys. B **206-207**, 368 (1995).

[100] B. Maddox, Ph.D. Thesis, University of California, Davis, 2006.

[101] J. A. Bradley, K. T. Moore, M. J. Lipp, B. A. Mattern, J. I. Pacold, G. T. Seidler, P. Chow, E. Rod, Y. Xiao, and W. J. Evans, Phys. Rev. B - Condens. Matter Mater. Phys. **85**, 1 (2012).

[102] J. Wittig, Phys. Rev. Lett. **46**, 1431 (1981).

[103] G. Fabbris, T. Matsuoka, J. Lim, J. Mardegan, K. Shimizu, D. Haskel, and J. Schilling, Phys. Rev. B **88**, 245103 (2013).

[104] J. Lim, G. Fabbris, D. Haskel, and J. S. Schilling, Phys. Rev. B **91**, 045116 (2015).

[105] B. R. Coles, Adv. Phys. **7**, 40 (1958).

[106] G. K. Samudrala, G. M. Tsoi, S. T. Weir, and Y. K. Vohra, High Press. Res. **34**, 266 (2014).

[107] J. Lim, G. Fabbris, D. Haskel, and J. S. Schilling, arXiv:1502.01785 [cond-Mat.str-El] (2015).

[108] Z. P. Yin and W. E. Pickett, Phys. Rev. B **74**, 205106 (2006).

[109] D. Errandonea, R. Boehler, B. Schwager, and M. Mezouar, Phys. Rev. B **75**, 014103 (2007).

[110] J. C. Duthie and D. G. Pettifor, Phys. Rev. Lett. **38**, 564 (1977).

[111] G. Fleming and S. Liu, Phys. Rev. B **2**, 164 (1970).

[112] M. Tokita, K. Zenmyo, H. Kubo, K. Takeda, M. Mito, and T. Iwamoto, J. Magn. Magn. Mater. **272-276**, 593 (2004).

[113] S. H. Liu, Phys. Rev. **127**, 1889 (1962).

[114] J. J. Hamlin, V. G. Tissen, and J. S. Schilling, Phys. C Supercond. **451**, 82 (2007).

[115] G. K. Samudrala, G. M. Tsoi, and Y. K. Vohra, J. Phys. Condens. Matter **24**, 362201 (2012).

[116] J. S. Schilling, Adv. Phys. **28**, 657 (1979).

[117] J. R. Schrieffer and P. A. Wolff, Phys. Rev. **149**, 491 (1966).

[118] Y. Yang, Z. Fisk, H.-O. Lee, J. D. Thompson, and D. Pines, Nature **454**, 611 (2008).

[119] K. Dhar, K. Malik, and R. Vijayaraghavan, J. Phys. C Solid State Phys. **14**, L321 (1981).

[120] S. K. Malik, R. Vijayaraghavan, and W. E. Wallace, J. Magn. Magn. Mater. **37**, 303 (1983).

[121] S. A. Shaheen, J. S. Schilling, P. Klavins, C. B. Vining, and R. N. Shelton, J. Magn. Magn. Mater. **47&48**, 285 (1985).

[122] A. L. Cornelius and J. S. Schilling, Phys. Rev. B **49**, 3955 (1994).

[123] D. R. Noakes and G. K. Shenoy, Phys. Lett. **91A**, 35 (1982).

[124] B. D. Dunlap, L. N. Hall, F. Behroozi, G. W. Crabtree, and D. G. Niarchos, Phys. Rev. B **29**, 6244 (1984).